On Modular Coil Systems of the WENDELSTEIN VII-AS Type with Reactor Dimensions

E. Harmeyer, U. Brossmann, H. Gorenflo
J. Kisslinger, S. Mukherjee, J. Raeder
F. Rau, H. Wobig

IPP 2/269 August 1983

MAX-PLANCK-INSTITUT FÜR PLASMAPHYSIK

8046 GARCHING BEI MÜNCHEN

MAX-PLANCK-INSTITUT FÜR PLASMAPHYSIK

GARCHING BEI MÜNCHEN

On Modular Coil Systems of the WENDELSTEIN VII-AS Type with Reactor Dimensions

E. Harmeyer, U. Brossmann, H. Gorenflo
J. Kisslinger, S. Mukherjee, J. Raeder
F. Rau, H. Wobig

IPP 2/269 August 1983

Die nachstehende Arbeit wurde im Rahmen des Vertrages zwischen dem Max-Planck-Institut für Plasmaphysik und der Europäischen Atomgemeinschaft über die Zusammenarbeit auf dem Gebiete der Plasmaphysik durchgeführt.

Abstract

Modular stellarator coil systems with reactor dimensions are described. They comprise 5 field periods (F.P.) with 4 to 10 twisted coils within each. Preference is given so far to a data set of 10 coils/F.P.. The coil configuration is optimized with respect to the magnetic field (B, rotational transform ι) and with respect to the available space for the blanket. Technical constraints of superconducting NbTi coils are satisfied. The forces, mechanical stresses and deformations are calculated and suitable support concepts for the coils are investigated.

Contents

1. Introduction

This study investigates the feasibility of a modular stellarator coil system on the basis of the WENDELSTEIN VII-AS configuration. This advanced stellarator is described in detail in /1, 2, 3/. In the previous study /4/ the coil configuration of WENDELSTEIN VII-AS was scaled up to reactor dimensions, but without optimizing the plasma parameters for reactor application. The aim for that investigation was to identify technical problems of the modular coil system.

In the following, parameters of the magnetic field in conjunction with the geometric reactor dimensions are reconsidered. In view of plasma confinement and particle diffusion the mean minor plasma radius is increased to r = 1.6 m and the mean major plasma radius to R_o = 25.5 m. This gives a plasma aspect ratio of 15.9. The combined blanket and shielding thickness is taken as 1.70 m, which is close to the value used in /5/. For the coil housing, a radial thickness of 0.1 m is added.

The calculation of the topology of the modular coil system starts from a current layer on a chosen torus. This current layer is obtained numerically /6/ from the magnetic topology, which is described by a sum of DOMMASCHK potentials /7/. Discretization of the current layer leads to coils of finite extent. Recalculating the magnetic field of these coils establishes the required degree of approximation of the original magnetic topology. The toroidal excursion of the twisted coils is comparatively small if the torus is chosen not too far outside of the "last" magnetic flux surface and if the coil aperture is adapted to the shape of the flux surfaces /1/.

2. Optimization of the coil system

The present basis for determining reactor-size advanced stellarator coil configurations is the modular coil set of WENDELSTEIN VII-AS with a total of 40 + 5 twisted coils, 5 being of special large aperture to provide experimental access. Regarding the number of coils per field period two different cases are considered:

- 10 coils per field period
- 4 coils per field period.

With 5 field periods around the torus circumference, this makes a total coil number of 50 and 20, respectively.

The cross-section, current density, mean radius and ellipticity of the coils are varied in both cases. Care is being taken to ensure that the distance between the inner side of the coils and the plasma boundary layer is at least 1.8 m. The total coil current is chosen such that a field of B_o = 5.3 T is produced on the plasma axis (with one exception). The choice of this value of B_o is determined by the maximum field on the coils which is limited to 9 T.

Characteristic data for a total of 8 different configurations is presented in Table I. The values for the magnetic fields, the induction coefficients, and the force densities are computed with the EFFI code /8/; the rotational transform angle and the field ripple are computed with the GOURDON code /9/. It is furthermore ensured that the degree of "drift-optimization", characterising WENDELSTEIN VII-AS as an advanced stellarator, is not degraded by the changes made from WENDELSTEIN VII-AS towards the reactor-size coil topology /10, 11/. Some of the cases investigated are discussed below.

Figs. 1 and 2 show top views of the modular coil sets of the configurations ASR2510 and ASR254E with 10 and 4 coils/F.P. In both cases identical values of the coil current density j = 6.86 MA/m^2 and the magnetic induction B_o = 5.3 T are established by proper choices of the

radial and lateral coil dimensions, h and w, resp.. Although the coils shown in Fig. 2 are more massive, they clearly separate and thus could allow an easy scheme of reactor maintenance, i.e. the demounting of each coil by a purely radial motion appears possible. In an effort to lower the maximum induction at the conductor a square cross section is chosen for the coil at $\varphi = 36^{\circ}$.

Magnetic vacuum field configurations of these two coil sets are given in Figs. 3 and 4: For toroidal positions of zero and 1/2 field periods the contours of several nested magnetic surfaces are drawn. The values of the rotational transform at the magnetic axis are $\iota(o) = 0.43$ and 0.47, resp.. In the configuration with 4 coils per field period $\iota(o)$ is increased by 10 %. This is due to the two superposed variations of the coil set, the increased coil cross-section, and the larger gaps between the coils.

The relative field ripple along the magnetic axis

$$\delta_o = (B_{max} - B_{min}) / (B_{max} + B_{min})$$

amounts to 1.6 % and 8.5 % for the two cases. In the configuration ASR2510 the last magnetic surface is at $r \approx 2$ m, with $\iota_r = 0.45$, whereas ASR254E only allows a minor radius of $r \approx 1.5$ m with $\iota_r = 0.35$. The ripple along the last magnetic surfaces of these two configurations amounts to $\delta_r = 12.5$ % and 17 %, see Fig. 5 and 6. The figures show /B/ versus the length of the field line for about 8 field periods. The increased values of the ripple within the magnetic surfaces of ASR254E is a direct consequence of the lower number of twisted coils per field period. It also is responsible for the lower value of rotational transform at the last magnetic surface, thus causing a negative value of the shear

$$\delta\iota/\iota = (\iota_r - \iota_o) / \iota_o,$$

and a reduction in the quantity

$$V'' = (\int(dl/B)_r - \int(dl/B)_o) / \int(dl/B)_o.$$

On the other hand the maximum values of $j_{\parallel}/j_{\perp}$, which characterize the degree of "drift-optimization" /12/, the associated improvement factor

$$F = \frac{2/\iota_o}{(j_{\parallel}/j_{\perp})_{max}} \quad ,$$

as well as the quantities expected as a permissible equilibrium-ß in an advanced stellarator,

$$ß_F = F\, ß_{eq}, \qquad ß_{eq} = (r/R)\, \iota_o^2,$$

do not deviate much for the two coil configurations ASR2510 and ASR254E. Comparing the shapes of the vacuum magnetic flux surfaces at a toroidal position $\varphi = 0$ for the two coil sets, the triangularity is more pronounced in the case of ASR254E. This feature is caused by the presence of a twisted coil at the azimuth $\varphi = 0$, whereas in ASR2510 there is a gap between two adjacent coils.

If one splits this particular coil of ASR254E into two halves, each having half of the current, a local gap at $\varphi = 0$ is introduced again, and a magnetic topology is attained in the coil configuration ASR5, which closely agrees with ASR2510 in shape and size, see Fig. 7, but has other characteristics more similar to those of ASR254E, see Table II.

Regarding the option of 4 to 5 or of 10 twisted coils per field period we presently prefer a system with 10 coils/F.P.. Although their maintenance might be more complicated, their smaller magnitude of field ripple promises a better confinement of the plasma. As will be shown in sect. 4.1 also the local peak fields at the coils are reduced in these configurations.

For the systems with 10 coils/F.P. some studies are done towards obtaining a scaling of the maximum induction B_M at the coil surface with the dimensions and current density j of the coils, but maintaining the axis value of the magnetic induction at $B_o = 5.3$ T (with one exception, see Table I). The ratio h/w $\sim$2 of radial to

lateral coil dimension is usually kept constant, mainly because of the limited space between the coils at lower values of j. For comparison with Fig. 1, the top view of the configuration ASR2510M with a maximum current density $j = 20\ MA/m^2$ is shown in Fig. 8. If this large value of j would be feasible in coil construction, the maintenance of the coil system by a purely radial motion of the coils for demounting would be alleviated by both, the increased space between the coils, and the reduced coil mass. The coils closed to $\varphi = i \cdot 72^o$, i = 1-5, are interlocked, however.

For the coil configurations as described above the average coil aspect ratio amounts to 4.15, which value agreess with the coil aspect ratio of the twisted coils [+)] of WENDELSTEIN VII-AS, see /1/. The aperture (bore) of these coils is elliptic and the ellipticity is identical for all of them. On the other hand, for the reactor-size coils described so far, the ratio of coil half-axes b/a changes from values of 1.117 to 1.349 when proceeding in the toroidal direction from $\varphi = 0$ to $\varphi = 36^o$ = 1/2 F.P..

Further optimization of the coil configuration for this work is directed towards reducing the toroidal excursions and simultaneously increasing the value of ι. This is done in several steps. They employ the choice of different torus shapes, recalculation of the appropriate surface current patterns in order to retain the properties of the magnetic configuration, e.g. of ASR2510, and then establishing the contours of the discrete twisted coils. Finally, by increasing the coil aspect ratio, and also introducing some helicity in the formerly plane and radially oscillating position of the coil center points, a new coil data set is obtained.

+) with the exception of the 5 special large coils of WENDELSTEIN VII-AS. They have a lower coil aspect ratio and a more triangular shape of their bores.

By an adjustment of the ellipticity of the coil cross section the desired radial distance Δ = 1.8 m between the last magnetic surface and the coil bore is established or even exceeded. Thus we arrive at the configuration ASR25T7, which represents the present state of the art. This coil data set and the associated characteristics of its vacuum magnetic fields are described in the following.

The top view of the coil set (10 coils/F.P.) is shown in Fig. 9. The current density in the coils is adjusted to j = 9.8 MA/m^2 within the radial and lateral coil dimensions h = 1.4 and w = 1.0 m, resp. Thus a total coil current of 13.7 MA yields a magnetic induction of B_o = 5.3 T at the magnetic axis.

The system of nested vacuum flux surfaces is given in Figs. 10-12 for the three toroidal positions of zero, 1/4 and 1/2 field periods, i.e. at φ = 0, 18 and 36°. Also shown in the figures are the apertures of the adjacent twisted coil. The coil bores are of elliptic cross section. The center filaments of the coils attain ratios of half axes b/a varying from 0.9 to 1.7 between φ = 0 and φ = 36° , at an average coil aspect ratio 4.76. The centers of these ellipses are situated along a helical curve $R_c(\varphi)$, $Z_c(\varphi)$ characterized by

$$R_c(\varphi) = 25\ (1.016 - 0.028 \cos 5\varphi) \quad /m/$$
$$Z_c(\varphi) = 0.15 \sin 5\varphi \quad /m/$$

The radial amplitude of the oscillation exceeds the vertical one. Furthermore, the orientation of the half-axes oscillates in the poloidal direction by an angle

$$\theta_o(\varphi) = \pi/8\ (\sin 5\varphi + 0.5 \sin 10\varphi).$$

This type of torus topology is similar to that used for the twisted coils of WENDELSTEIN VII-AS, apart from different values of the constants.

The values of the rotational transform of ASR25T7, both at the axis $\iota_o = 0.58$ and at the edge, $\iota_r = 0.61$ are considerably increased, in comparison to the previous reactor-size coil sets, as well as compared to WENDELSTEIN VII-AS. Care has been taken to avoid a rational value $\iota = K/L$ with values of integers K = 1 and 5 and low values of $L < 8$. The aspect ratio of the last useful magnetic surface is R/r = 14.6. The slightly corrugated shape of this surface is caused by the vicinity of $\iota = 5/8$ at the separatrix. The shear is + 5.2 %, and $V'' = - 8.6 \cdot 10^{-4}$ is just marginally negative. As shown in Table II, the values of $j_{\parallel}/j_{\perp}$ and of the improvement factor F are comparable to the previous data sets, if one takes into account the general trend of configurations of WENDELSTEIN VII-AS type, namely a slight reduction of the degree of drift-optimization when increasing the rotational transform, see Fig. 13.

In Fig. 14 the drift-surfaces of passing α-particles (guiding center motion) are shown, starting at some radial position at $\varphi = 0$. The velocity direction is parallel ($V_{\parallel}$) and antiparallel ($V_{\nparallel}$) to the magnetic vacuum field direction. The energy is 3.5 MeV and the offset Δ^*/ρ of the drift surfaces from the magnetic surfaces (normalized by the LARMOR radius ρ) varies between 0.8 and 1.5 within the field period. These values are lower than $1/\iota = 1.7$ which is expected in a standard l = 2 stellarator of identical rotational transform. As further demonstrated in Table II also the value of $\beta_{eq} = (r/R) \cdot \iota_o^2$ or a possible improved value for drift-optimized systems, $\beta_F = F \cdot \beta_{eq}$ is optimum in the configuration ASR25T7. The difficult questions regarding the value of stability-beta in stellarators are not addressed at present.

Nevertheless, we conclude the configuration ASR25T7 as being optimized regarding the magnetic topology, rotational transform, and aspect ratio, if one depends on a distance $\Delta = 1.8$ m required for first wall, blanket, shield, dewar and coil housing.

Table I: Stellarator reactor configurations

			ASR254C	ASR254E	ASR254F	ASR2510	ASR2510M	ASR2510N	ASR25S3	ASR25T7
mean major plasma radius	R_o	/m/	25.5	25.5	25.5	25.5	25.5	25.5	25.5	25.5
mean coil radius	r_c	/m/	6.2	6.2	6.2	6.2	6.2	5.7	4.8	5.24
radial coil thickness	h	/m/	2.8	3.16	3.12	2.	1.054	1.2	1.2	1.4
lateral coil thickness	w	/m/	1.4	1.58	2.08	1.	0.528	0.6	0.6	1.
coil cross-section	A_c	/m^2/	3.92	5.	6.49	2.	0.557	0.72	0.72	1.4
coil mass	m_c	/Mg/	1280.	1632.	2120.	652.	182.	216.	182.	386.
No. of coils total/per F.P.	n/np		20/4	20/4	20/4	50/10	50/10	50/10	50/10	50/10
total coil current	I_c	/MA/	34.3	34.3	34.3	13.72	11.14	13.73	13.73	13.73
overall current density	jc	/MA/m^2/	8.75	6.86	5.29	6.86	20.	19.07	19.07	9.8
self inductance 1. coil	L_{11}	/μH/		15.2	14.4		25.3	22.8	17.4	18.5
total stored magnetic energy	E_s	/GJ/		~230.	~220.		~160.	~210.	~150.	~170.
average field on plasma axis	B_o	/T/	5.3	5.3	5.3	5.3	4.3	5.3	5.3	5.3
field ripple on plasma axis	δB	/T/	$^{+0.6}_{-0.3}$	$^{+0.6}_{-0.3}$	$^{+0.7}_{-0.3}$	±0.1	±0.08	±0.1	±0.1	±0.1
max. field at coil	B_M	/T/	10.9	10.14	9.52	8.8	9.02	10.35	9.72	8.73
induction ratio	B_M/B_o		2.05	1.91	1.79	1.66	2.1	1.95	1.83	1.64
rot. transf. on plasma axis	ι(o)		0.467	0.472	0.477	0.427	0.574	0.577	0.593	0.583
radius of "last" flux surface	r	/m/	1.72	1.46	1.53	1.93	1.67	1.65	1.70	1.75
rot. transf. "last" flux surface	ι(r)		0.264	0.354	0.356	0.447	0.601	0.606	0.611	0.613
max. force density macroelement	$\overline{F_m}'$	/MN/m^3/	33.3	25.8	19.6	26.5	67.7	80.7	78.0	41.2

Table II: Characteristic Values of Vacuum Magnetic Fields

Configuration			ASR2510	ASR254E	ASR5	ASR25T7
magnetic axis:						
major radius	R_o	/m/	25.5	25.5	25.5	25.5
rotational transform	ι_o		0.427	0.472	0.463	0.583
induction	B_o	/T/	5.3	5.3	5.3	5.3
ripple	δ_o	/%/	1.6	8.5	10.3	1.8
"last" magnetic surface:						
minor radius	r	/m/	1.93	1.46	1.75	1.75
aspect ratio	R/r		13.2	17.5	14.6	14.6
rotational transform	ι_r		0.447	0.354	0.411	0.613
ripple	δ_r	/%/	12.5	17.0		12.6
shear		/%/	+4.8	-24.9	-11.2	+5.2
V"		/%/	-0.8	- 0.2	+ 0.3	-0.1
max $(j_{\parallel}/j_{\perp})$			2.8	2.2	2.3	2.1-2.2
$2/\iota_o$			4.7	4.2	4.3	3.4-3.3
$F = \frac{2/\iota_o}{\max(j_{\parallel}/j_{\perp})}$			1.7	1.9	1.9	1.56
$\beta_{eq} = r/R\ \iota_o^2$		/%/	1.4	1.3	1.5	2.3
$\beta_F = F\ \beta_{eq}$		/%/	2.4	2.5	2.9	3.6

3. Constraints due to superconductivity

The coils of the reactor-size advanced stellarator configurations described above are assumed to be superconducting. In order to follow a conservative approach we choose NbTi at an operating temperature of 4.2 K as superconducting material. This limits the maximum magnetic induction B_{max} in the coil to about 9 T /13/. This value imposes a major technical constraint on the configurations if the field B_o on the plasma axis has to be ≥ 5 T. The number of coils per field period has to be as large as possible, resulting in a thick pack of coils that makes maintenance difficult. On the other hand, the current density should not be too high. This is in keeping with the condition that the current density in the superconductor has to remain below the critical current density. With NbTi at T = 4.2 K and B = 8.8 T the latter is $j_{crit} = 4.5 \times 10^8$ A/m^2 /14/. To ensure cryogenic stability and stability in the safety discharge, the superconductor has to be embedded in a sufficient quantity of stabilizing copper. The ratio of the cross-section of the stabilizing material to that of the superconductor was conservatively estimated at $\alpha \approx 16$. If the superconductor is assumed to be 2.5 % and the embedding copper conductor 40 % of the total cross-section, an overall current density $j \leq 10$ MA/m^2 is required. Table I shows that the conditions of the maximum field and the maximum current density are best satisfied in configuration ASR25T7. It therefore serves as the basis for further consideration of coil engineering.

4. Engineering considerations of the coil system ASR25T7

As discussed in section 2 the coil system ASR25T7 constitutes an optimized configuration with respect to essential parameters of the magnetic field. Furthermore it satisfies technical boundary conditions best. Fig. 15 shows a field period of the coil assembly from above, Fig. 16 from the front. It can be seen that coils 3 to 8 can be removed from the coil assembly by only radial displacement. With the other coils azimuthal movement is additionally required to remove them from the assembly. Coils 1 and 10 are subject to comparatively strong toroidal excursion, they are interlinked with the adjacent coils. In Fig. 17 coils 6 to 15 are viewed from above, showing that maintenance of coil 9 to 12 is difficult.

The coil system contains 5 different types of coils. Coils 6 to 10 conform in shape to coils 1 to 5, but the configuration is mirror symmetric. For the field and force calculations it is sufficient to consider coils 1 to 5. Figures 18 to 22 show coils 1 to 5 from two sides. Each coil is subdivided into 48 volume elements (with, in general case, non-parallel straight boundary lines) similar to the rectangular general current elements (GCE's) used in EFFI. The volume elements are consecutively numbered for the 5 coils so that they are readily identified in the field and force calculations.

4.1 Magnetic field distribution

The field calculations are made with the EFFI code. The value of current density in the coils is 9.8 MA/m^2, and is assumed to be uniformly distributed over the total coil cross-section of 1.4 m^2. The direction of the current density vector is governed by the alignment of the GCE's.

The field distribution is calculated by integrating over all of the current elements according to Biot-Savart /8/:

$$\vec{B} = \frac{\mu_0}{4\pi} \iint_{S\,A} \frac{j\vec{ds} \times \vec{r}\,dA}{|\vec{r}|^3} \qquad (1)$$

where j is the current density, $\vec{r}$ the vector from the source point to the field point, $d\vec{s}$ a line element in the direction of the current, and dA an area element at right angles to the current flux. Fig. 23 shows the field distribution in the plane z = 0 in the 1st quadrant of the configuration. The dashed lines are contour lines; they connect points of equal /B/. The value on the plasma axis is B_o = 5.3 T and the maximum value in this plane is $B_m \gtrsim 8.2$ T on the inner side of coil 5. Fig. 24 shows the same field distribution as a 3D plot.

Of great importance for the coil technology is the question what magnetic flux density B prevails in the coils. With NbTi as superconducting materials this ought not to exceed 9 T. As the maximum flux density is expected to be at the inner side of the coil, the program CONTOUR was developed which computes points at the inner side of the coil (in the centre of the GCE or along the edge of the GCE).

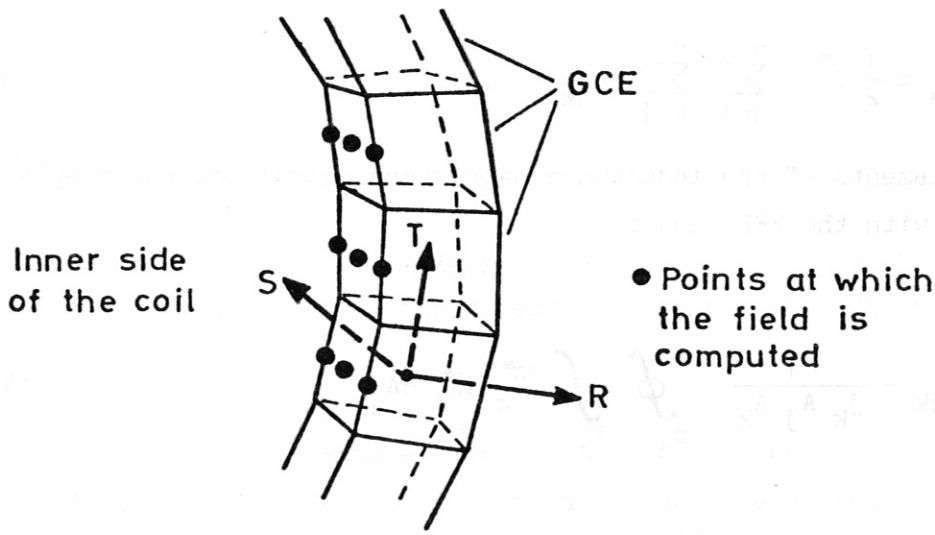

The B field is calculated along this contour. In Figs. 25 to 29 the values of B and the components are plotted in local coil coordinates (R, S, T) for coils 1 to 5 as a function of the longitudinal coordinate of the coils (number of the GCE). In all cases the contour runs through the middle of the inner side of the coil which faces towards the magnetic axis. The maximum value of 8.53 T occurs at GCE 217 of coil 5. Calculation of the B field along an edge contour of the inner side of the coil yields at GCE 6 of coil 1 a still higher value,

namely 8.73 T (see Fig. 30). Here the maximum flux density occurs because the coil has strong toroidal curvature in this region. A plot of the contour lines of B with a cross-section through GCE 6 is shown in Fig. 31. The value of B_M = 9.24 T is uncertain, however, because it is calculated near the intersection of two GCE's.

4.2 Energy stored in the coil system

The total energy stored in a coil system with n coils is

$$E_s = \frac{1}{2} \sum_{j=1}^{n} \sum_{k=1}^{n} I_j L_{jk} I_k \quad , \tag{2}$$

where L_{jk} are the elements of the inductance matrix and I_j, I_k are the total coil currents. If the currents in all of the coils are equal, it follows that

$$E_s = \frac{1}{2} I^2 \sum_{j=1}^{n} \sum_{k=1}^{n} L_{jk} \quad . \tag{3}$$

The elements of the inductance matrix are calculated for single turn coils with the EFFI code:

$$L_{jk} = \frac{1}{j_k A_j A_k} \oint_{s_j} \int_{A_j} \vec{V}_k \cdot d\vec{s}_j \cdot dA_j \quad , \tag{4}$$

where j_k is the current density in coil k, A_j and A_k are the cross-sectional areas of the respective coils, and $\vec{V}_k$ is the vector potential due to coil k.

Computation of the inductance matrix with EFFI code is very time-consuming; in one CRAY-hour about 40 inductance values are determined for the set of 50 coils. (For comparison: the inductance matrix is a symmetric n x n, i.e. with n = 50 one has to compute 1275 values.) It is found, however, that it is possible to deduce the total inductance from the values of the first matrix elements.

The total inductance is

$$L := \sum_{j=1}^{n} \sum_{k=1}^{n} L_{jk} \quad . \tag{5}$$

The numerical values show that the self-inductances of the coils are approximately equal (because of $\bar{r}_c$ = const.), and that the sum of the mutual inductances of one coil is proportional to the self-inductance of that coil.

It thus holds that

$$\begin{aligned} L_{jj} &\approx L_{kk} \qquad \forall\, j,k \quad , \\ \sum_{\substack{k=1 \\ k\neq j}}^{n} L_{jk} &\approx c\, L_{jj} \qquad \forall j,k,\ k \neq j. \end{aligned} \tag{6}$$

Substitution in eq. (5) yields

$$L \approx (1 + c)\, n\, L_{jj} \tag{7}$$

For n = 50 the factor c is roughly 1, for n = 20 it is about c = 0.35. These estimations are valid for dimensions of the coil systems considered above.

In ASR25T7 the first matrix element is obtained to be $L_{11} = 18.5 \times 10^{-6}$H. With eq. (7) the total inductance of the configuration is then found to be $L \approx 1.85 \times 10^{-3}$H. This value can be compared with the inductance of a ring coil.
According to /15/, p. 282, it holds that

$$L = n^2 \cdot \frac{\mu_o A}{2\pi R_o} = n^2 \cdot \frac{\mu_o \bar{r}_c^{\,2}}{2 R_o} \tag{8}$$

With the numerical values of Table I one obtains an inductance of $L = 1.7 \times 10^{-3}$H, i.e. there is good agreement. With eq. (3) the total energy stored in the coil system is found to be $E_s \approx 170$ GJ.

4.3 Magnetic forces

The magnetic forces are also computed with the EFFI code. The force $\vec{F}$ and the force densities $\vec{F}'$ are given by

$$\vec{F} = \iint_{S}\iint_{A} j\vec{ds} \times \vec{B} dA \quad ,$$

$$\vec{F}' = \frac{\vec{F}}{V_{GCE}} \qquad (9)$$

In Figs. 32 to 36 the value of $|\vec{F}'|$ and the components of F' are plotted in local coordinates (R, S, T) for coils 1 to 5 versus the longitudinal coordinate of the coils (number of the GCE). This local coordinate system determines the orientation of each GCE, where R is the normal, S the binormal and T is the tangential unit vector.

In these local coil coordinates there are only 2 force density components, the one in the radial (R coordinate) and the other in the lateral (S coordinate) direction. No forces are exerted in the longitudinal direction of the coils (T coordinate) because the current flows in the T direction. The value of the lateral force density component depends on the extent of the toroidal excursion of the coils, of its local radius of curvature, and of the vicinity of the adjacent coil.

In the following, two coils are considered:

- Coil 1 is characterized by particularly strong toroidal excursion.

- Coil 5 is highly elliptical but only has slight toroidal excursion.

Figs. 37 and 38 show coil 1, Figs. 39 and 40 coil 5. The radial and lateral force densities are specified on the GCE's. The largest force

density occurs on GCE 6 of coil 1 because the lateral force density component is particularly large here owing to the curvature of the coil. The maximum force density is 41.2 MN/m^3.

The force densities are averaged values (average over the GCE "macroelement"). The spatial dependence of the force density can be determined by subdividing the GCE's into "microelements". This is done with GCE 195 of coil 5 as an example:

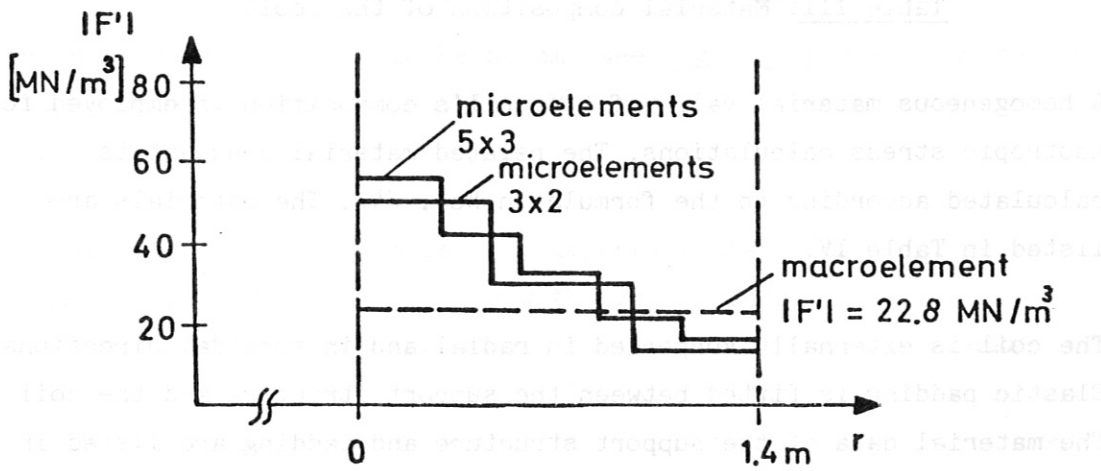

The force density is largest on the inner side of the coil since the highest field is present there. Furthermore, it is clear that subdividing the macroelements into 3x2 microelements is sufficient and economic regarding the required computational time. Therefore in the stress calculations with SAP a system of 3x2 microelements is used.

4.4 Analysis of the mechanical stresses

The analysis of the mechanical stress is performed with the SAP V(2) program system. The coil is subdivided into 288 microelements. Each element is a 12-node, isoparametric finite element. The magnetic force densities are converted into nodal forces with the SHAPE program.

The coil is assumed to be composed of superconductor, copper, stainless steel, and insulation materials and their respective

percentages are listed in Table III. The remaining 10 % are liquid helium. For the stress calculations a filling factor of 0.8 has to be regarded equivalent to the amounts of copper and steel.

Superconductor	2.5 %
Copper	40.0 %
Stainless steel	40.0 %
Fibre-glass epoxy	7.5 %

Table III: Material composition of the coil

A homogeneous material value of the coil's composition is employed for isotropic stress calculations. The related material constant is calculated according to the formula in Ref. /4/. The materials are listed in Table IV.

The coil is externally supported in radial and in toroidal directions. Elastic padding is fitted between the support structure and the coil. The material data of the support structure and padding are listed in Table IV. The geometric data of the support structure and padding is produced by the program PADDING /16/ as input for SAP.

	Material	$E_{xx}=E_{yy}=E_{zz}$ /N/m^2/	$\nu_{xy}=\nu_{yz}=\nu_{zx}$	$G_{xy}=G_{yz}=G_{zx}$ /N/m^2/
Coil	Stainless steel	2×10^{11}	0.3	7.69×10^{10}
	Copper (1/2-hard)	1×10^{11}	0.3	3.85×10^{10}
	Copper-steel compound	1.5×10^{11}	0.3	5.77×10^{10}
Support structure	Stainless steel	2×10^{11}	0.3	7.69×10^{10}
Padding	Epoxy	1.2×10^{10}	0.3	4.6×10^{9}

Table IV: Material data at 4.2 K.

The support structures of coils 1 and 5 are now shown in Figs. 41 and 42, respectively. It is the "ring concept" described in Ref. /17/ that is applied. An outer ring is used because there is no space for support structure at the inner side of the coils. Lateral support is applied at locations of lateral force densities in the related direction (see Figs. 38 and 40) in order to achieve that the paddings are under compression. The thickness of the padding is chosen to be 10 cm. Thus the coil is allowed to expand by some amount, but the side paddings are still under compression. The maximum value of the compression stress in the paddings is about 100 MPa. The thickness of the outer ring is chosen to be 60 cm, see Figs. 41 and 42. The maximum value of the reference stress (von Mises stress) in the outer ring is about 50 MPa.

For the support concept it is very important that the support structure is held at the outside with rigid boundary elements (stiffness 10^{17}Pa). That means that the outer ring has to be equipped with additional structure elements. The side structure, which is also held by rigid boundary elements in the present model, should be held by mutual support between adjacent coils in a further step.

Fig. 41 shows coil 1, Fig. 42 coil 5, each with outer ring and lateral support structure. Figs. 43 to 49 show the stresses in the microelements over the coil circumference for coil 1, Figs. 50 to 56 the corresponding stresses for coil 5. The results of the calculations show that the "ring concept" appreciably reduces the stress values in the coil compared with the conventional support /5/. This is due to the minimization of the bending moments in the coil /17/. The maximum value of the reference stress (von Mises stress) occurs at GCE 38 of coil 1 and is about 80 MPa if the filling factor of the coil of 0.8 is taken into account.

Figs. 57 and 58 show the deflection of coil 1, Figs. 59 and 60 that of coil 5. Because of the rigid boundary elements the maximum value of the deflection is only about 1.1 mm.

5. Conclusions

Modular stellarator coil systems of the WENDELSTEIN VII-AS type with reactor dimensions are investigated. The coil configuration ASR25T7 is considered as optimized regarding the magnetic topology, rotational transform, and aspect ratio, if a distance Δ = 1.8 m is required for first wall, blanket, shield, dewar and coil housing.

The technical constraints with respect to the superconducting technology of NbTi at 4.2 K are satisfied. Forces and stresses of the coil system have been calculated using a support scheme which was proposed in Ref. /17, 18/. This "ring-type" outer support concept with elastic paddings minimizes the bending stresses within the coils. The peak value of the reference stress (von-Mises-stress) is reduced to an uncritical value of about 80 MPa. Further investigations are intended to optimize the support scheme. Particulary it appears necessary to investigate the mutual support between adjacent coils. Out of the scope of this paper are the engineering problems associated with low temperatures which are required for the superconductivity, and the transfer of forces across the thermal insulation.

6. References

/1/ Rau, F., Kisslinger, J., Wobig, H., Vacuum Magnetic Field and Modular Coil System of the Advanced Stellarator WENDELSTEIN VII-AS, Report IPP 2/259 June 1982
and
Proceedings 12th SOFT, Jülich (1982) 1051.

/2/ Sapper, J., Brossmann, U., Grieger, G., Kisslinger, J., Mukherjee, S., Rau, F., Sombach, B., Wobig, H., The Advanced Stellarator WENDELSTEIN VII-AS, Proceedings 12th SOFT, Jülich (1982) 161.

/3/ Brossmann, U., Kerl, F., Melchior, W., Mukherjee S., Sapper, J., Sombach, B., Modular Mechanical Design of the Advanced Stellarator WENDELSTEIN VII-AS, Proceeding 12th SOFT, Jülich (1982) 915.

/4/ Brossmann, U., Mukherjee, S., Sapper, J., Computational Aspects for a Modular Stellarator Fusion Reactor Magnet, Proceedings 12th SOFT, Jülich (1982) 985.

/5/ WENDELSTEIN VII-AS: Reactor Considerations, 17.-18.2. 1982, Internal IPP-Report.

/6/ Dommaschk, W., Solution to Stellarator Boundary Value Problems with a new Set of Simple Toroidal Harmonic Functions, Zeitschrift für Naturforschung 36a (1981) 251.

/7/ Dommaschk, W., Simple Series of Harmonic Functions for Representing Arbitrary, Non-singular Vacuum Fields in Toroidal Regimes in Reduce and Fortran Representation, Report IPP 0/38 Okt. 1978.

/8/ Sackett, S.J., EFFI - A code for calculating the electromagnetic field, force, and inductance in coil systems for arbitrary geometry, Lawrence Livermore Laboratory, Report UCRL-52402 (1978).

/9/ Gourdon, C., Marty, D., Maschke, E.K., Dumont, J.P., Configurations du type stellarator avec puits moyen et cisaillement des lignes magnetique, Proceedings 3rd Int. Conference on Plasma Physics and Controlled Nuclear Fusion Research, Novosibirsk (1968), 847.

/10/ Rau, F., Short communication at Stellarator-Workshop, Cap May (1982)
and
Gorenflo, H., Harmeyer, E., Kisslinger, J., Raeder, J., Wobig, H., Rau, F., Zur Reaktoreignung modularer Stellaratorspulen, Verhandlungen DPG Regensburg (1983) 376.

/11/ Brossmann, U., Gorenflo, H., Harmeyer, E., Kisslinger, J., Raeder, J., Rau, F., Wobig, H., Some Aspects of an Advanced Stellarator Reactor, 11th European Conference on Controlled Fusion and Plasma Physics, Aachen (1983) to be published.

/12/ Brossmann, U., Dommaschk, W., Herrnegger, F., Grieger, G., Kisslinger, J., Lotz, W., Nührenberg, H., Rau, F., Renner, H., Ringler, H., Sapper, J., Schlüter, A., Wobig, H., Concept of an Advanced Stellarator, 9th International Conference on Plasma Physics and Controlled Nuclear Fusion Research, Baltimore (1982).

/13/ Söll, M., Superconducting magnet systems for fusion reactors, Kerntechnik 19. Jahrg. (1977) No. 6 272.

/14/ Raeder, J., et al., Kontrollierte Kernfusion, Verlag Teubner Stuttgart (1981) 228.

/15/ Küpfmüller, K., Einführung in die theoretische Elektrotechnik, Springer Verlag Berlin (1973).

/16/ Mukherjee, S.B., Gorenflo, H., Harmeyer, E., PADDING - A program to generate padded support structure for modular coils, Report IPP in preparation

/17/ Mukherjee, S.B., Ring-type support concept for twisted coils (FE-Simulation), Report IPP 2/271 December 1983

/18/ Brossmann, U.B., Mukherjee, S.B., New Supporting Concept for Large Twisted Coils, Proceedings 12th SOFT, Jülich (1982) 979.

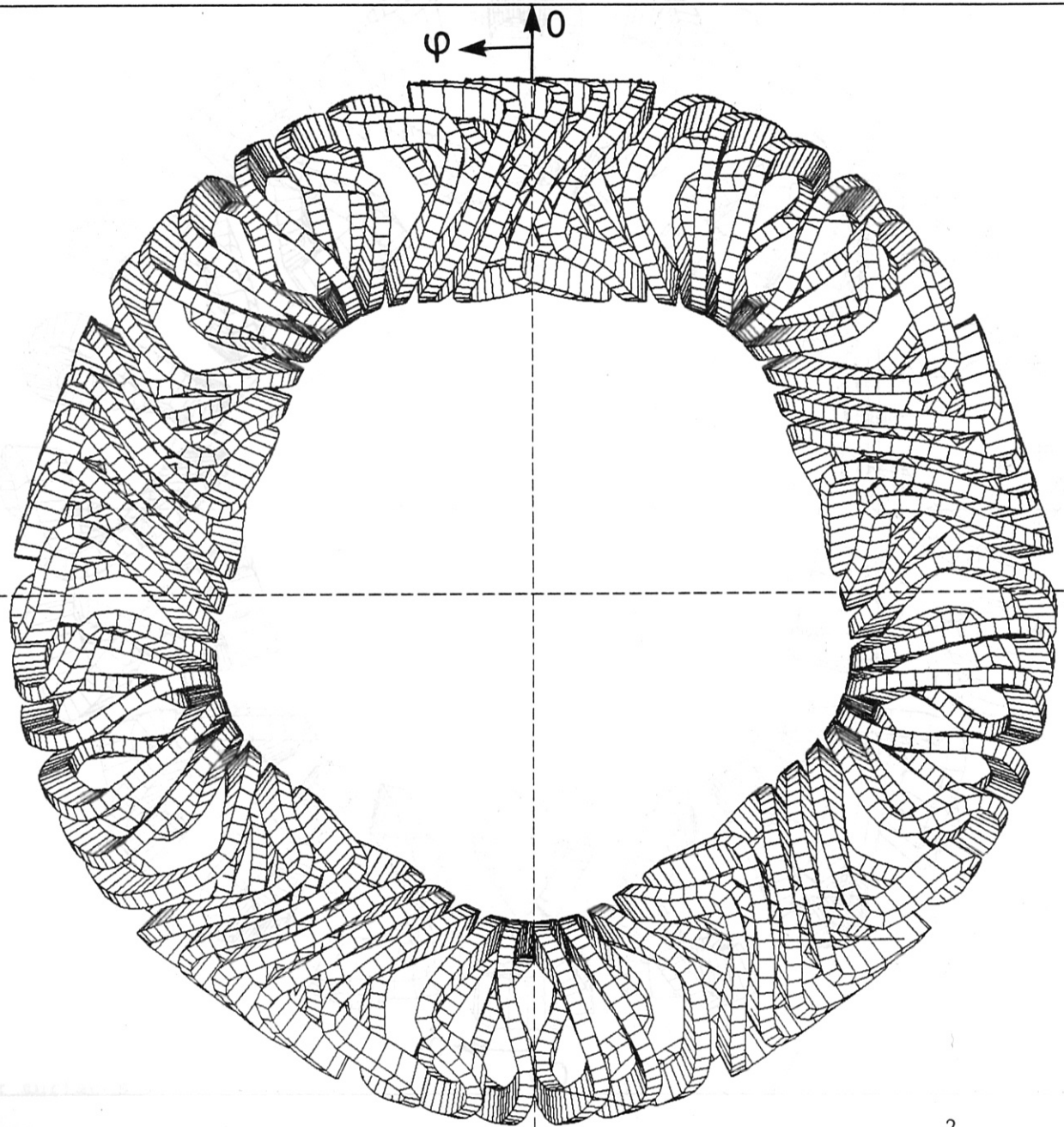

Fig. 1:

ASR2510 TOP VIEW Y=-90, S=0.0025 <j> = 6.86 MA/m^2 10 coils per F.P.

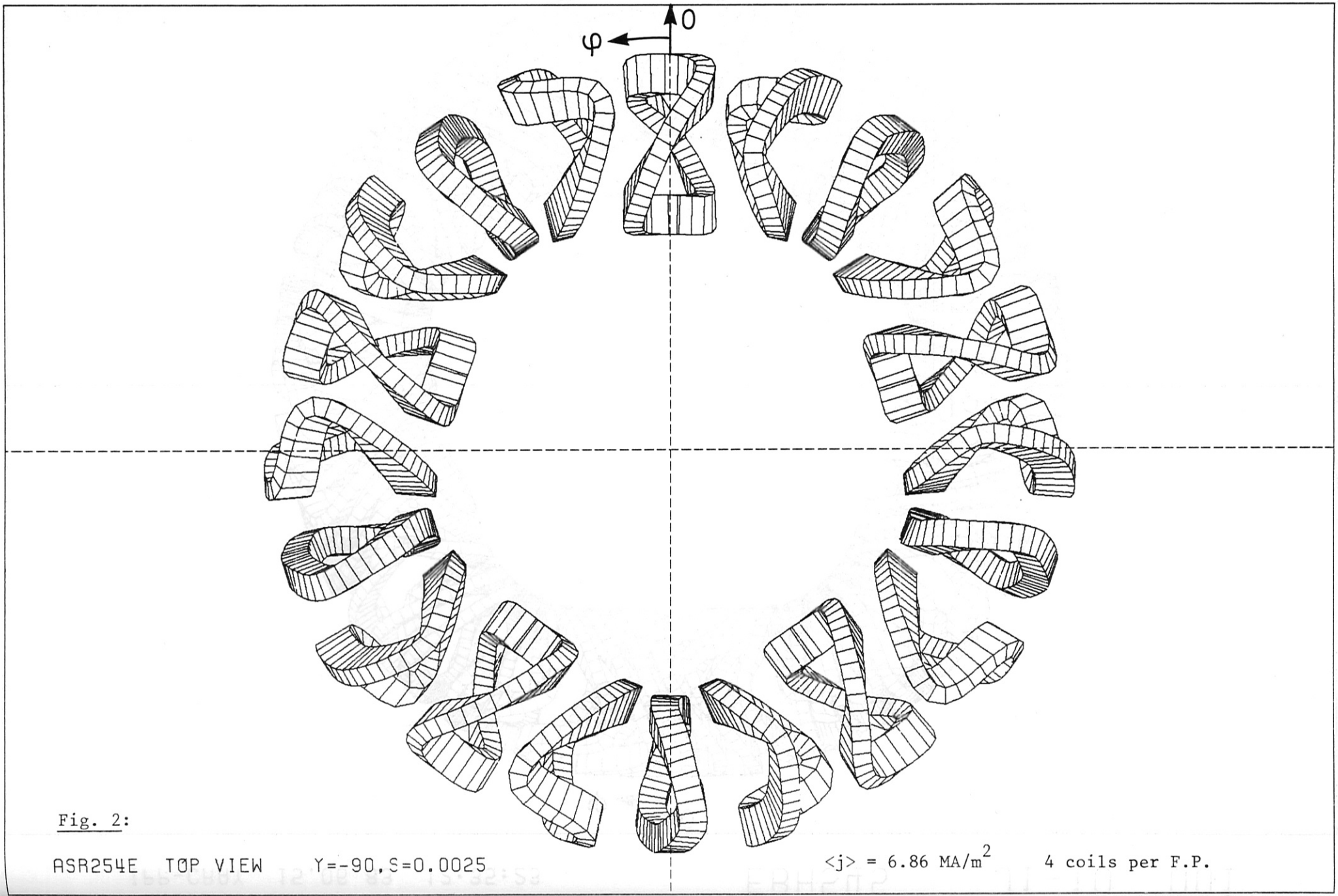

Fig. 2:

ASR254E TOP VIEW Y=-90, S=0.0025 <j> = 6.86 MA/m^2 4 coils per F.P.

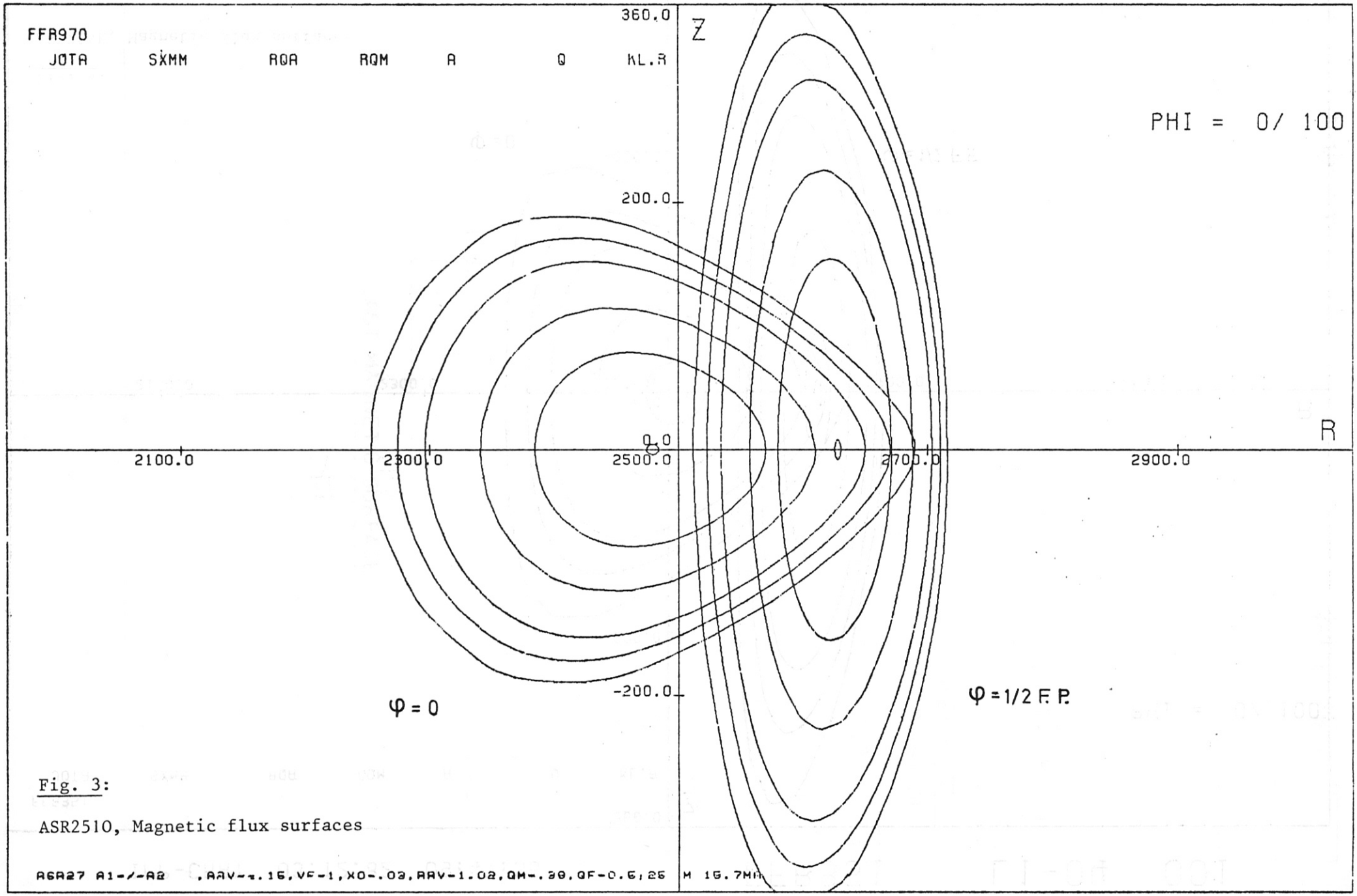

Fig. 3:

ASR2510, Magnetic flux surfaces

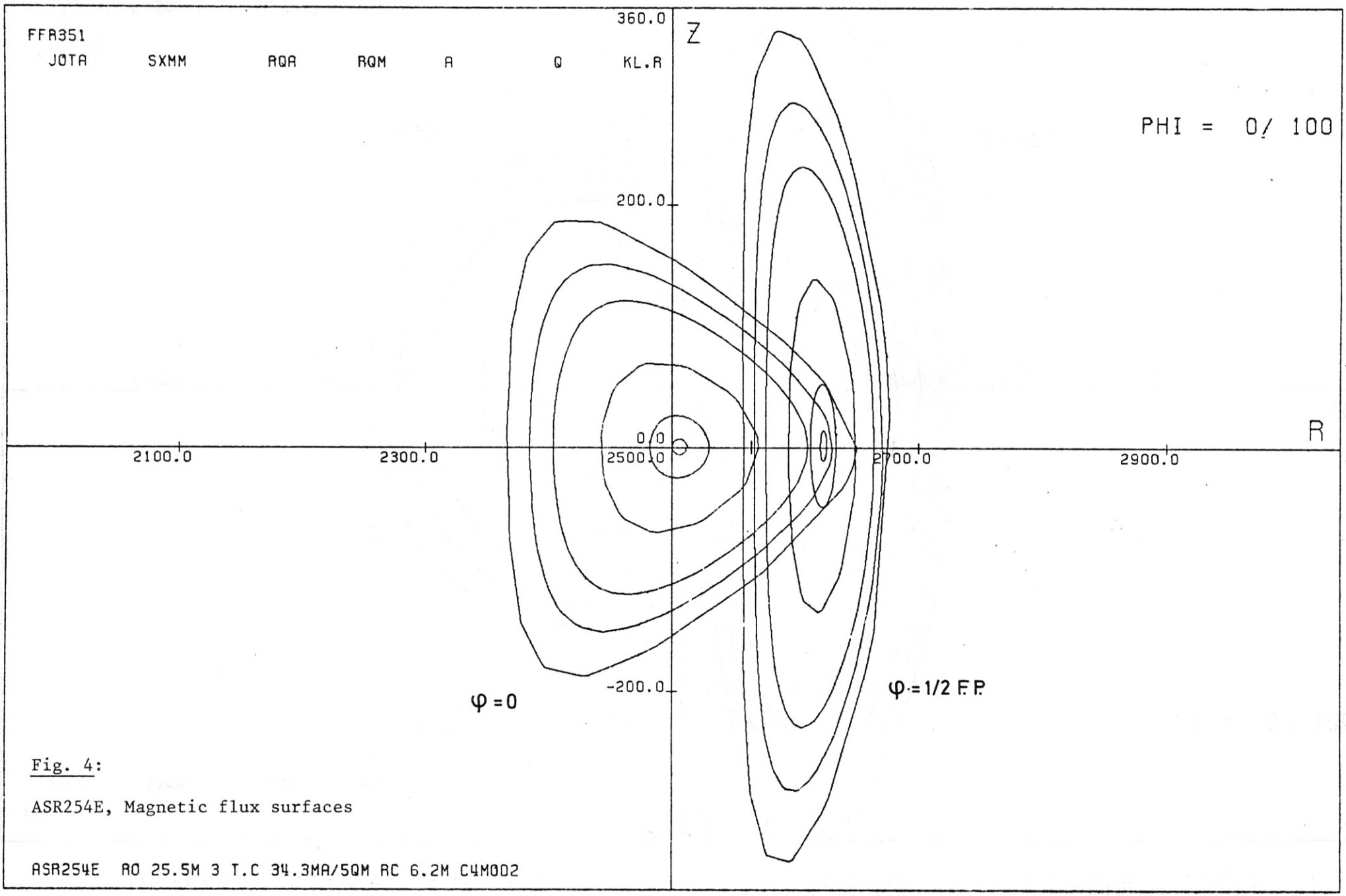

Fig. 4:

ASR254E, Magnetic flux surfaces

ASR254E RO 25.5M 3 T.C 34.3MA/5QM RC 6.2M C4M002

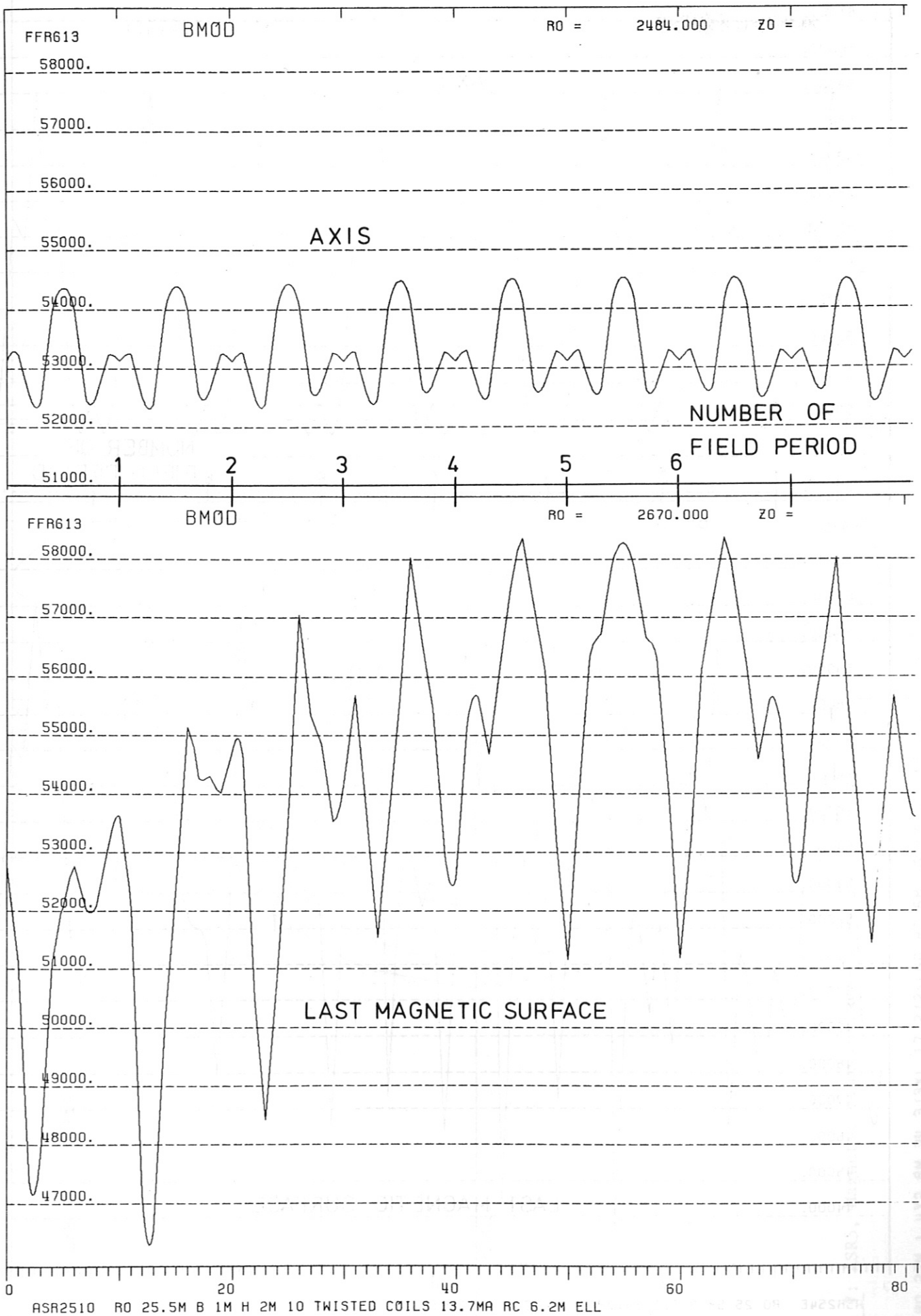

Fig. 5: ASR2510, Magnetic ripple

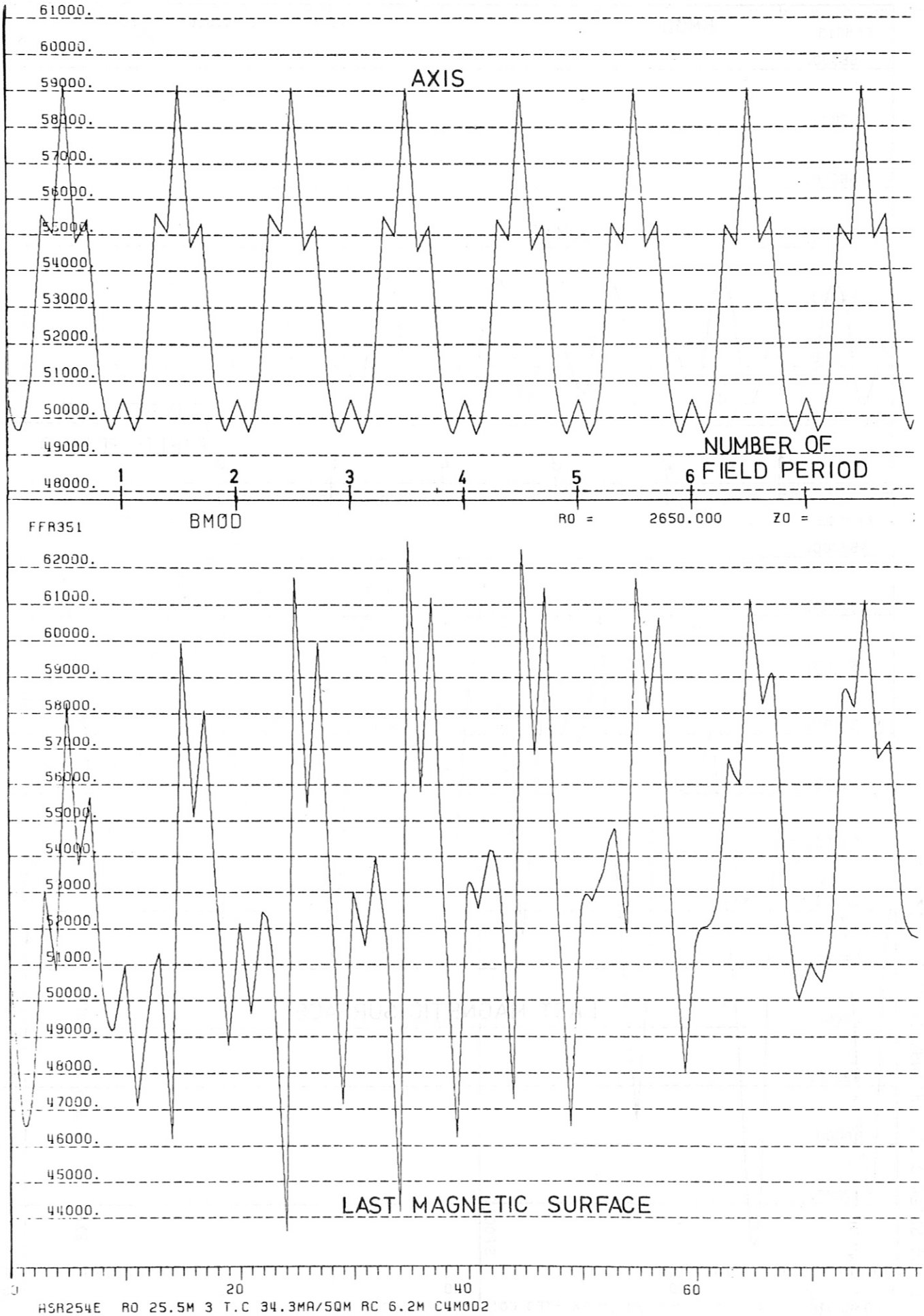

Fig. 6: ASR254E, Magnetic ripple

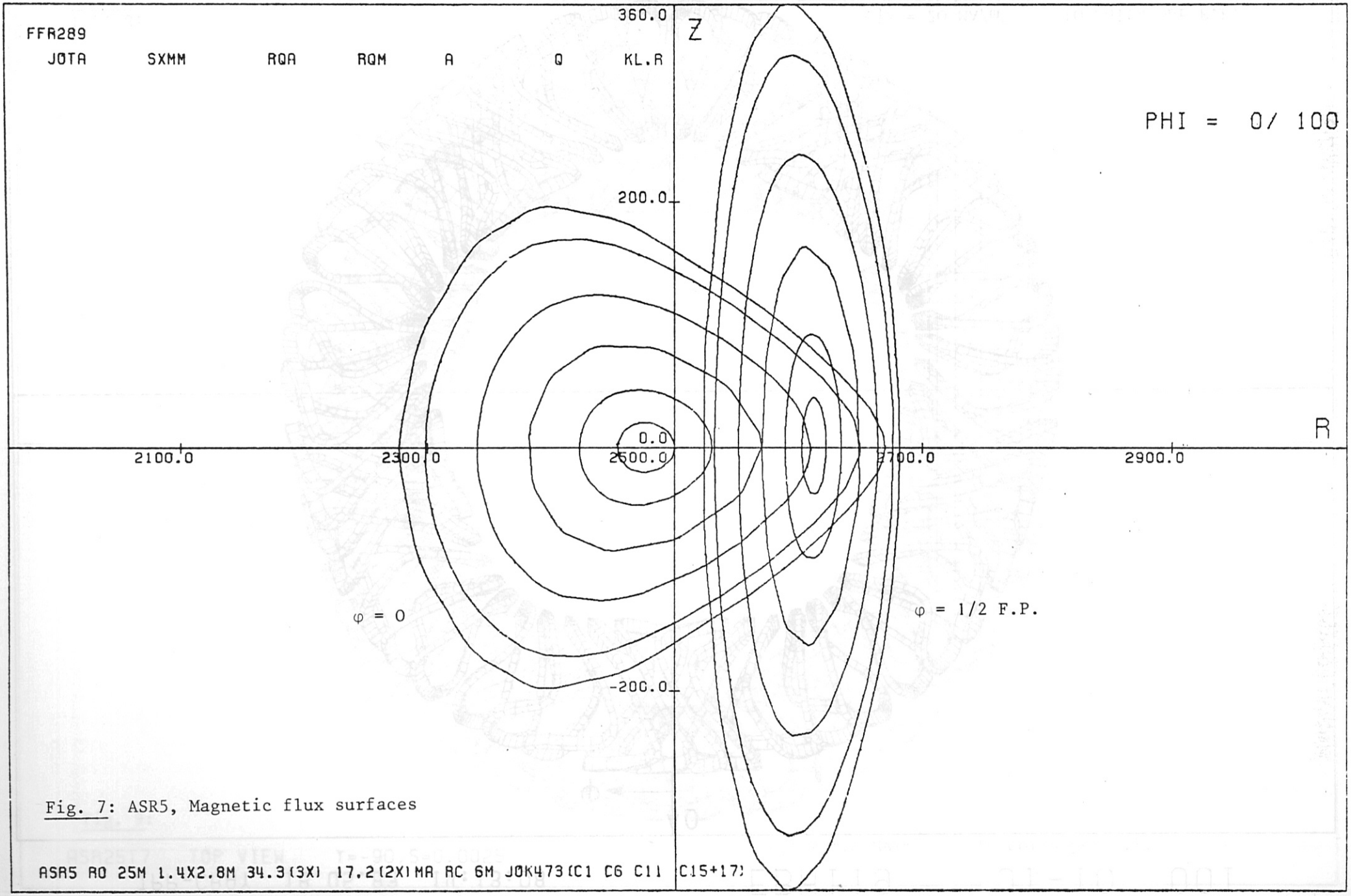

Fig. 7: ASR5, Magnetic flux surfaces

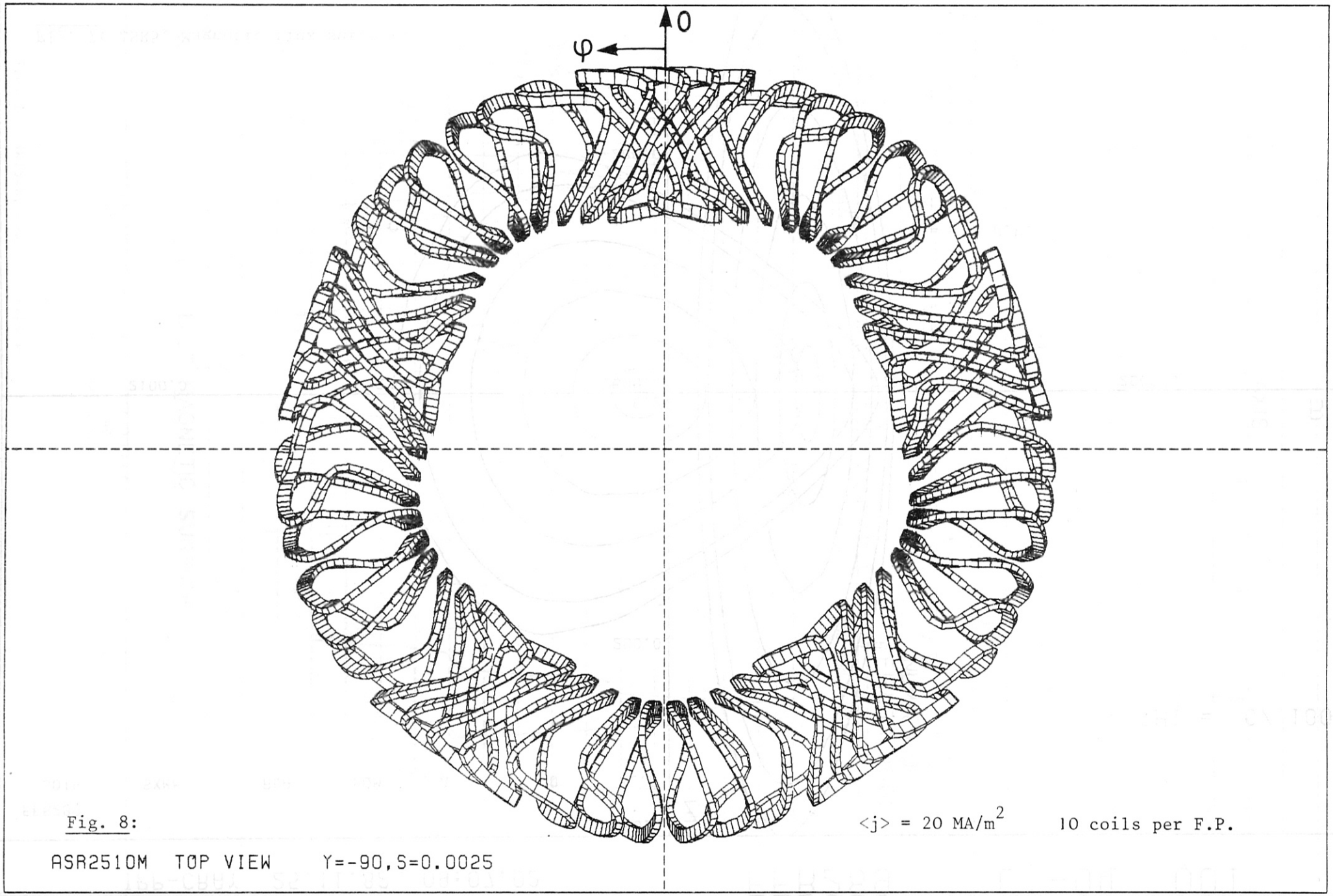

Fig. 8:

<j> = 20 MA/m^2 10 coils per F.P.

ASR2510M TOP VIEW Y=-90,S=0.0025

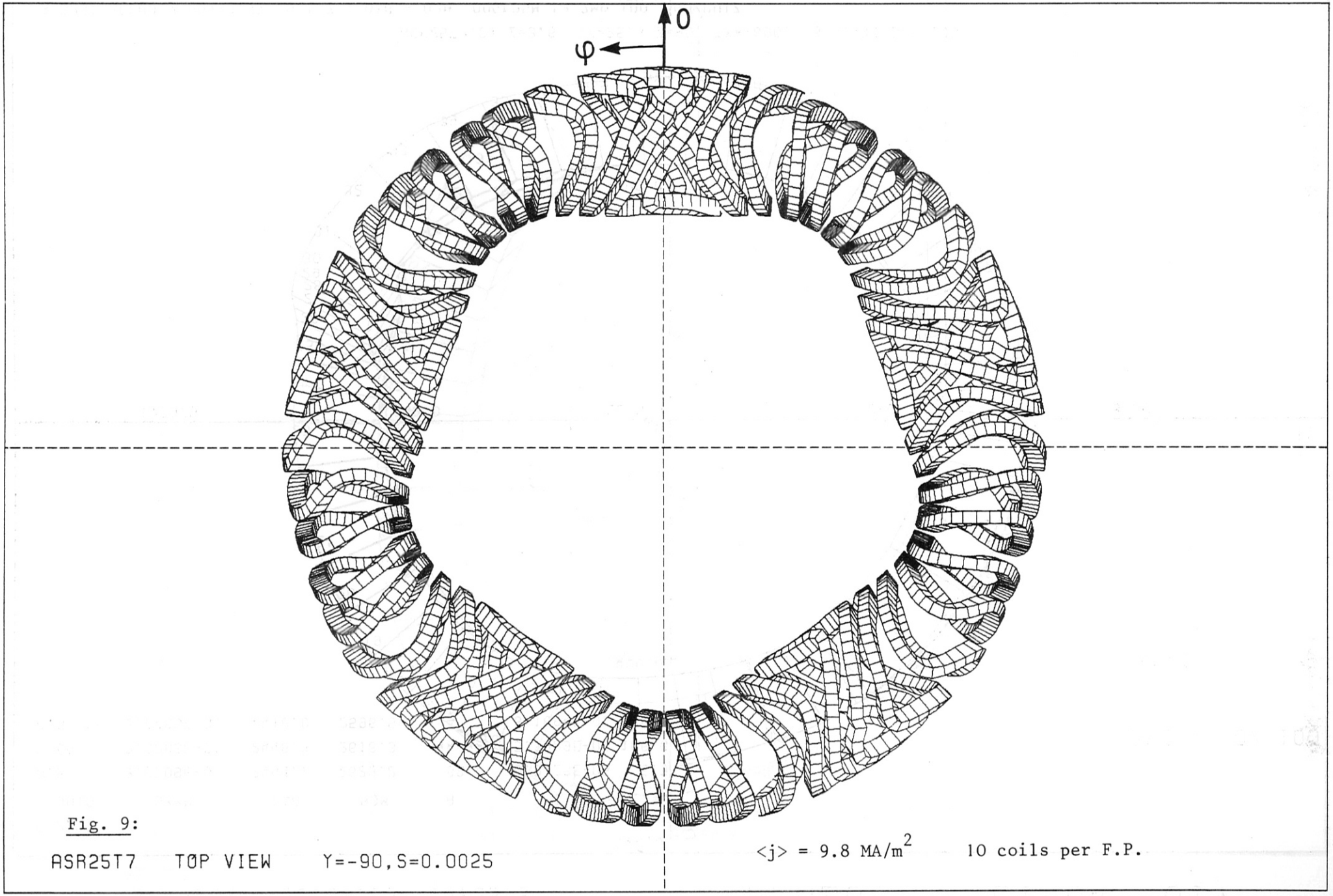

Fig. 9:

ASR25T7 TOP VIEW Y=-90, S=0.0025 $\langle j \rangle = 9.8\ MA/m^2$ 10 coils per F.P.

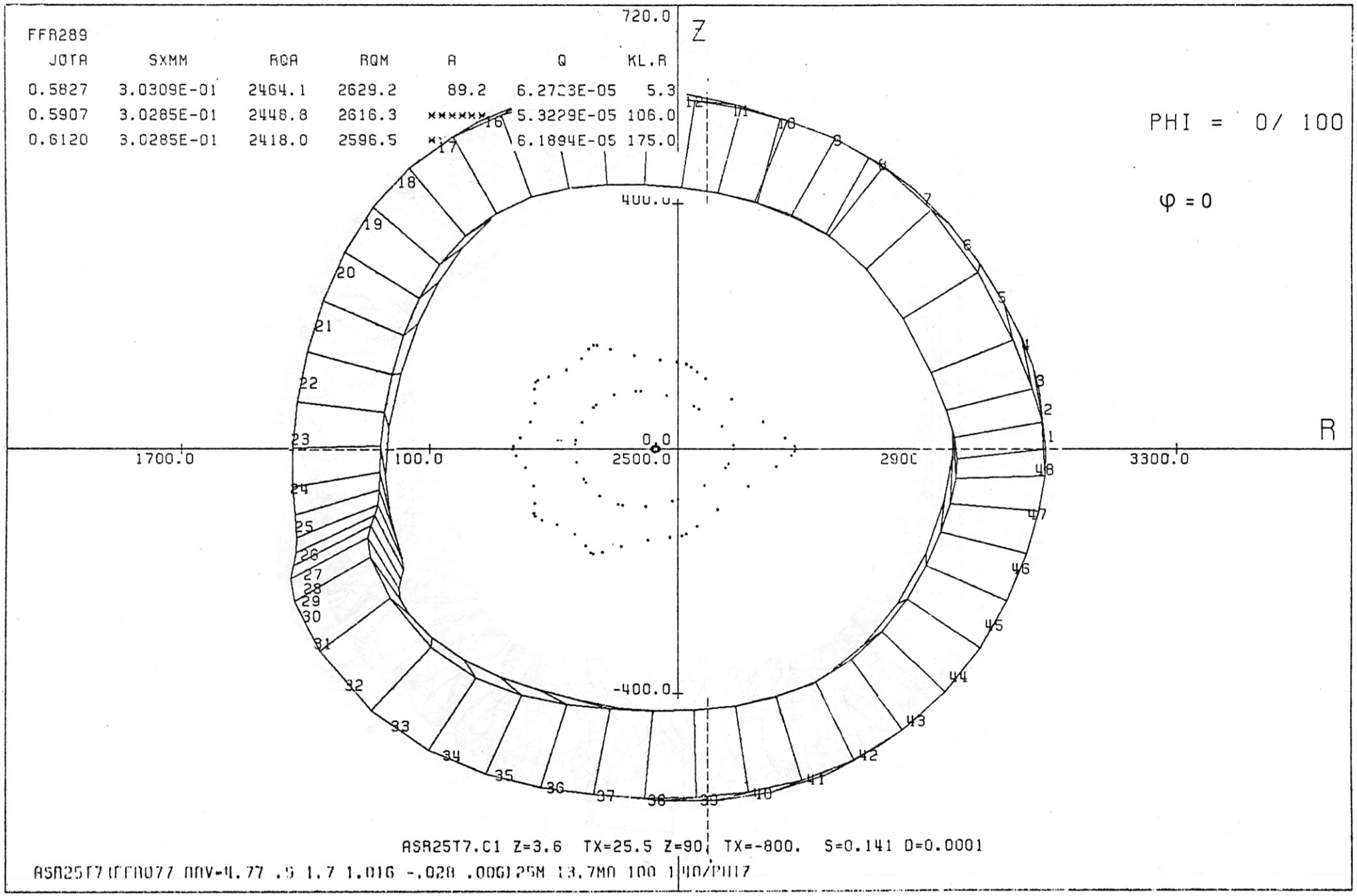

Fig.10: ASR25T7, φ = 0
Coil 1 and magnetic flux surfaces

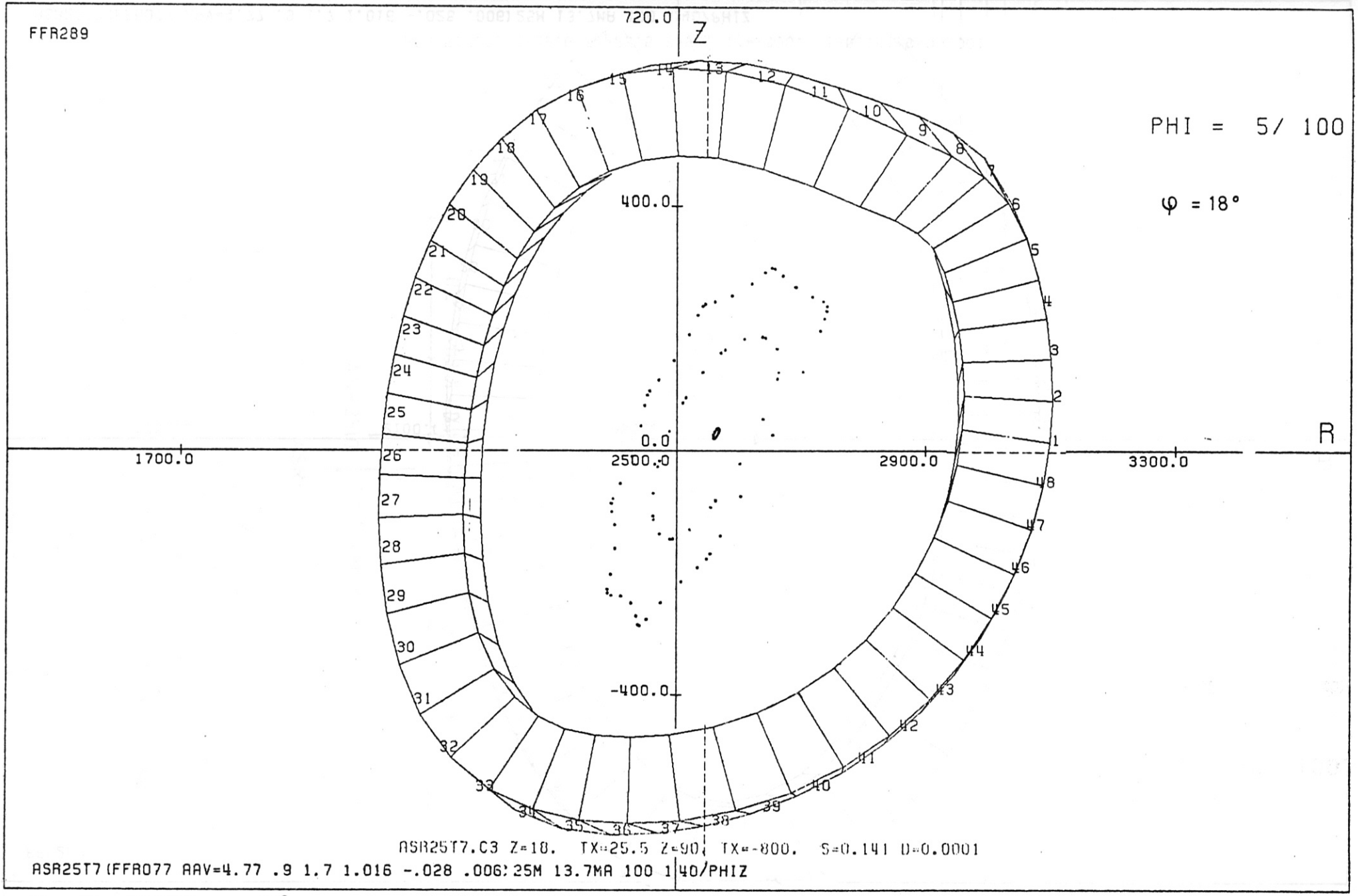

Fig. 11: ASR25T7, $\varphi = 18^{o}$
Coil 3 and magnetic flux surfaces

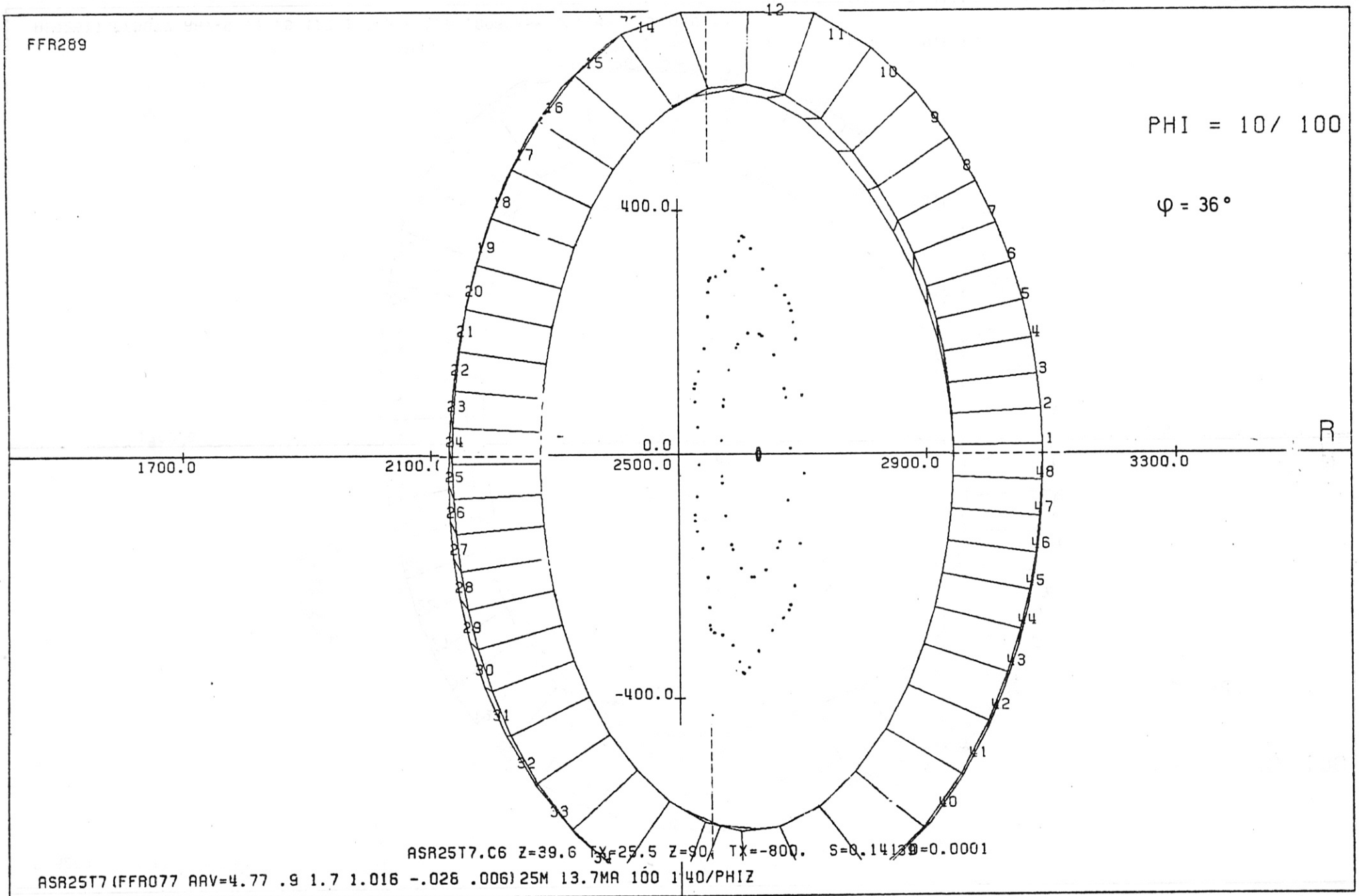

Fig. 12: ASR25T7, $\varphi = 36^{\circ}$
Coil 6 and magnetic flux surfaces

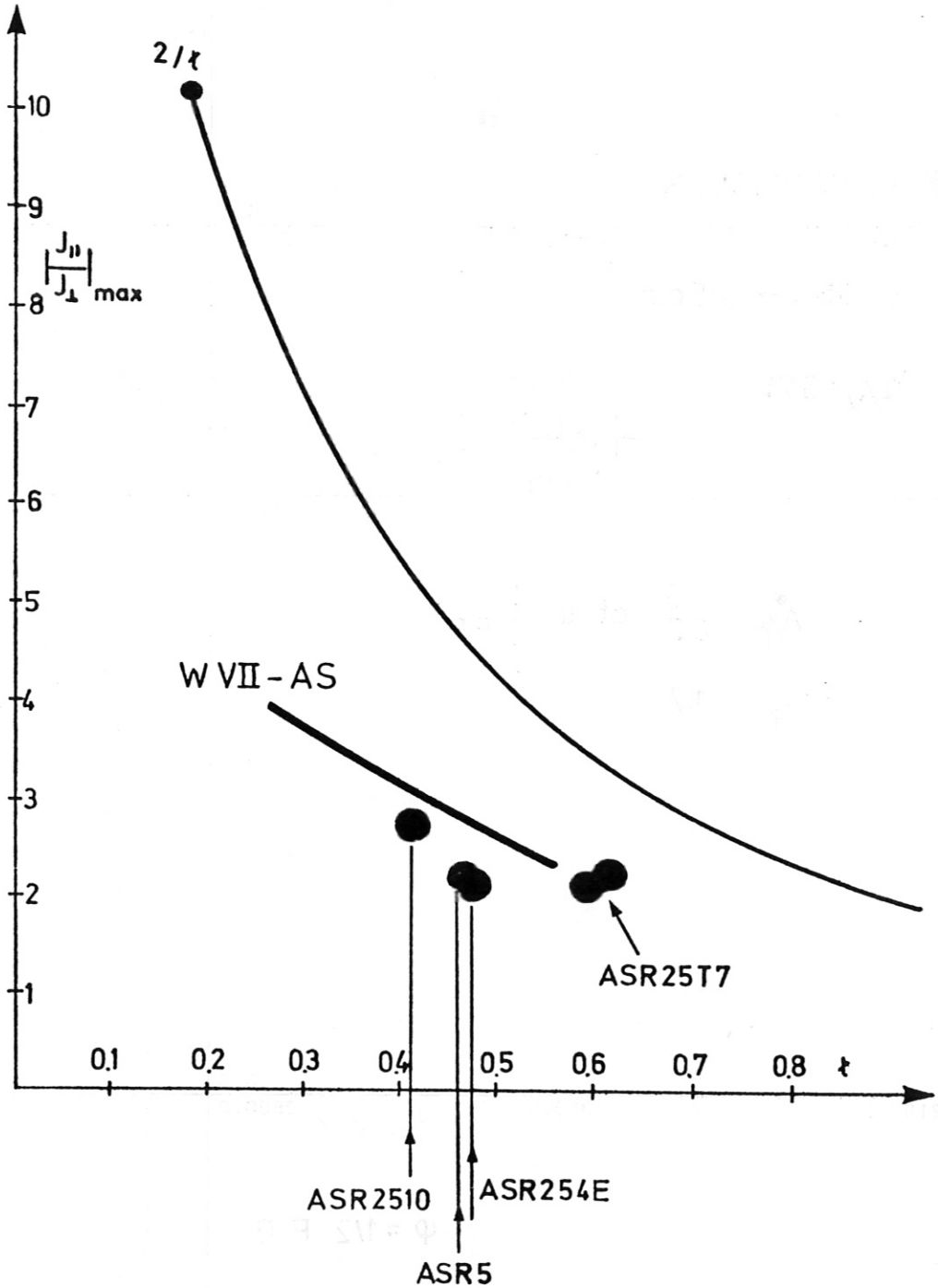

Fig. 13: Maximum ratio $|j_\parallel/j_\perp|_{max}$ vs rotational transform. The dots indicate $|j_\parallel/j_\perp|_{max}$ for the reactor-sized coil configuration of Table II. The curve labelled 2/t corresponds to a "classical" l = 2 stellarator, the bold line W VII-AS indicates $|j_\parallel/j_\perp|_{max}$ of the Advanced Stellarator WENDELSTEIN VII-AS.

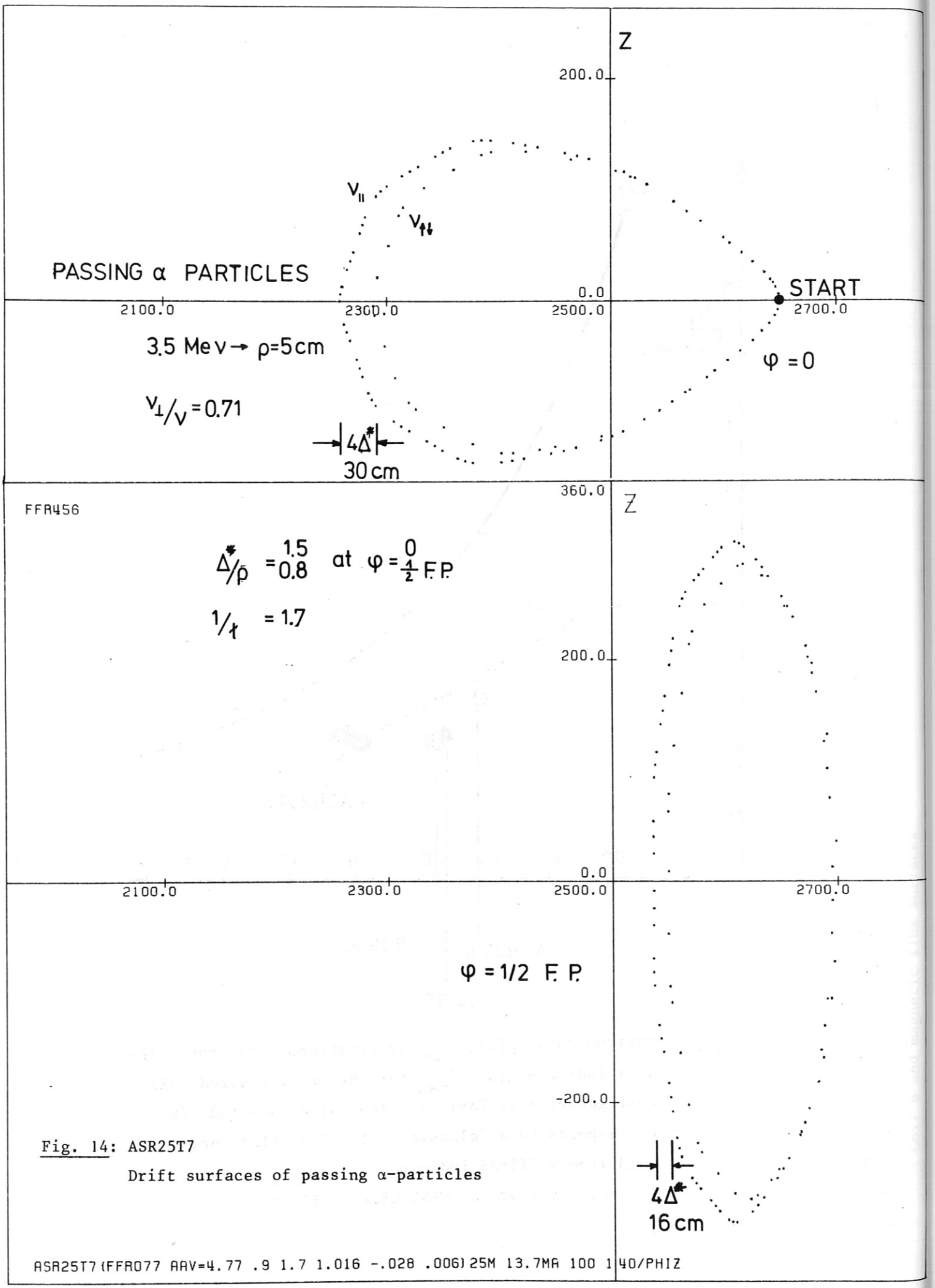

Fig. 14: ASR25T7

Drift surfaces of passing α-particles

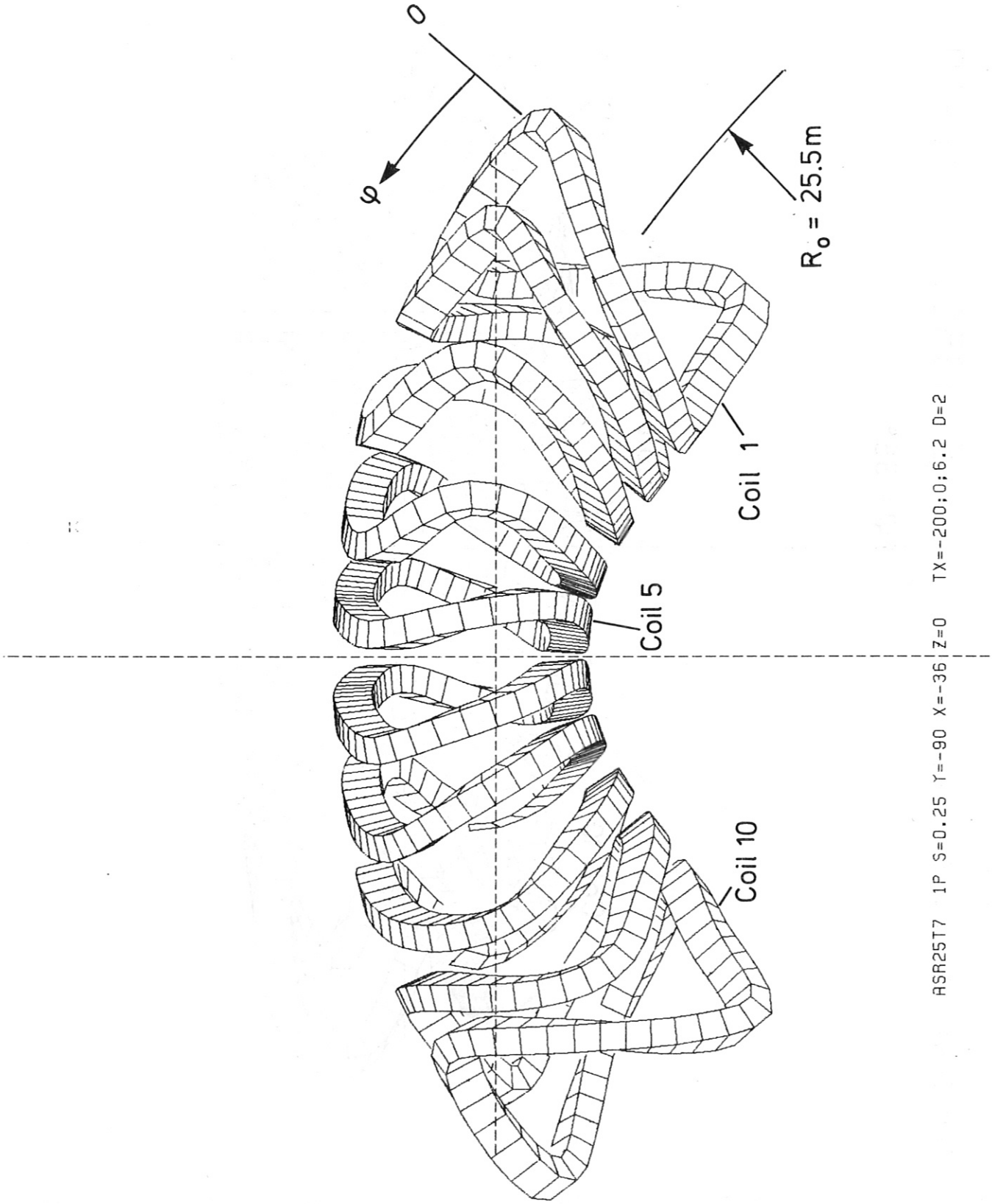

Fig. 15: Coil system of ASR25T7, one field period, top view

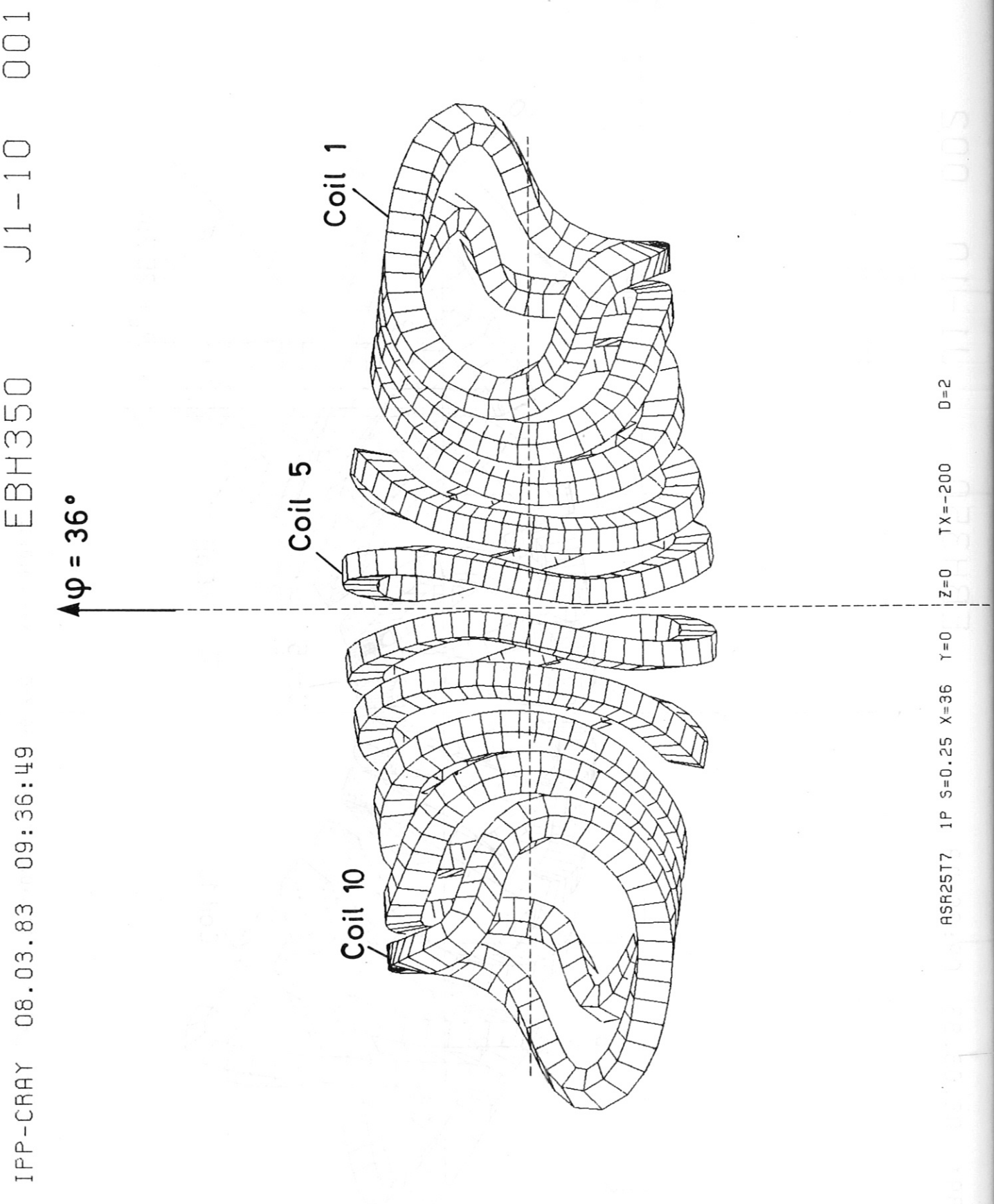

Fig. 16: Coil system of ASR25T7, one field period, side view

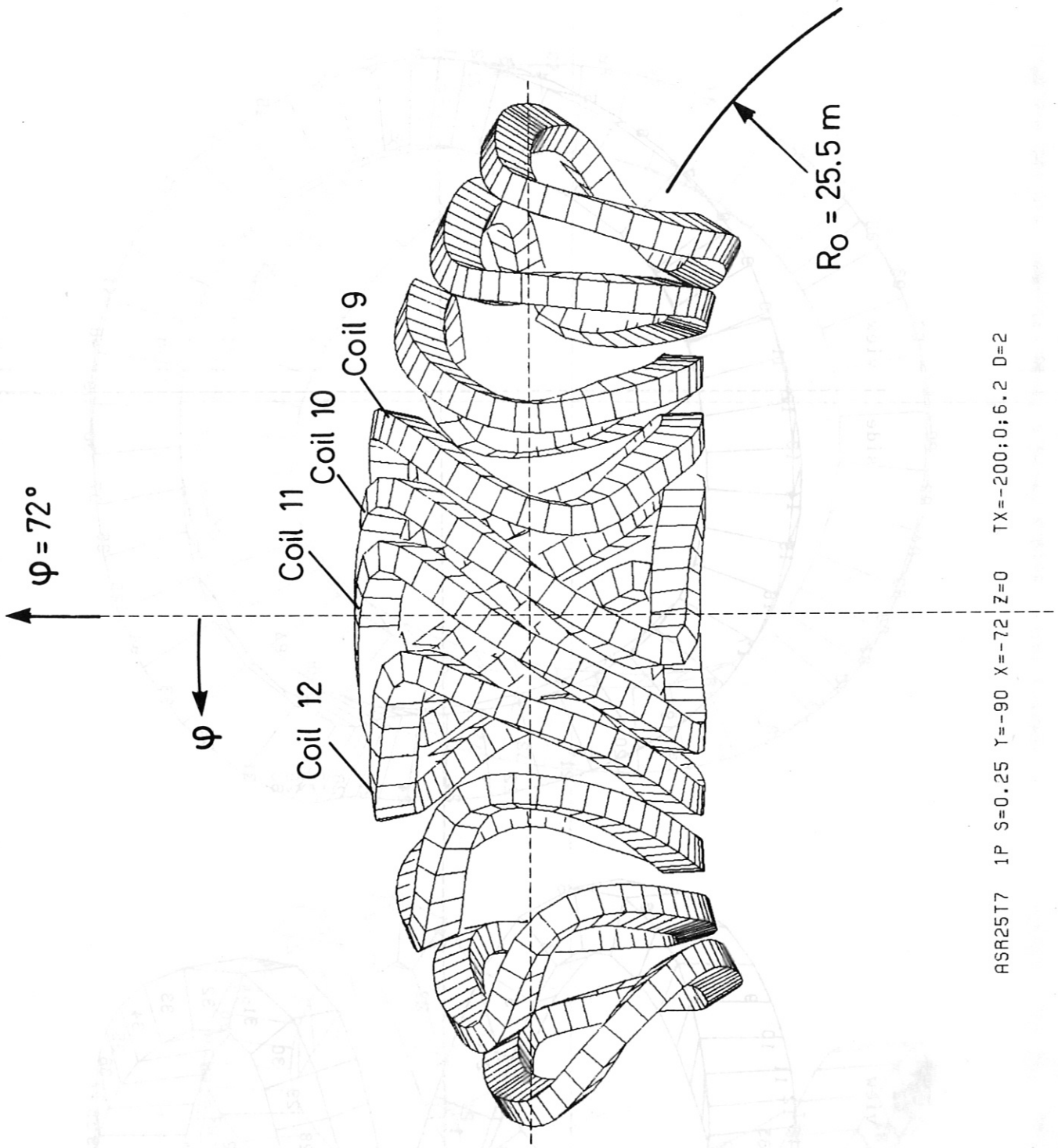

Fig. 17: ASR25T7, top view of one field period centered at $\varphi=72^{o}$

01.08.83 13:42:56

01.08.83 13:42:56

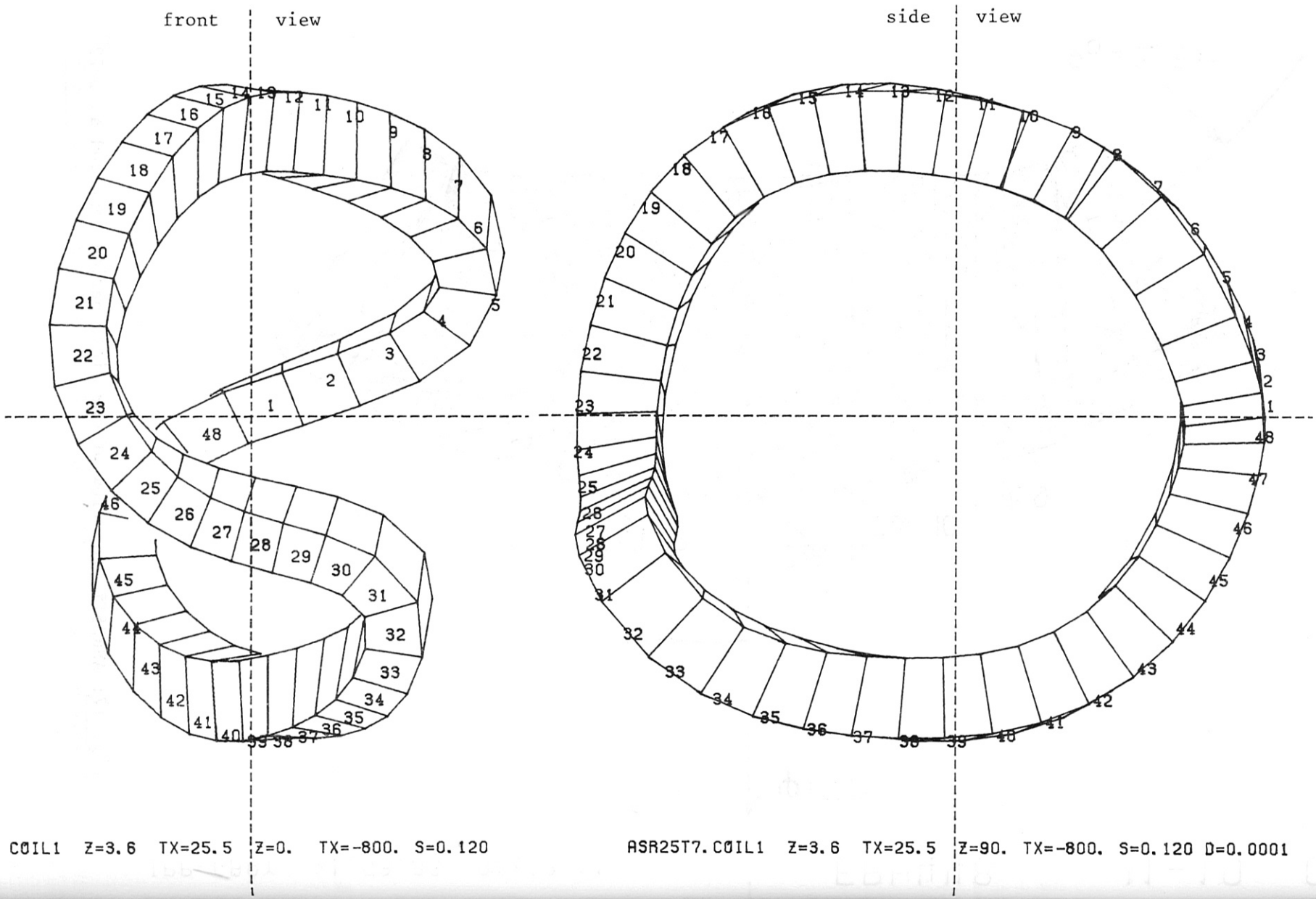

Fig. 18: ASR25T7. Coil 1

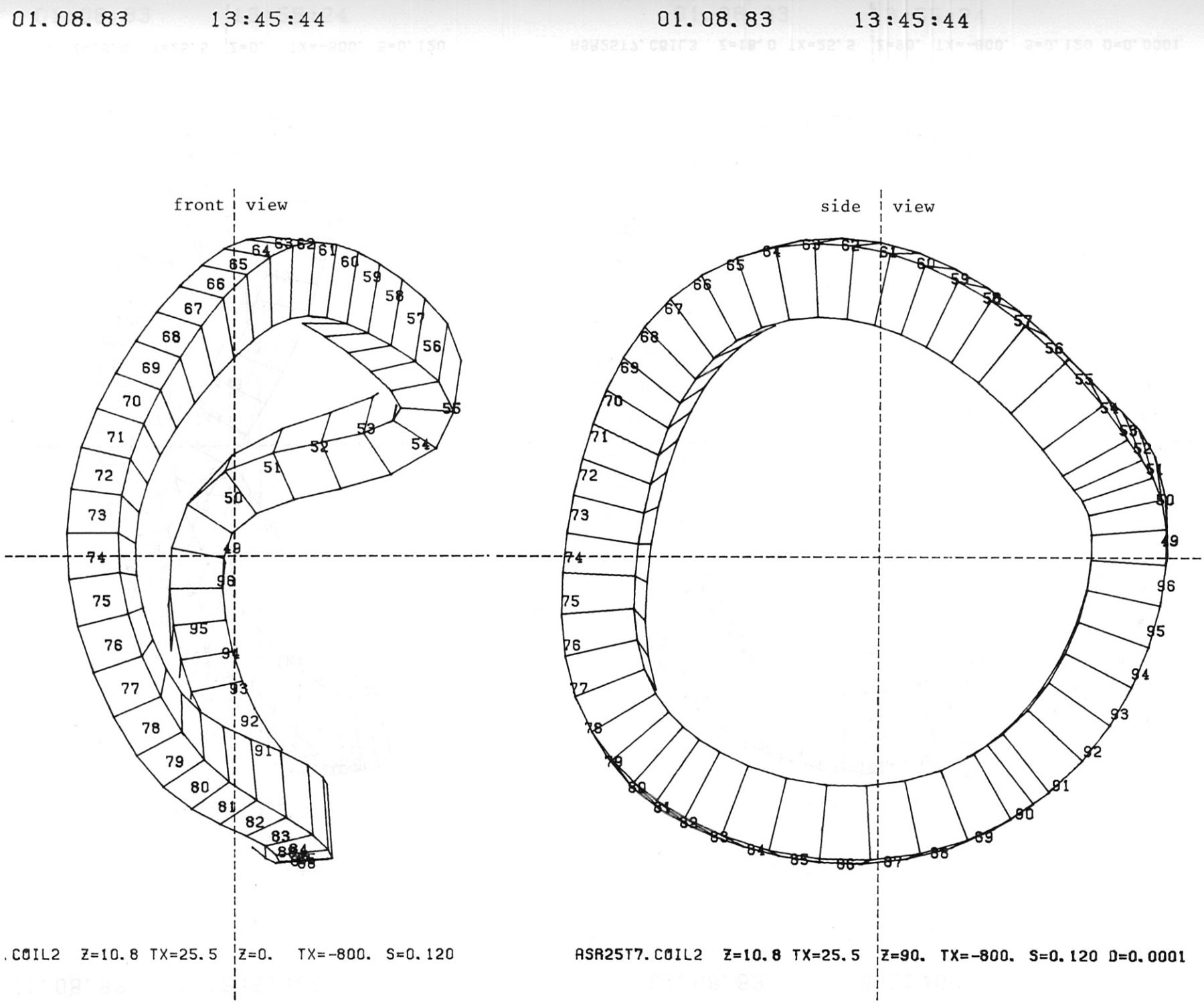

Fig. 19: ASR25T7. Coil 2

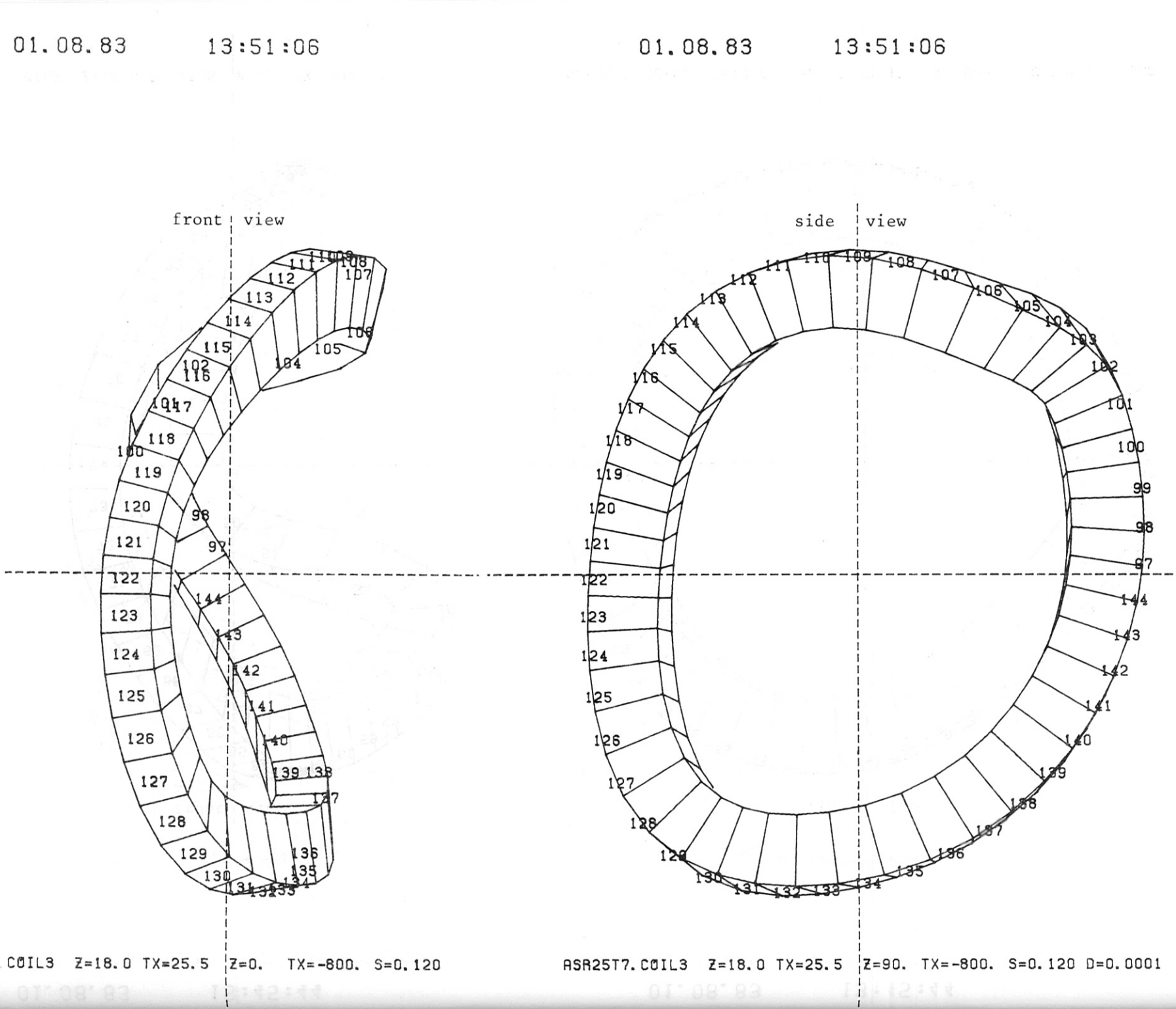

Fig. 20: ASR25T7. Coil 3

01.08.83 13:55:24

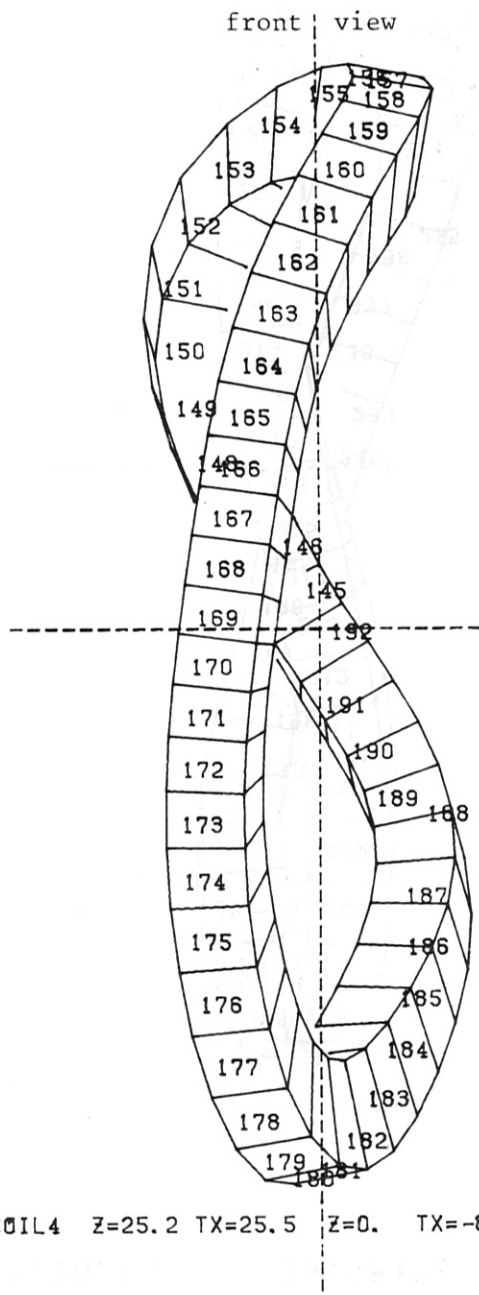

COIL4 Z=25.2 TX=25.5 Z=0. TX=-800. S=0.120

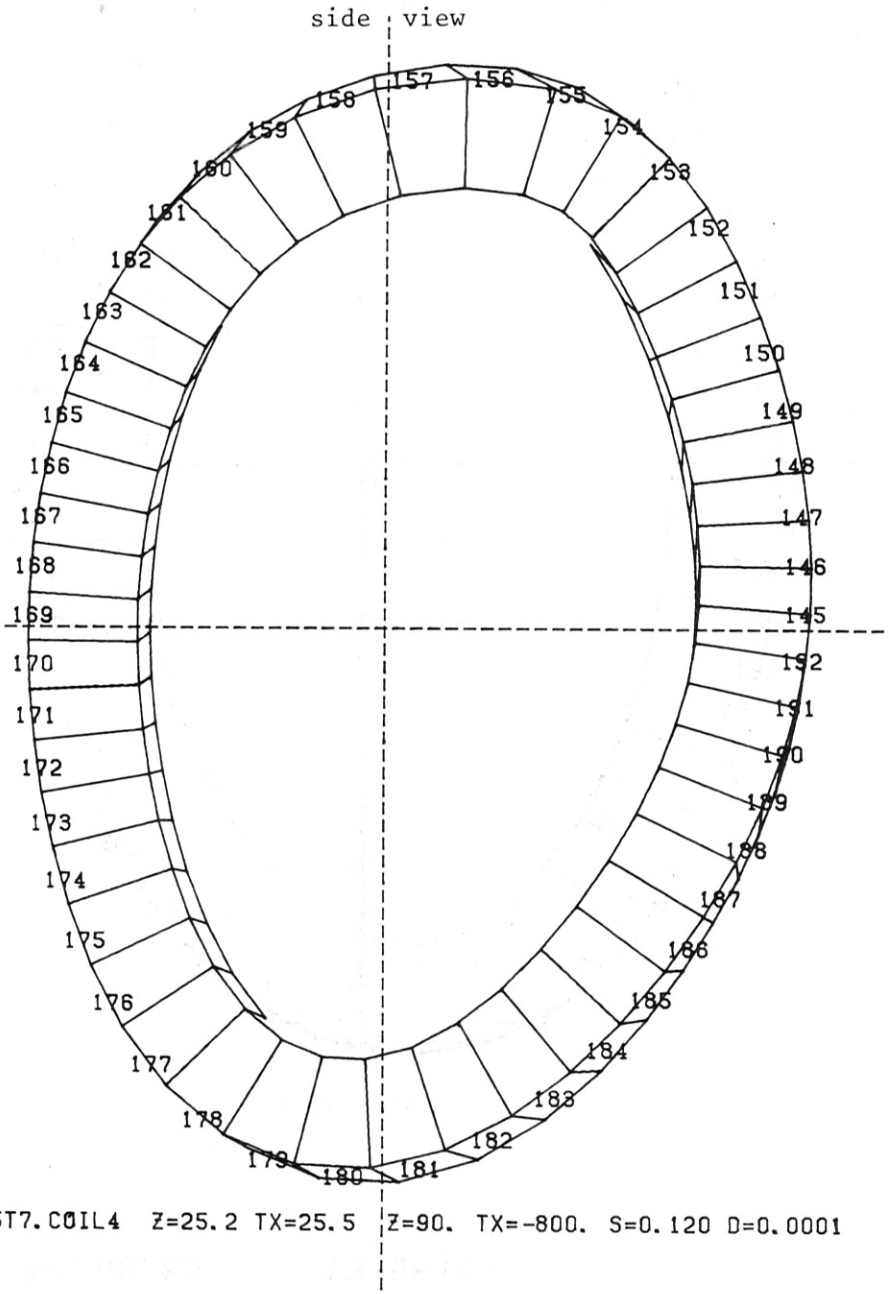

ASR25T7.COIL4 Z=25.2 TX=25.5 Z=90. TX=-800. S=0.120 D=0.0001

Fig. 21: ASR25T7. Coil 4

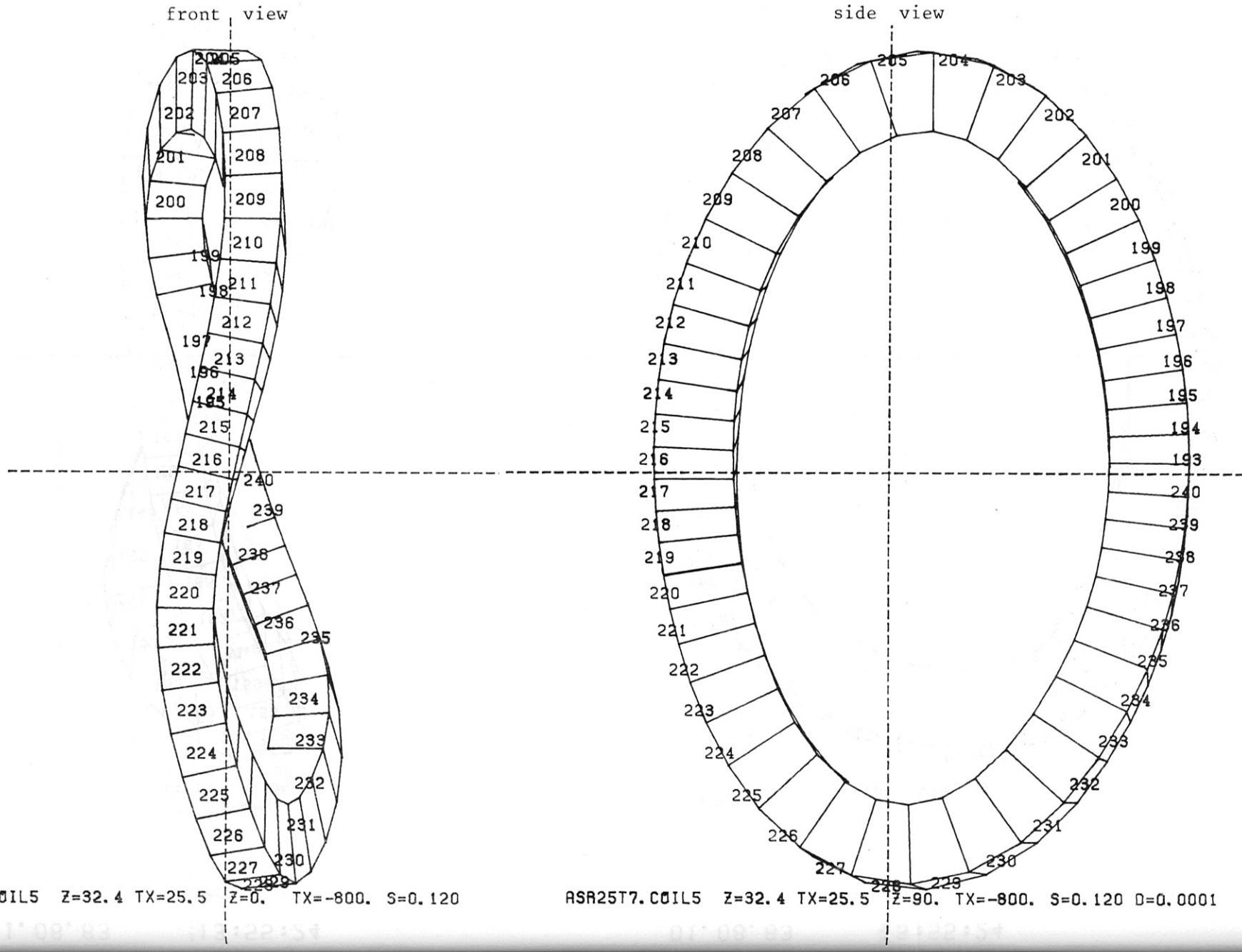

Fig. 22: ASR25T7. Coil 5

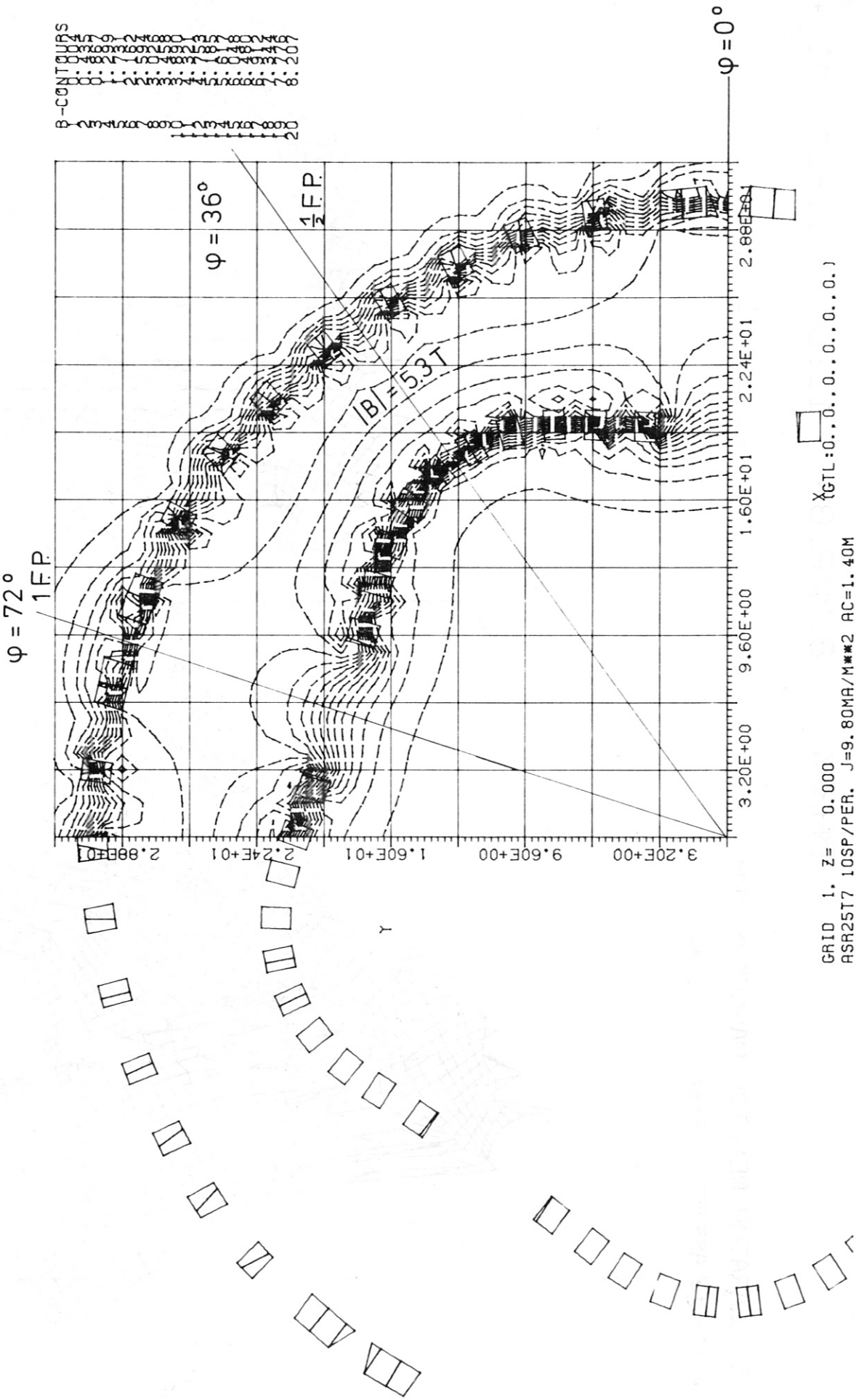

Fig. 23: Contours of constant magnetic flux density of ASR25T7

EBH354 8.MAR.83 11:01 J1-10 01 +

STELLARATOR REAKTOR MAGNETSYSTEM

Variante ASR25T7 Ebene z = 0.00

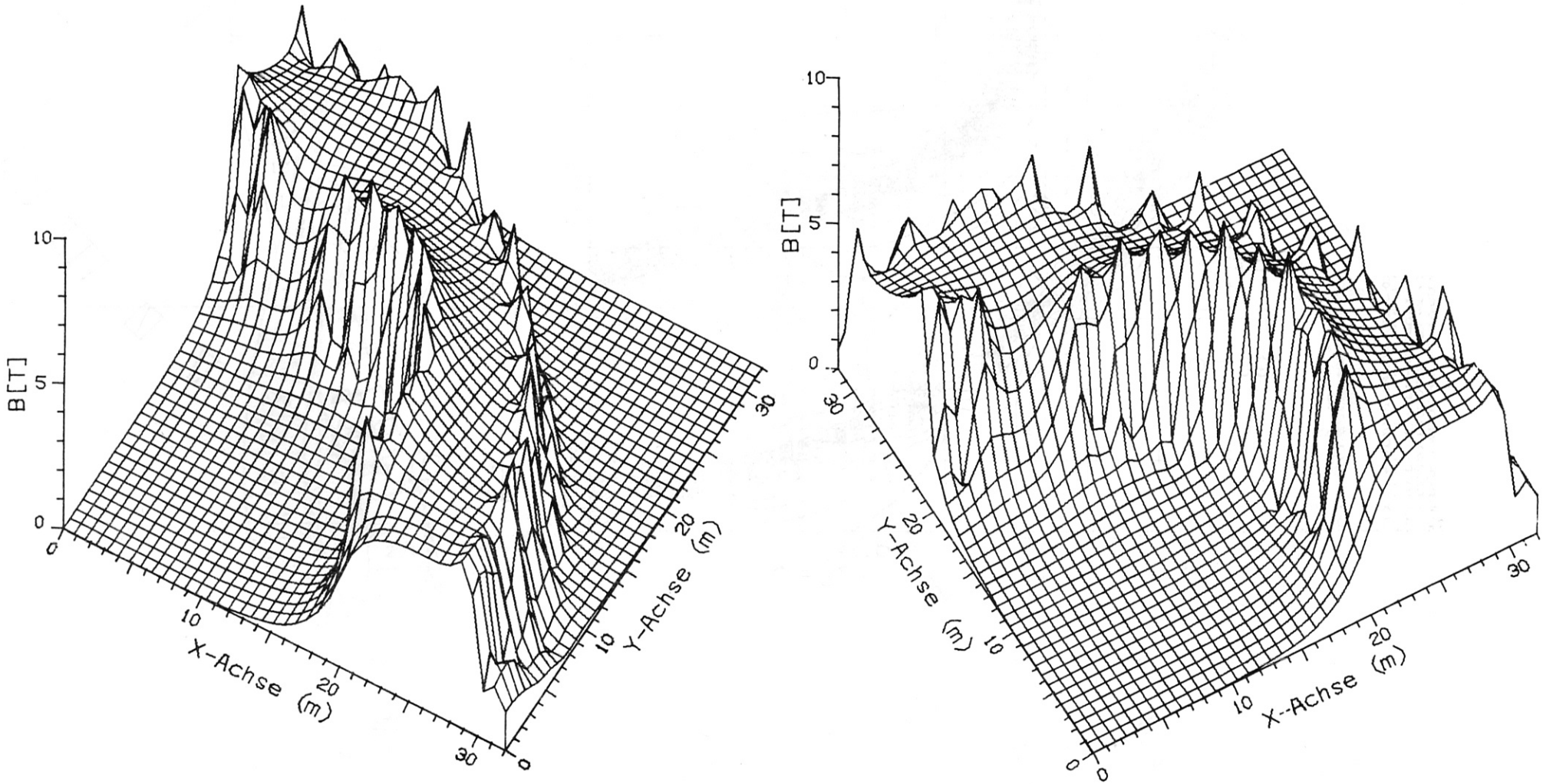

Fig. 24: Magnitude of the magnetic flux density (first quadrant)

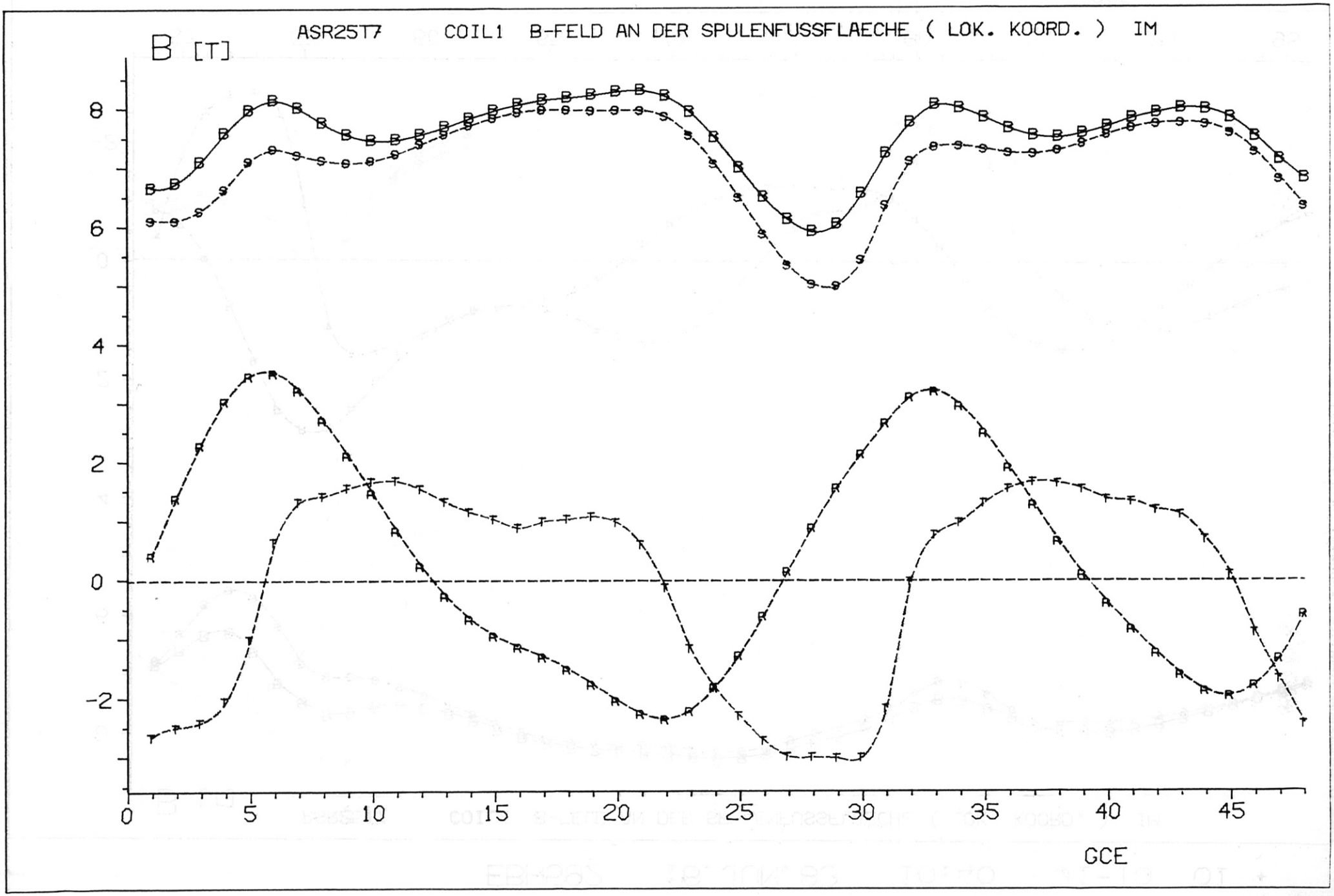

Fig. 25: Magnetic flux density at the inner side of coil 1

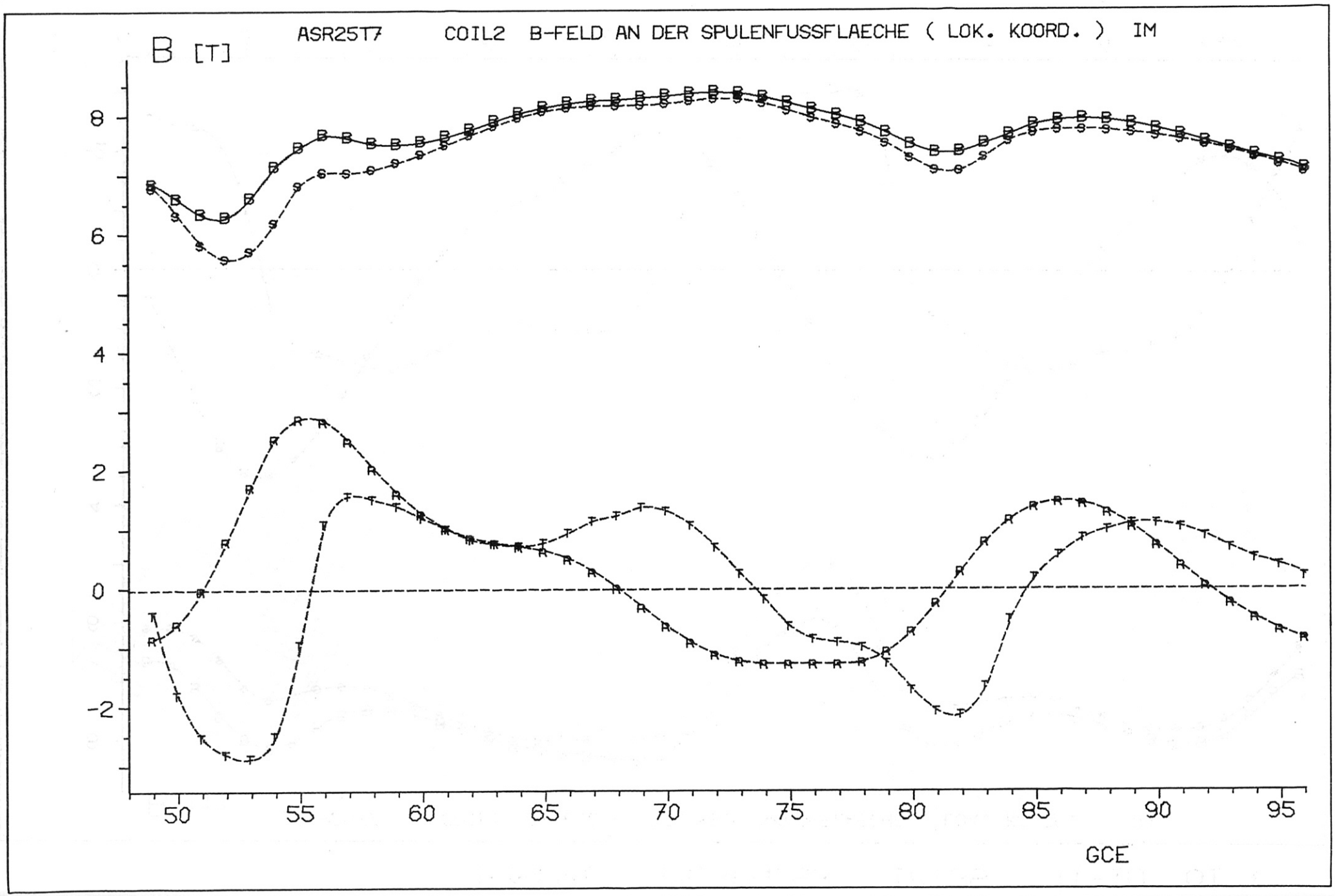

Fig. 26: Magnetic flux density at the inner side of coil 2

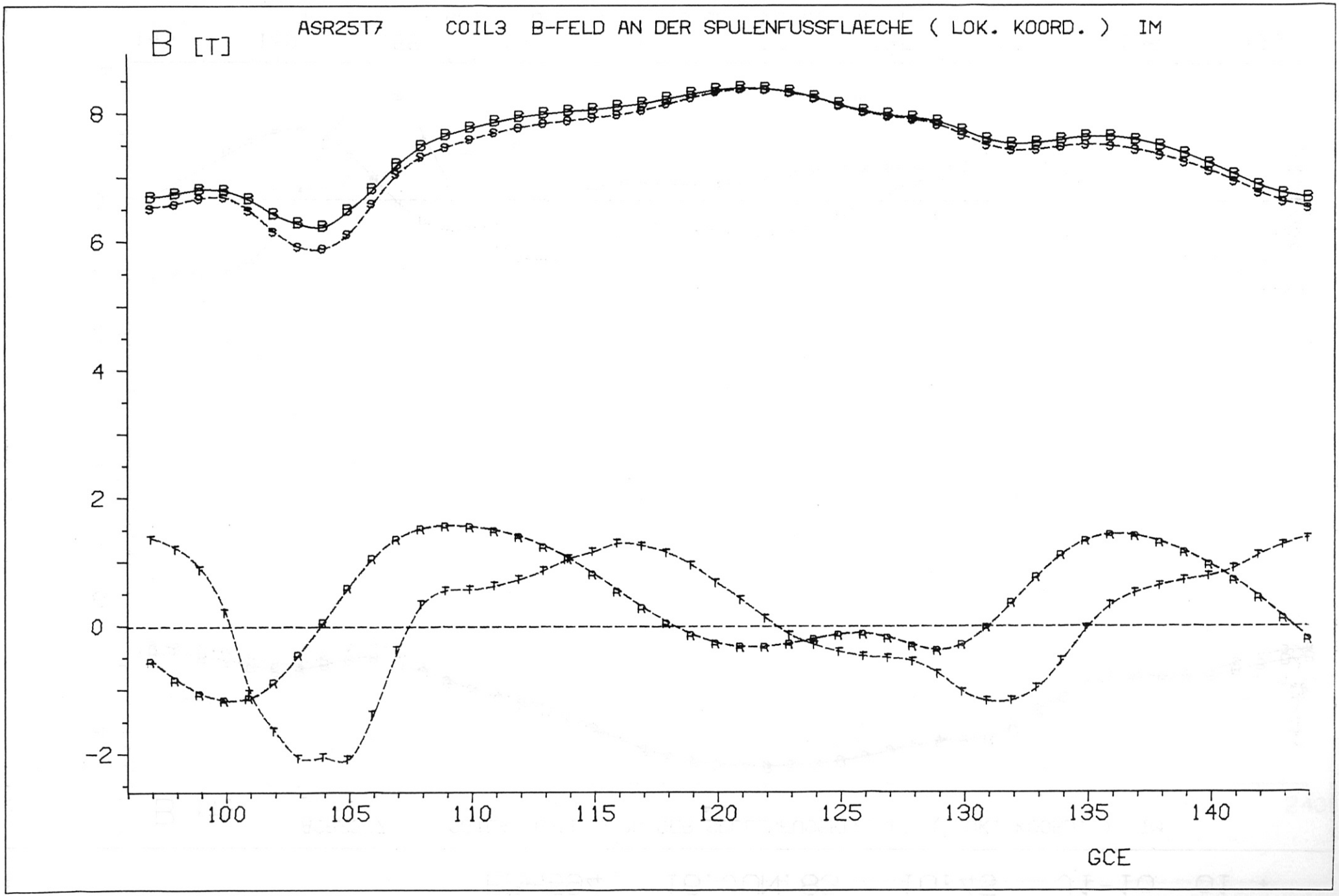

Fig. 27: Magnetic flux density at the inner side of coil 3

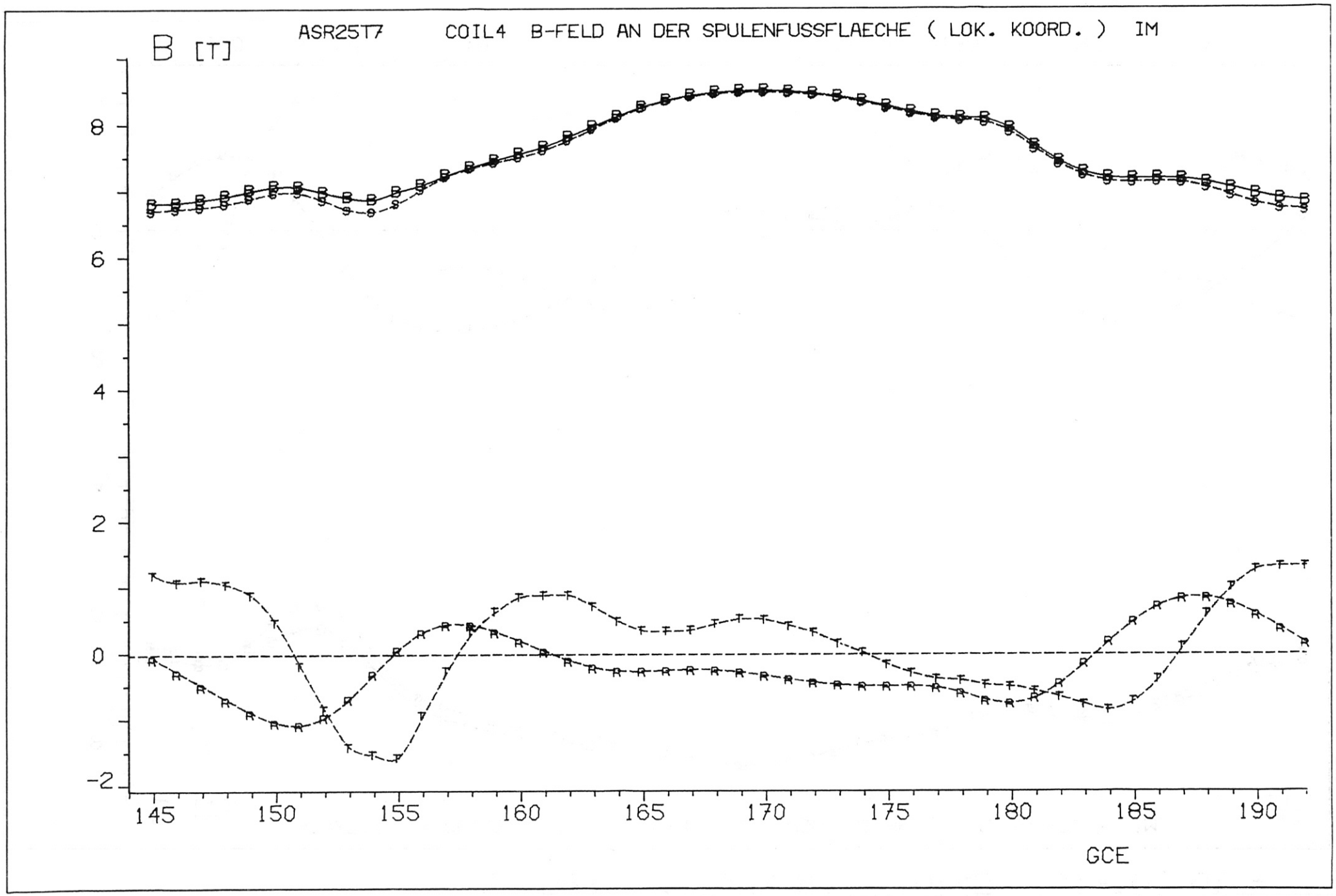

Fig. 28: Magnetic flux density at the inner side of coil 4

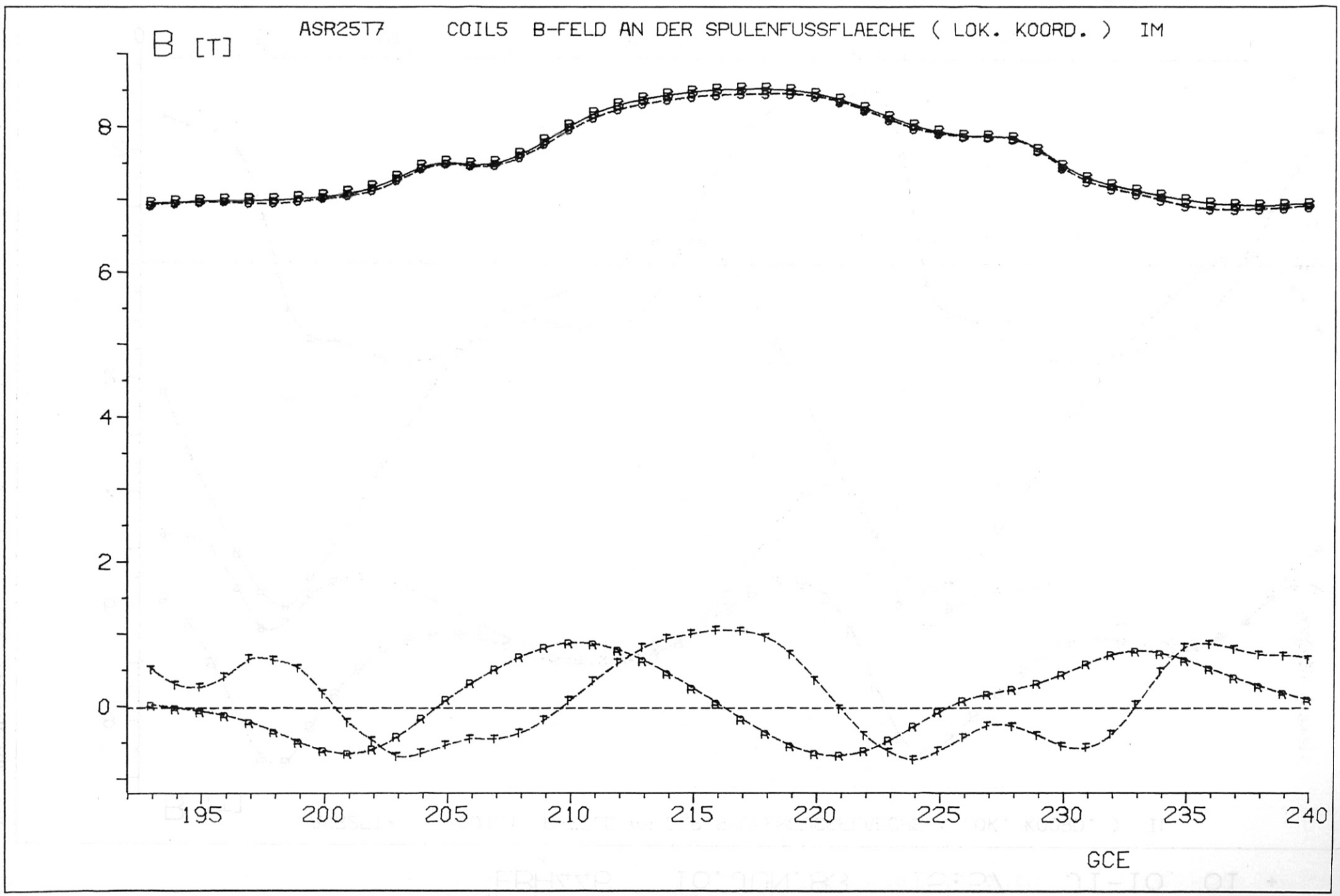

Fig. 29: Magnetic flux density at the inner side of coil 5

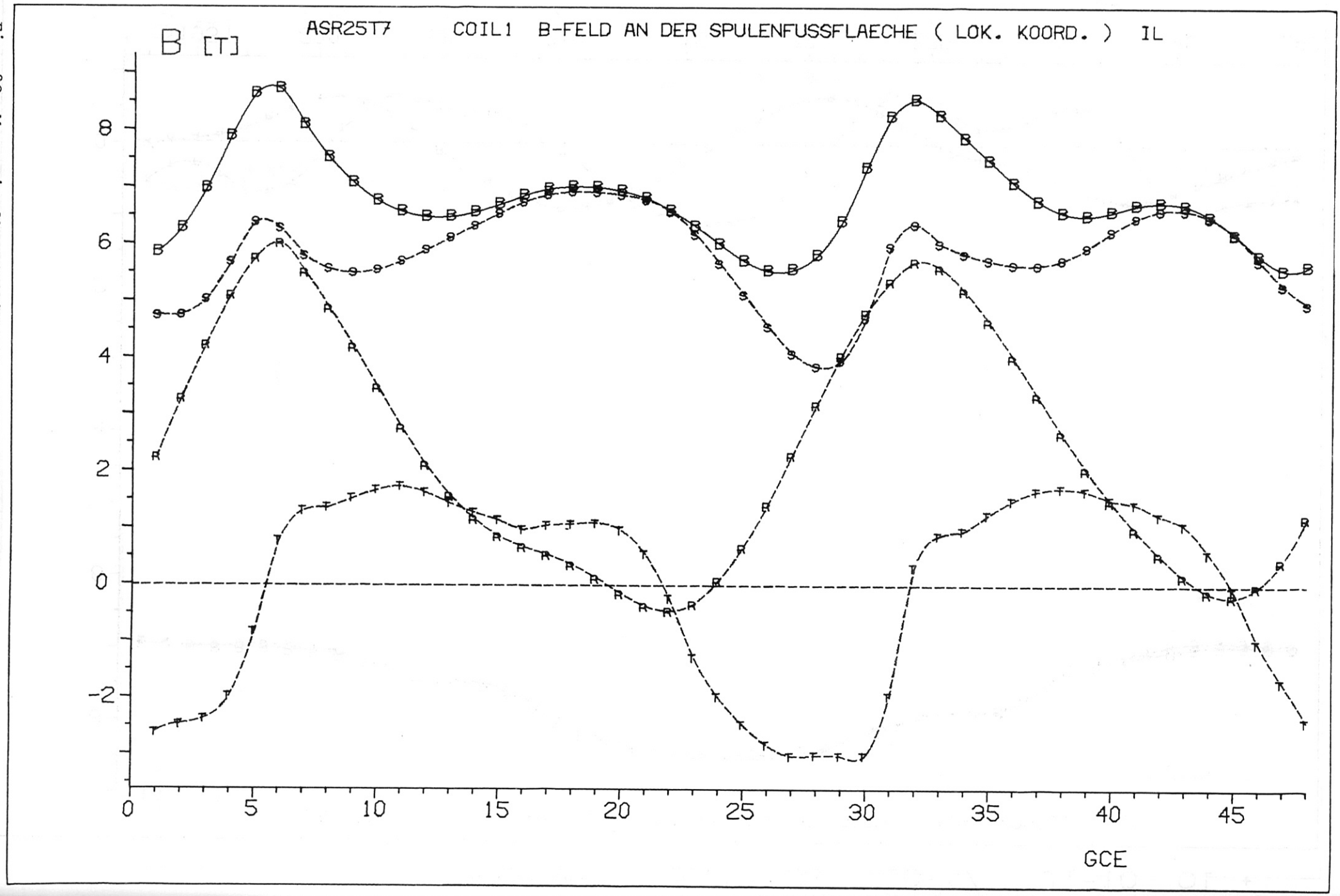

Fig. 30: Magnetic flux density of coil 1 along an edge contour of the inner side of the coil

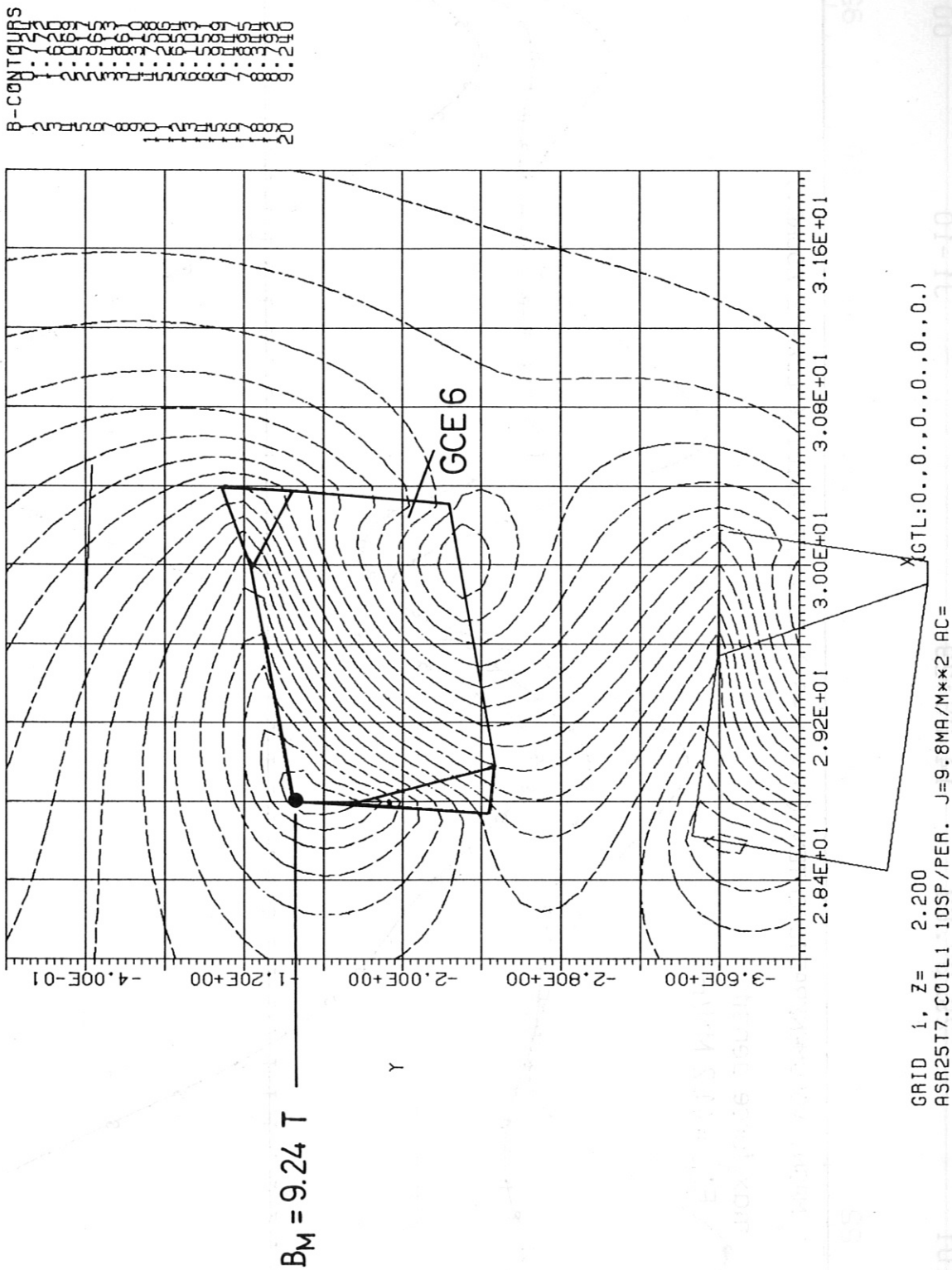

Fig. 31: Contours of constant magnetic flux density at GCE 6 of coil 1

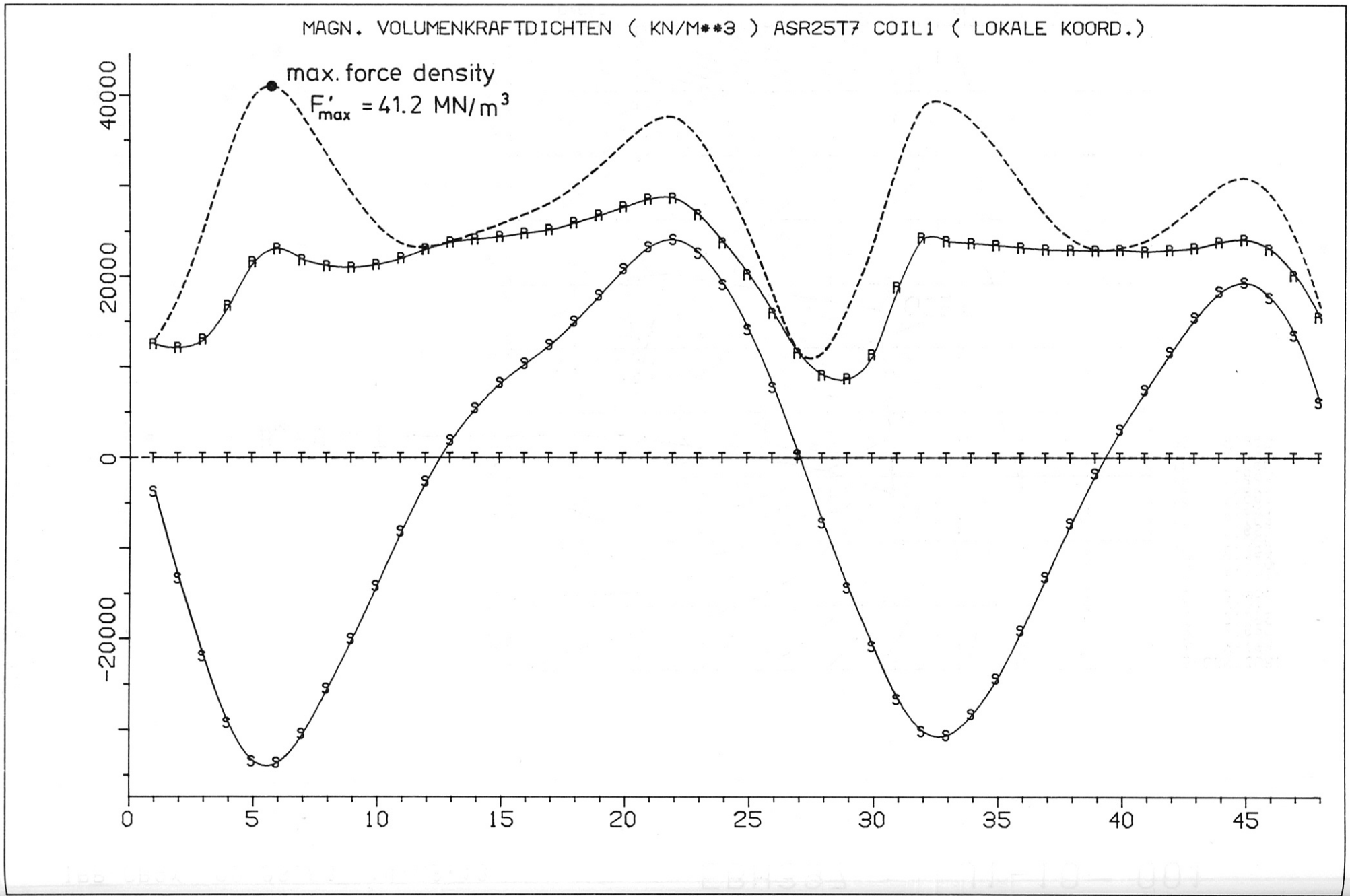

Fig. 32: Magnetic force density along "macroelements" of coil 1

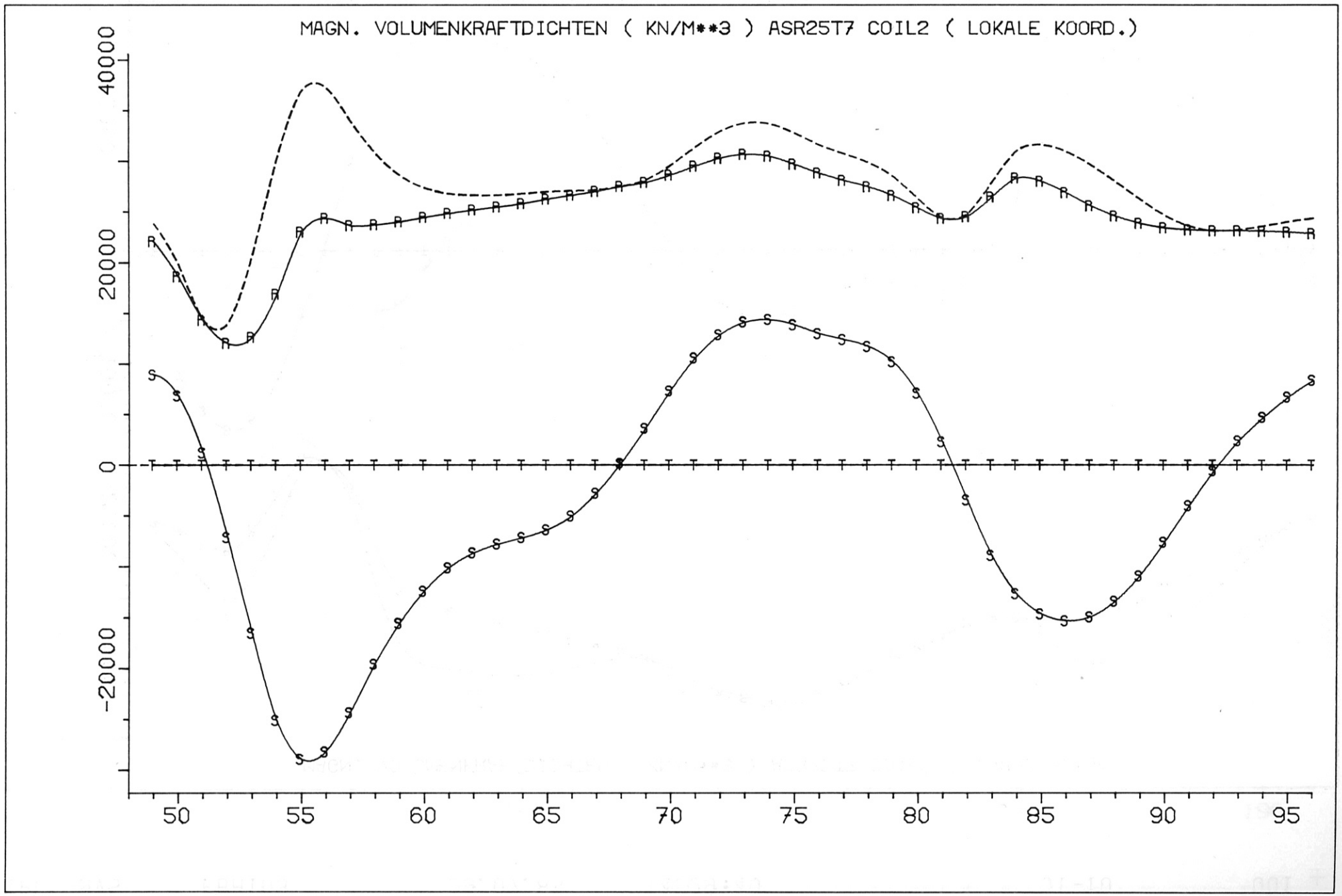

Fig. 33: Magnetic force density along "macroelements" of coil 2

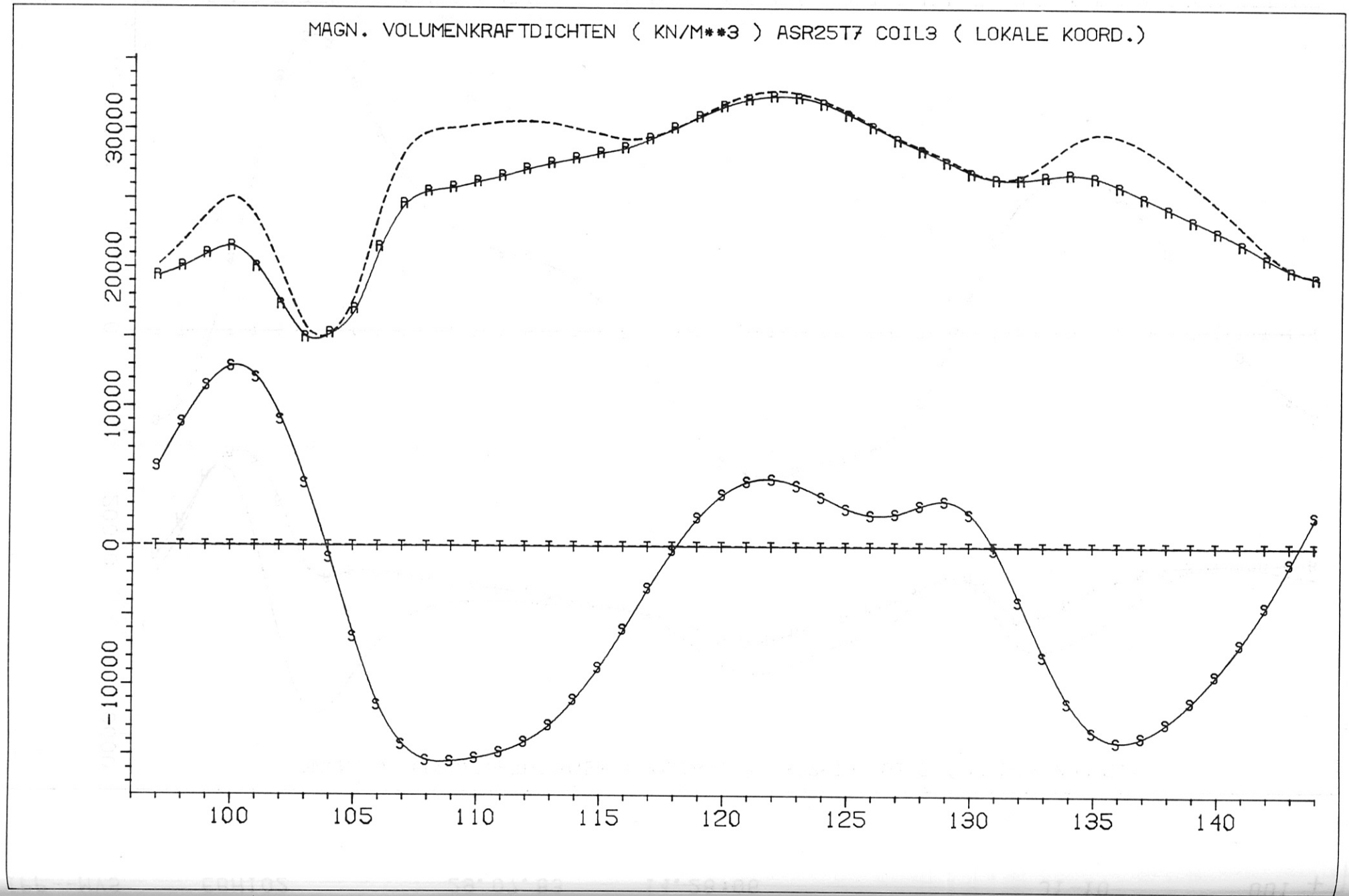

Fig. 34: Magnetic force density along "macroelements" of coil 3

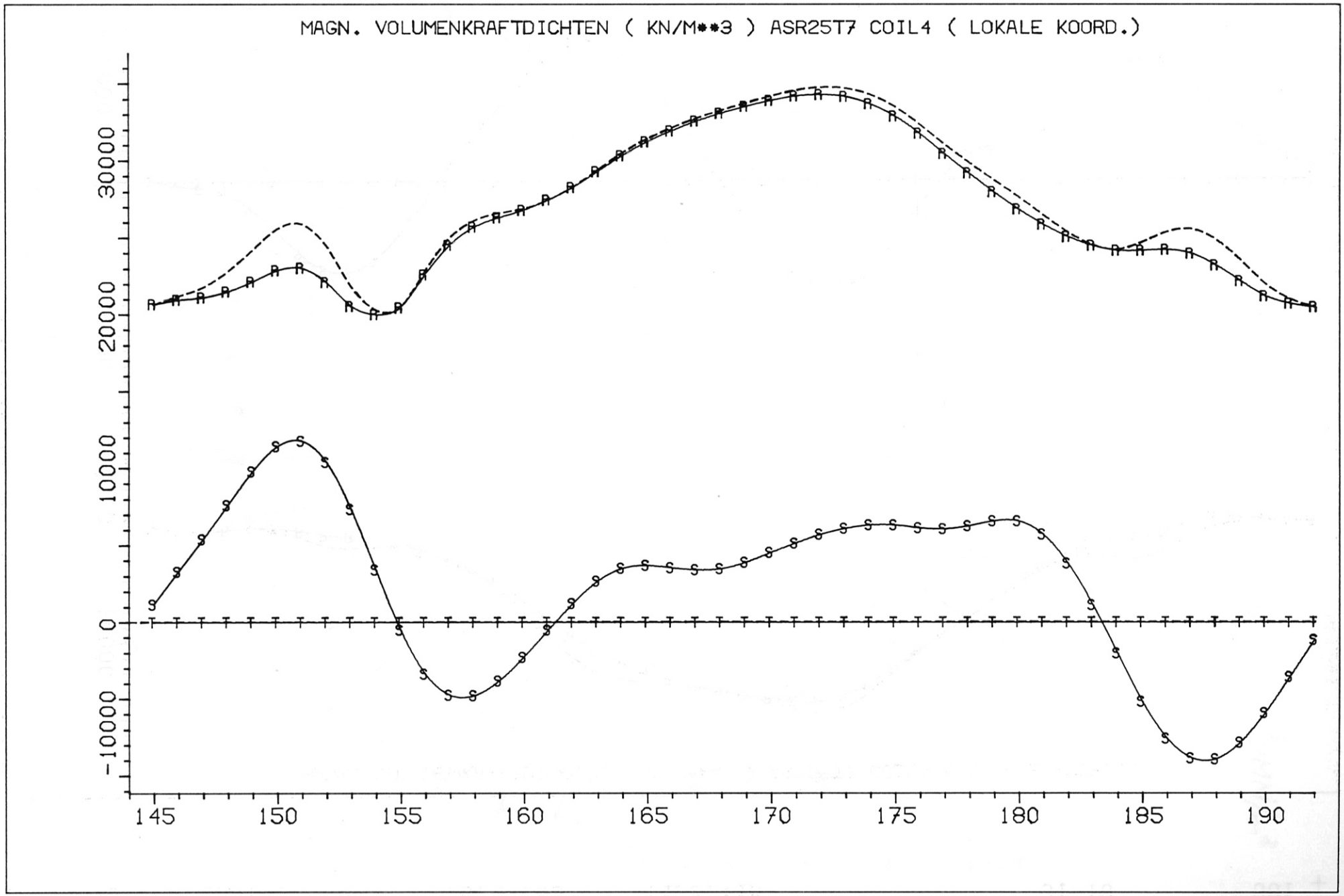

Fig. 35: Magnetic force density along "macroelelements" of coil 4

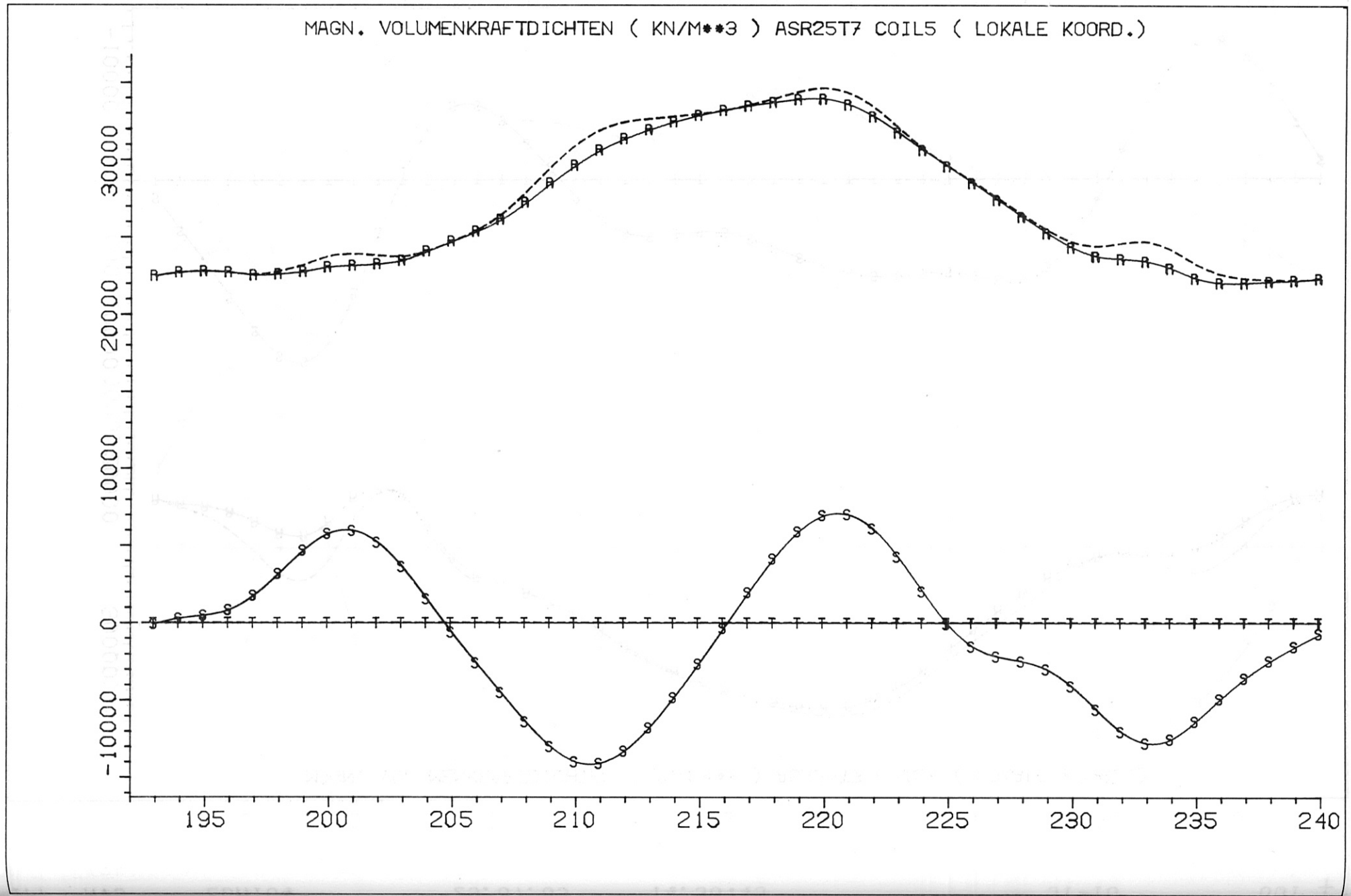

Fig. 36: Magnetic force density along "macroelements" of coil 5

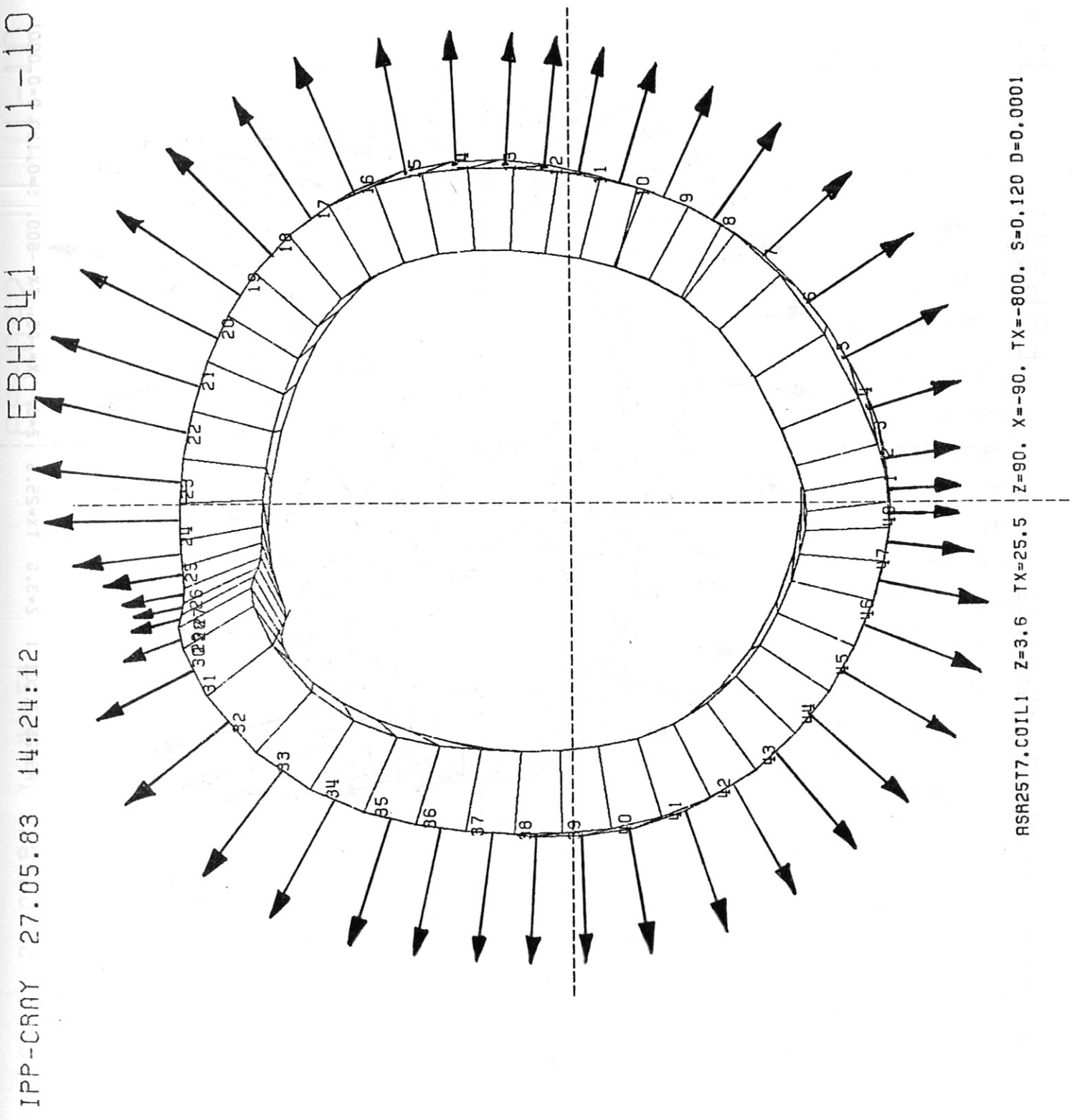

Fig. 37: Radial magnetic force density coil 1

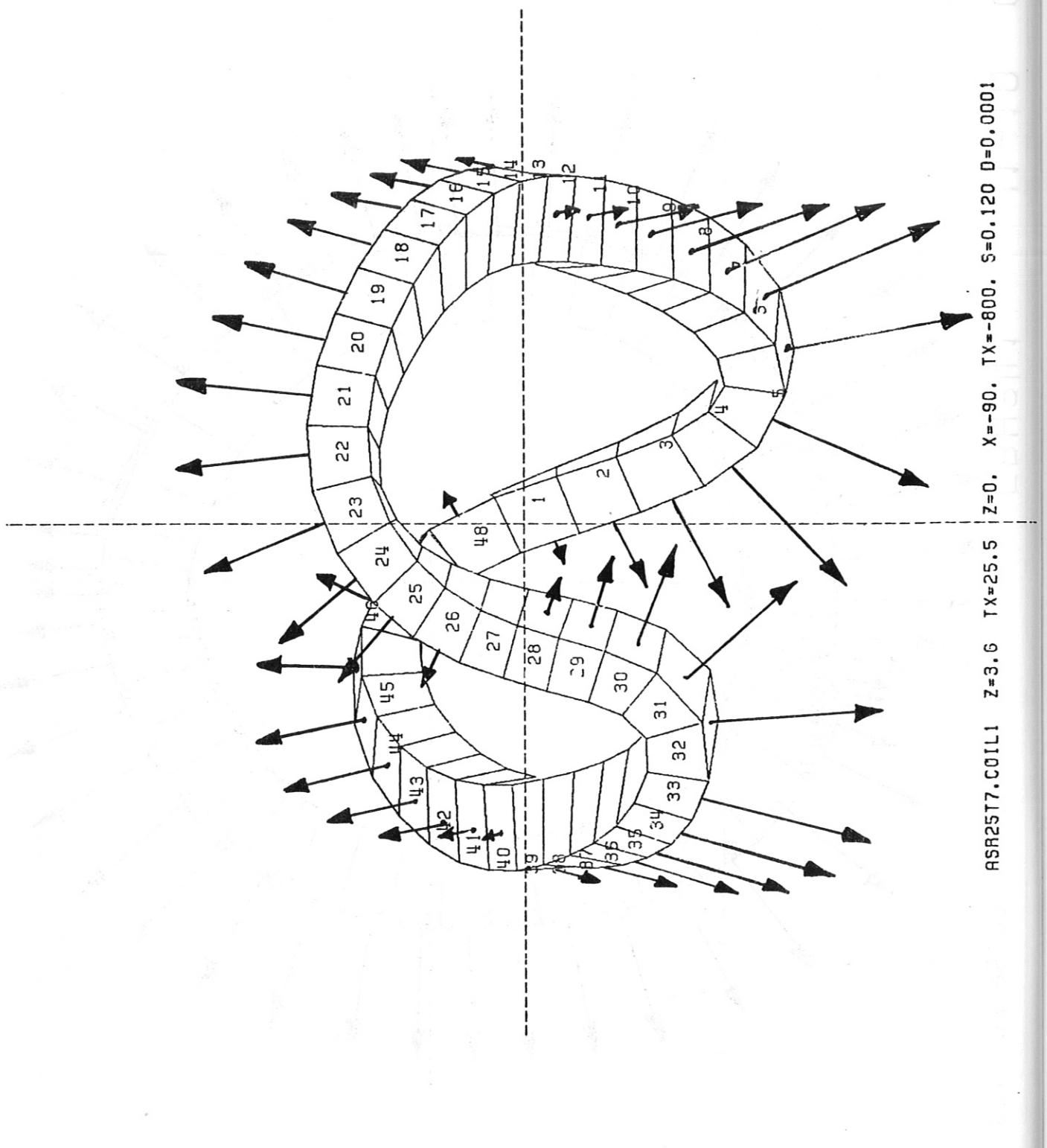

Fig. 38: Lateral magnetic force density coil 1

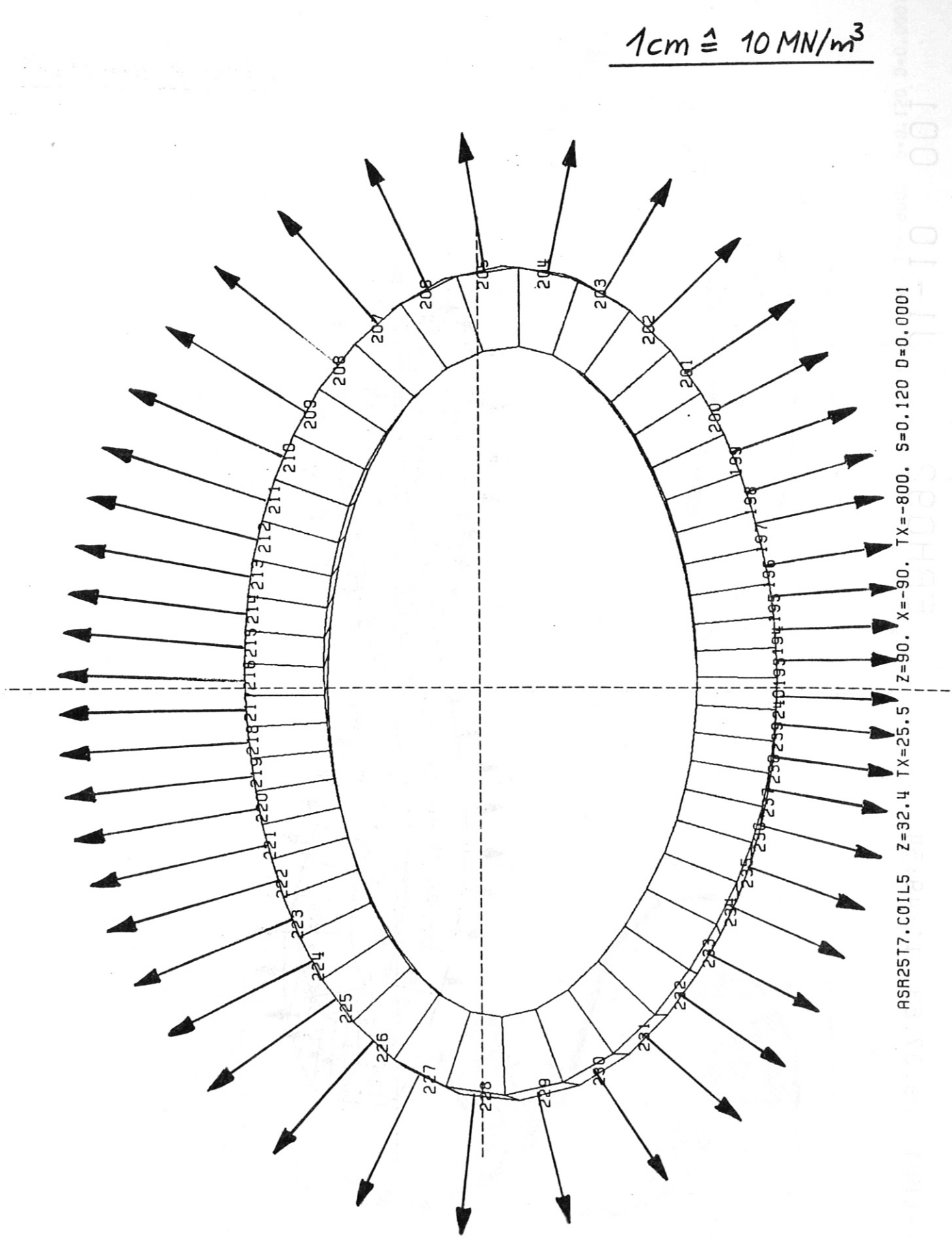

Fig. 39: Radial magnetic force density coil 5

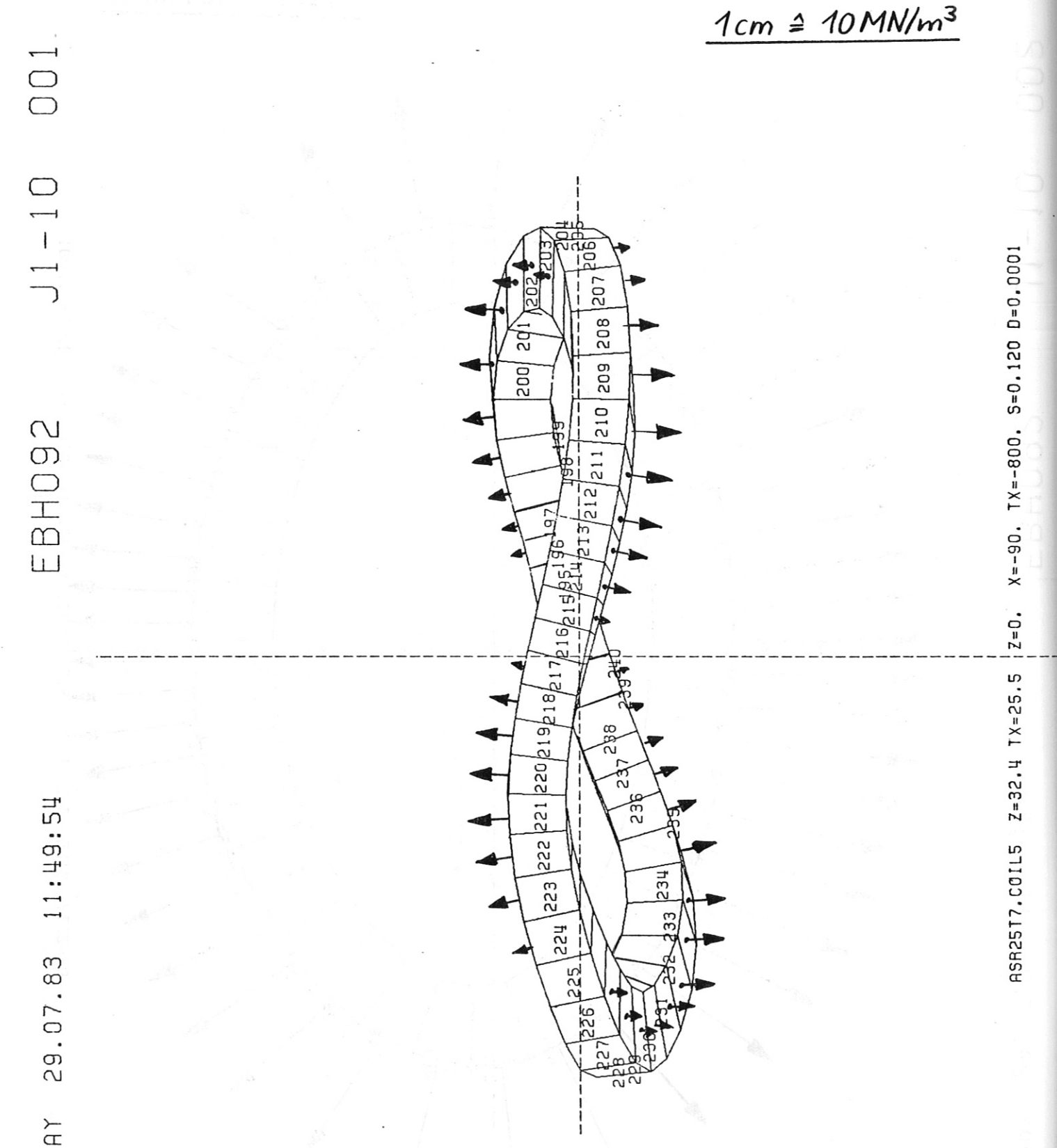

Fig. 40: Lateral magnetic force density coil 5

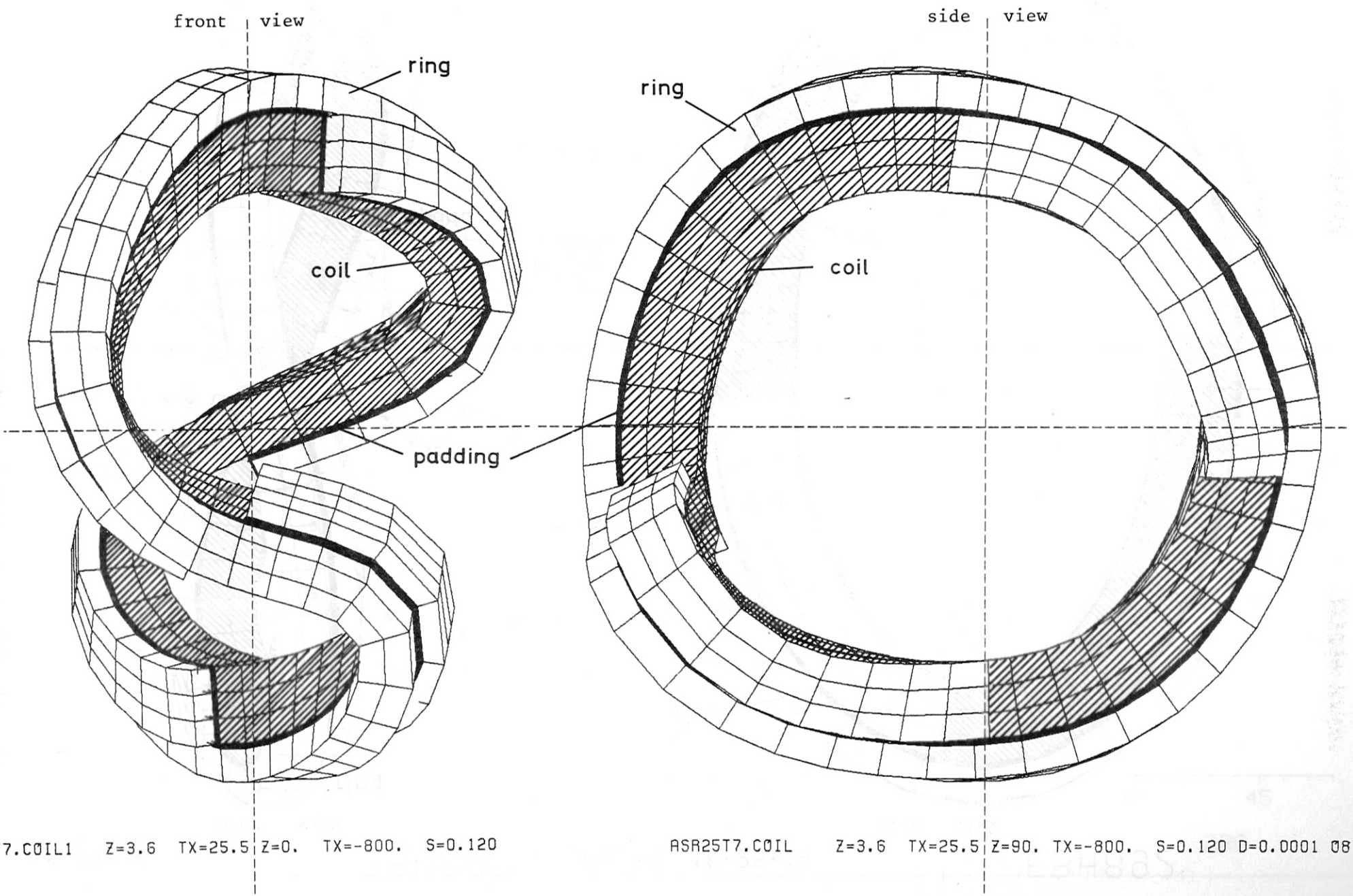

Fig. 41: Coil 1 with support structure

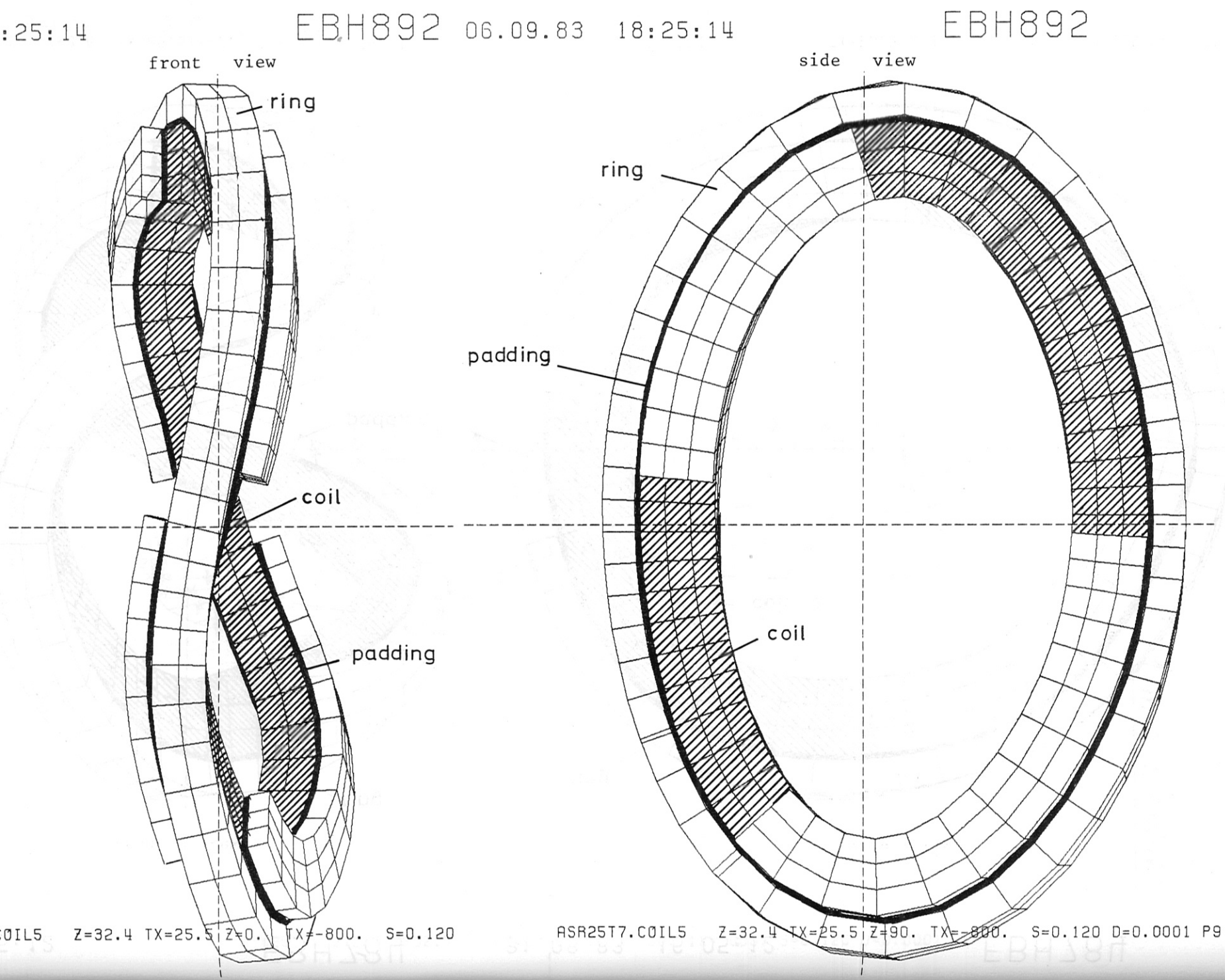

Fig. 42: Coil 5 with support structure

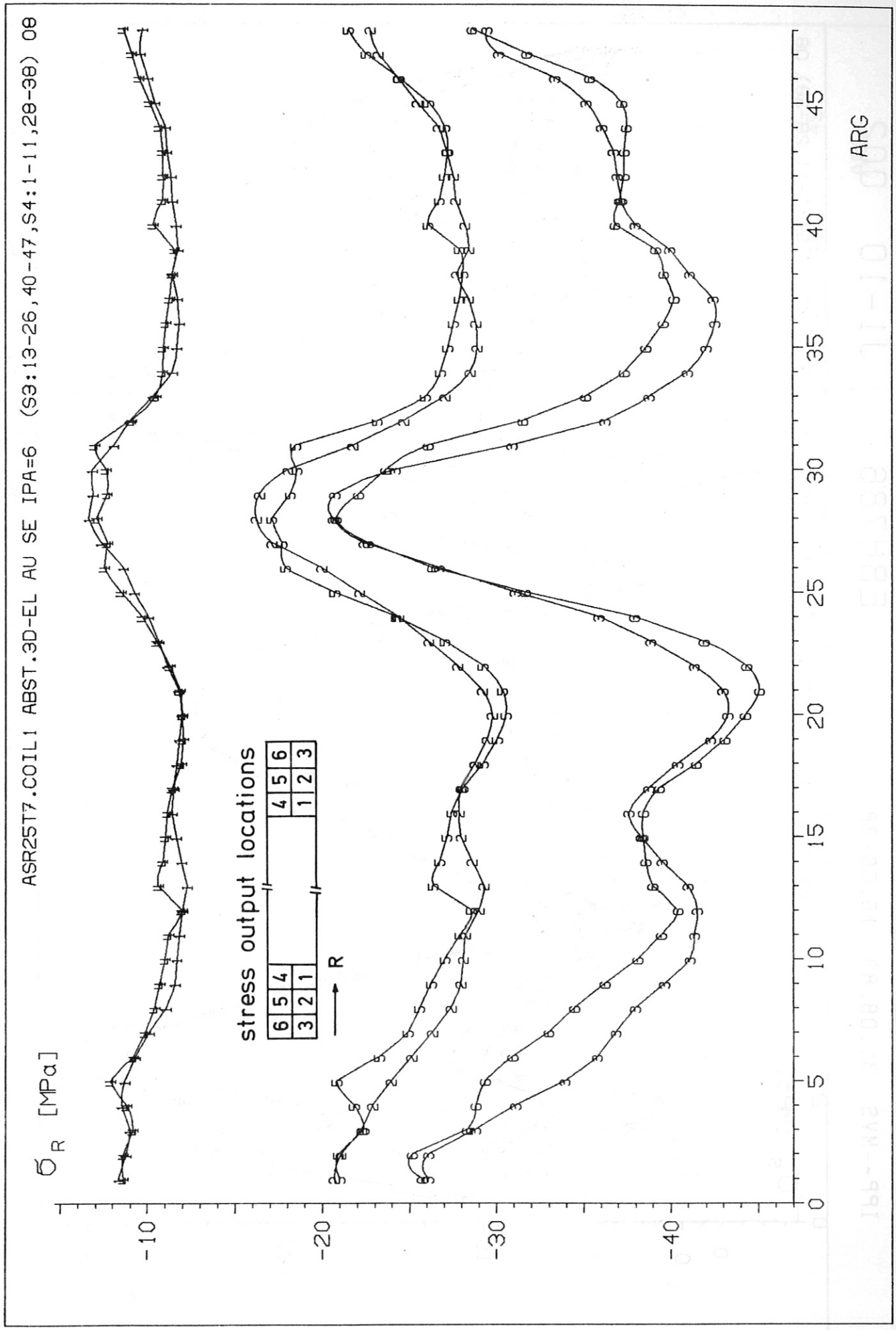

Fig. 43: Radial stress coil 1 with position of the "microelements" as in the insert

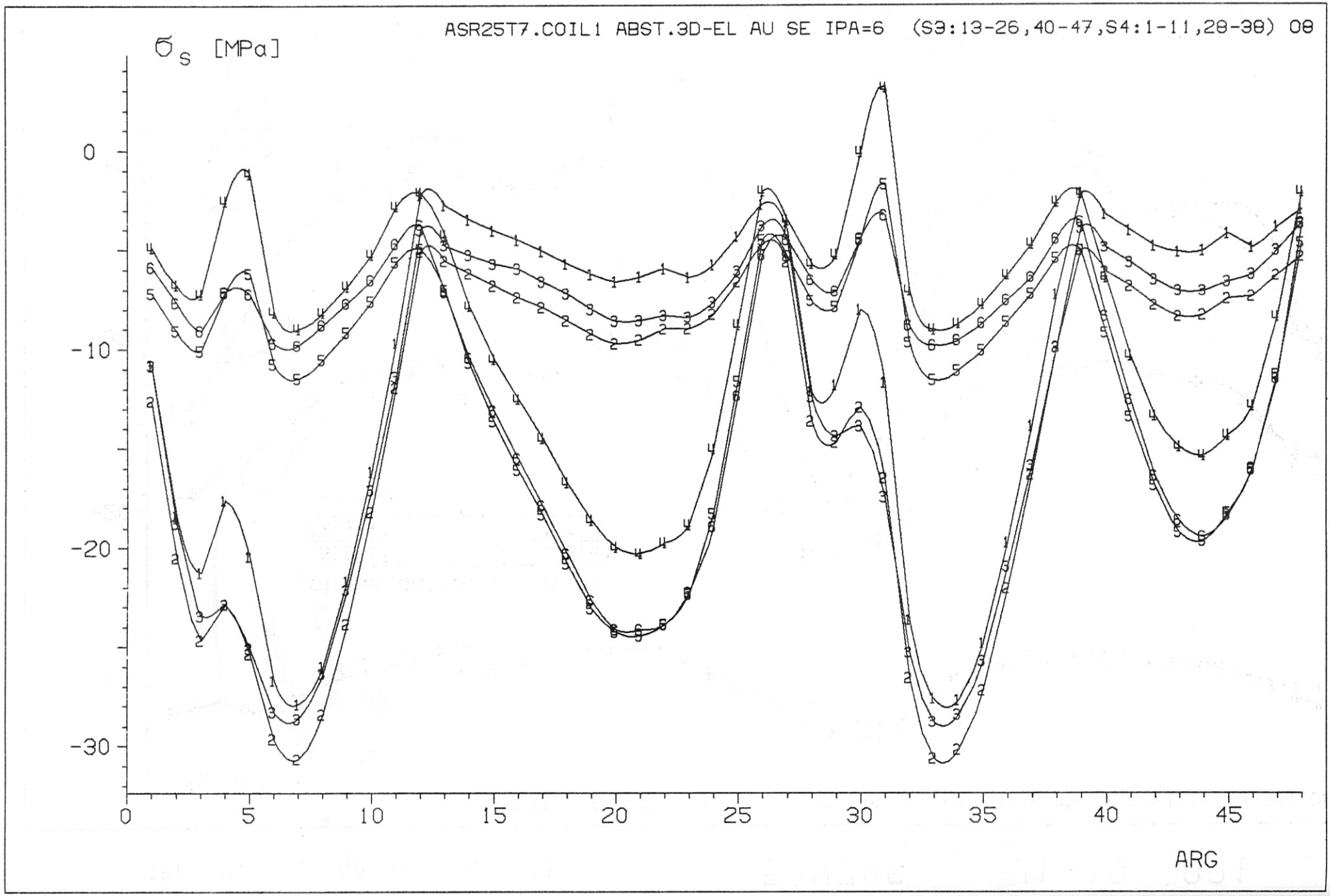

Fig. 44: Lateral stress coil 1

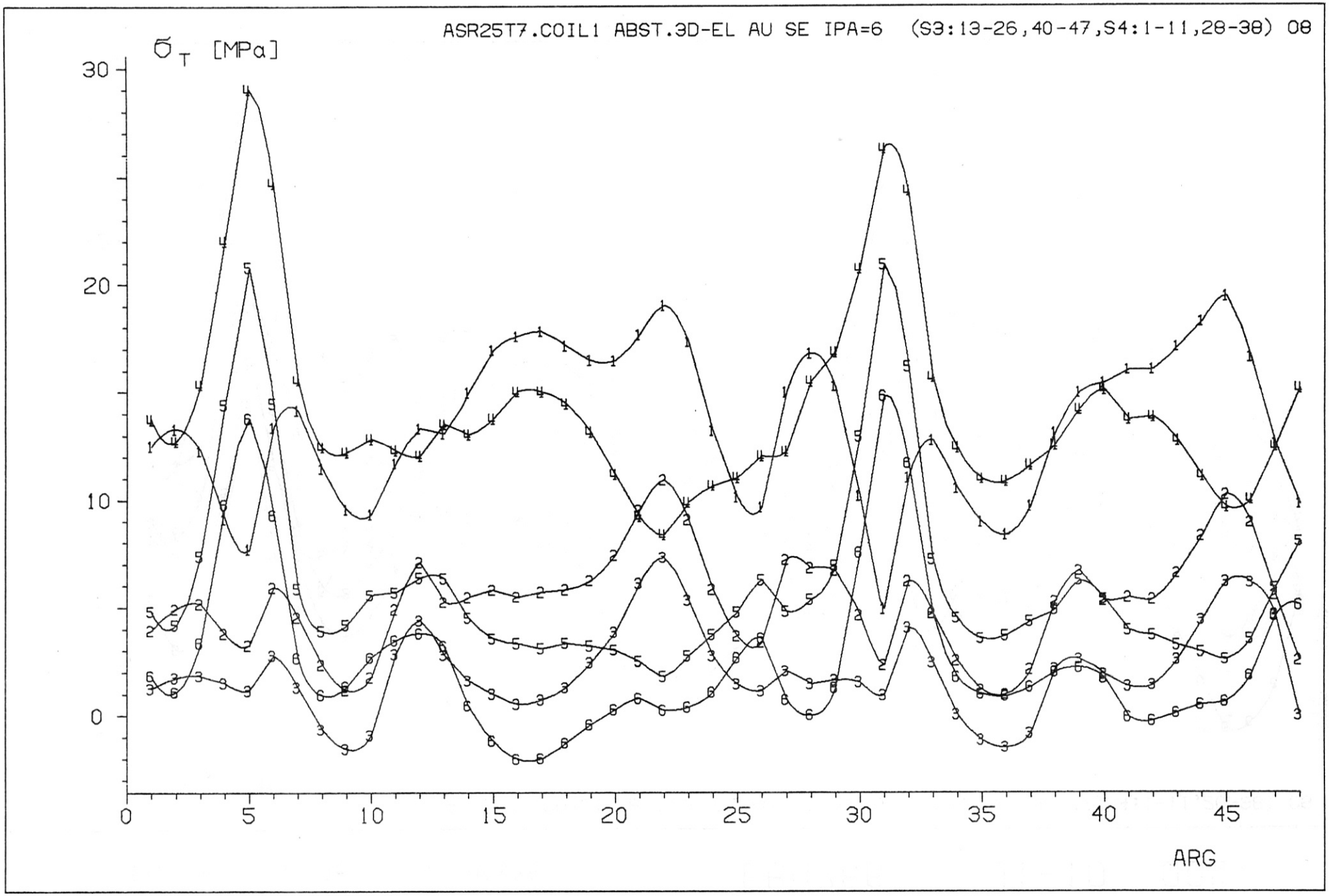

Fig. 45: Circumferential tensile stress coil 1

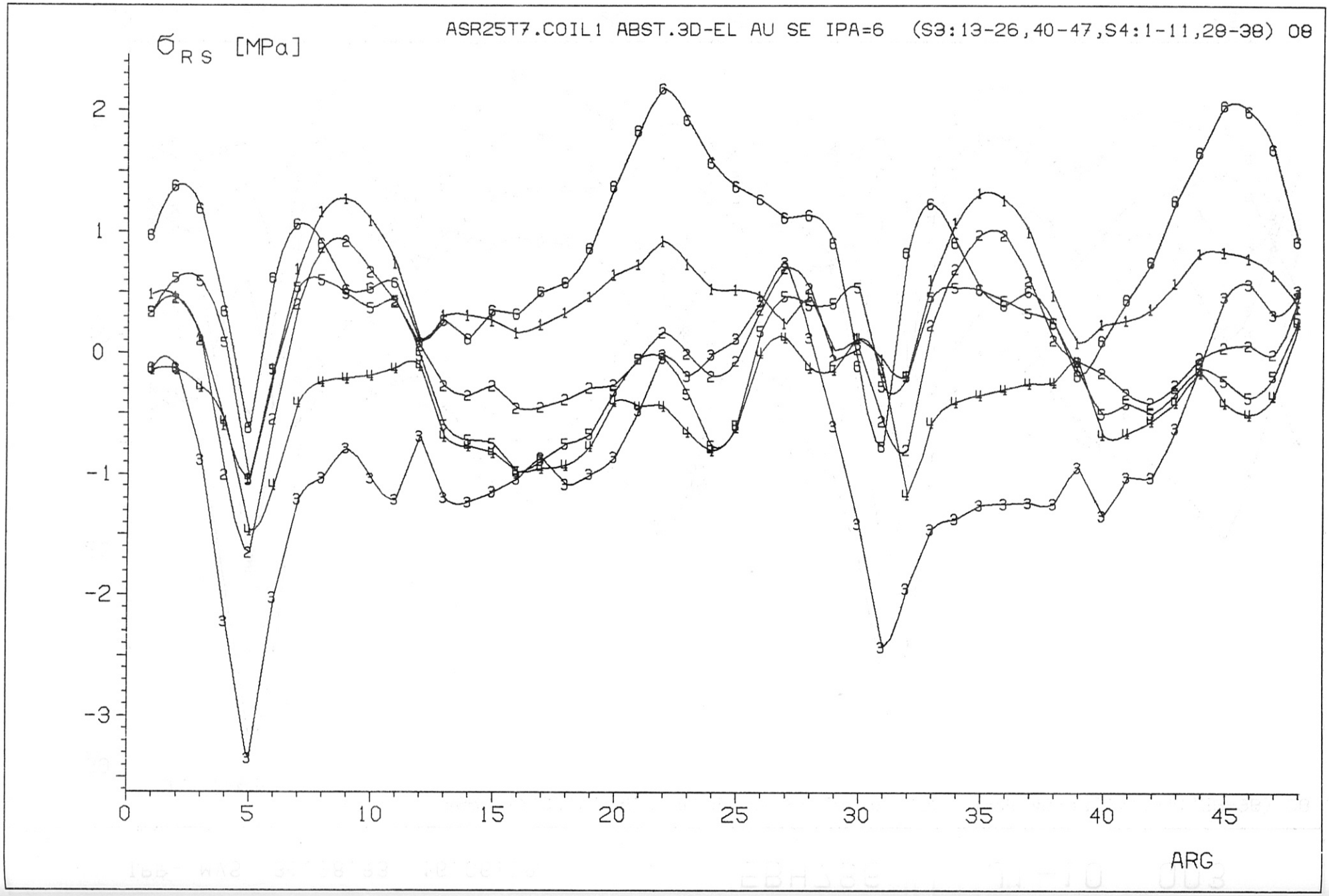

Fig. 46: Shear stress σ_{RS} coil 1

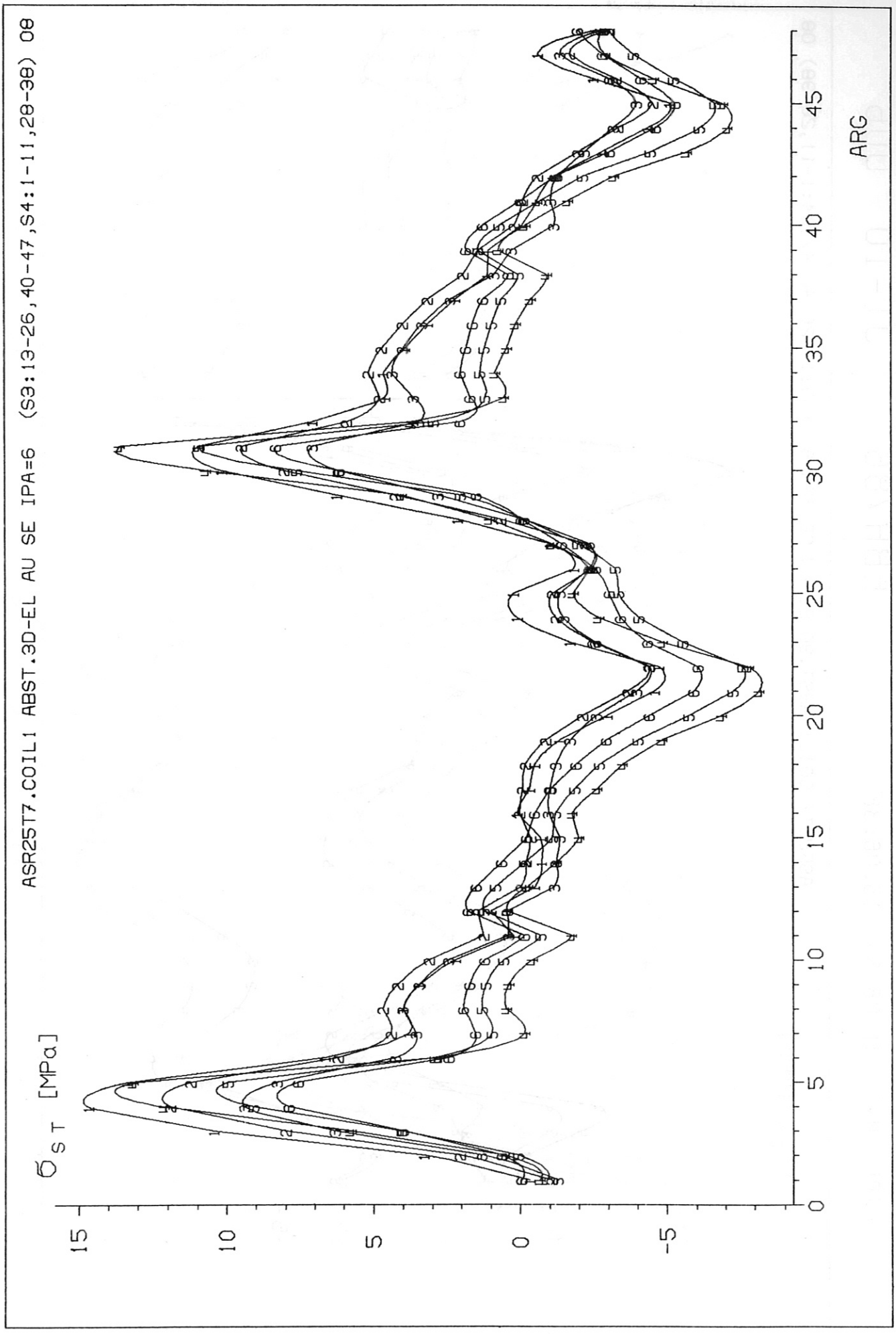

Fig. 47: Shear stress σ_{ST} coil 1

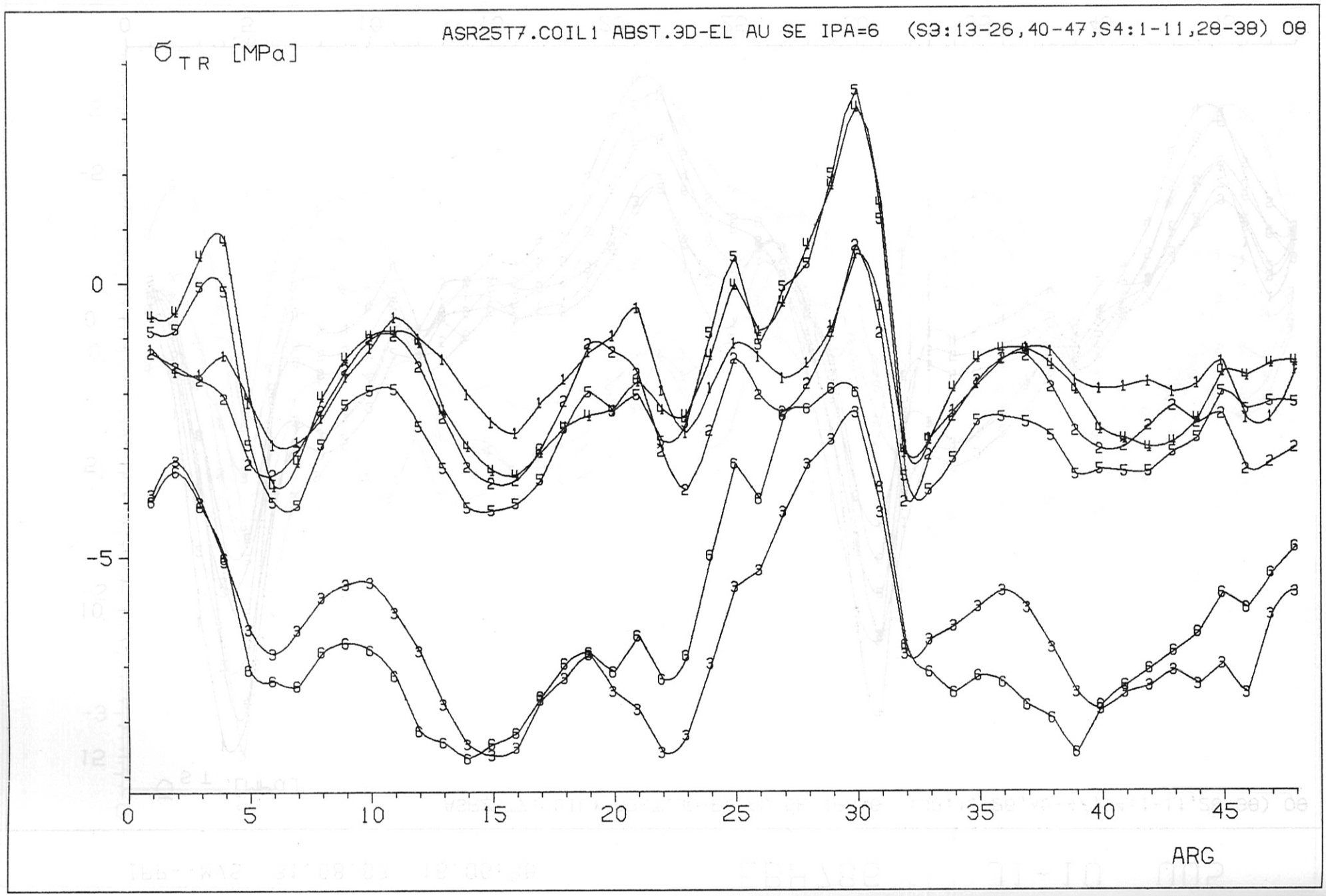

Fig. 48: Shear stress σ_{TR} coil 1

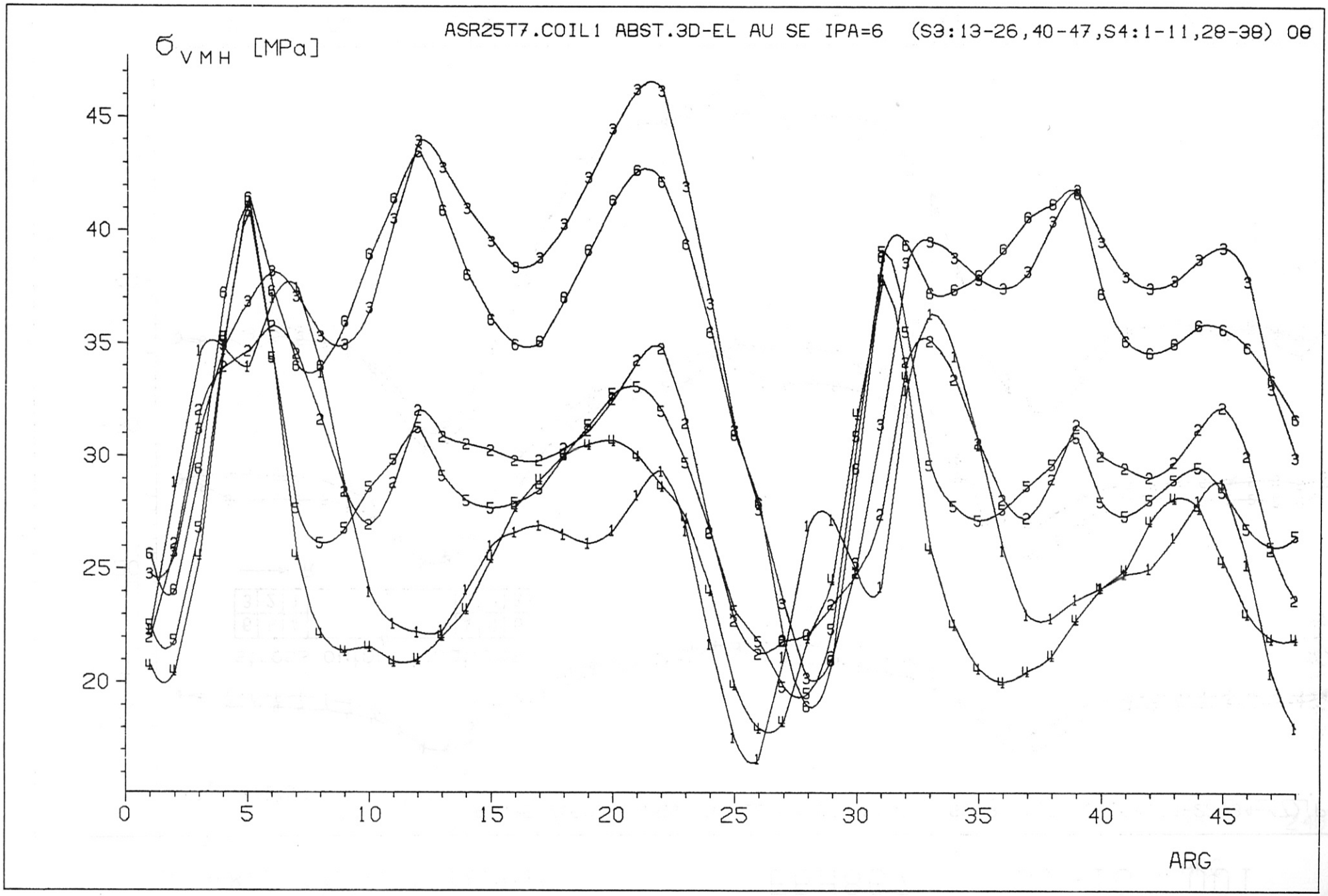

Fig. 49: Reference stress (von Mises stress) coil 1

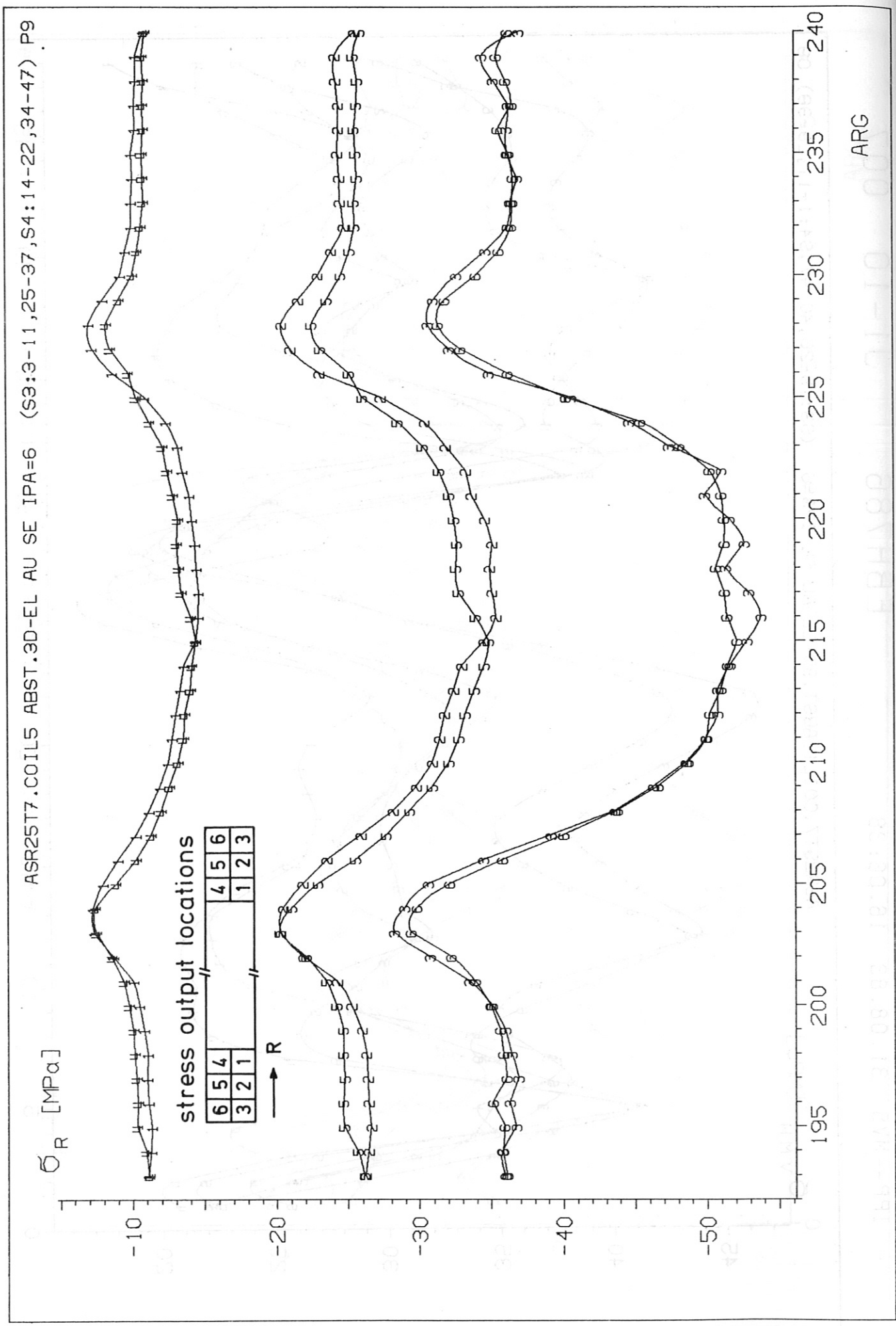

Fig. 50: Radial stress coil 5 with position of the "microelements" as in the insert

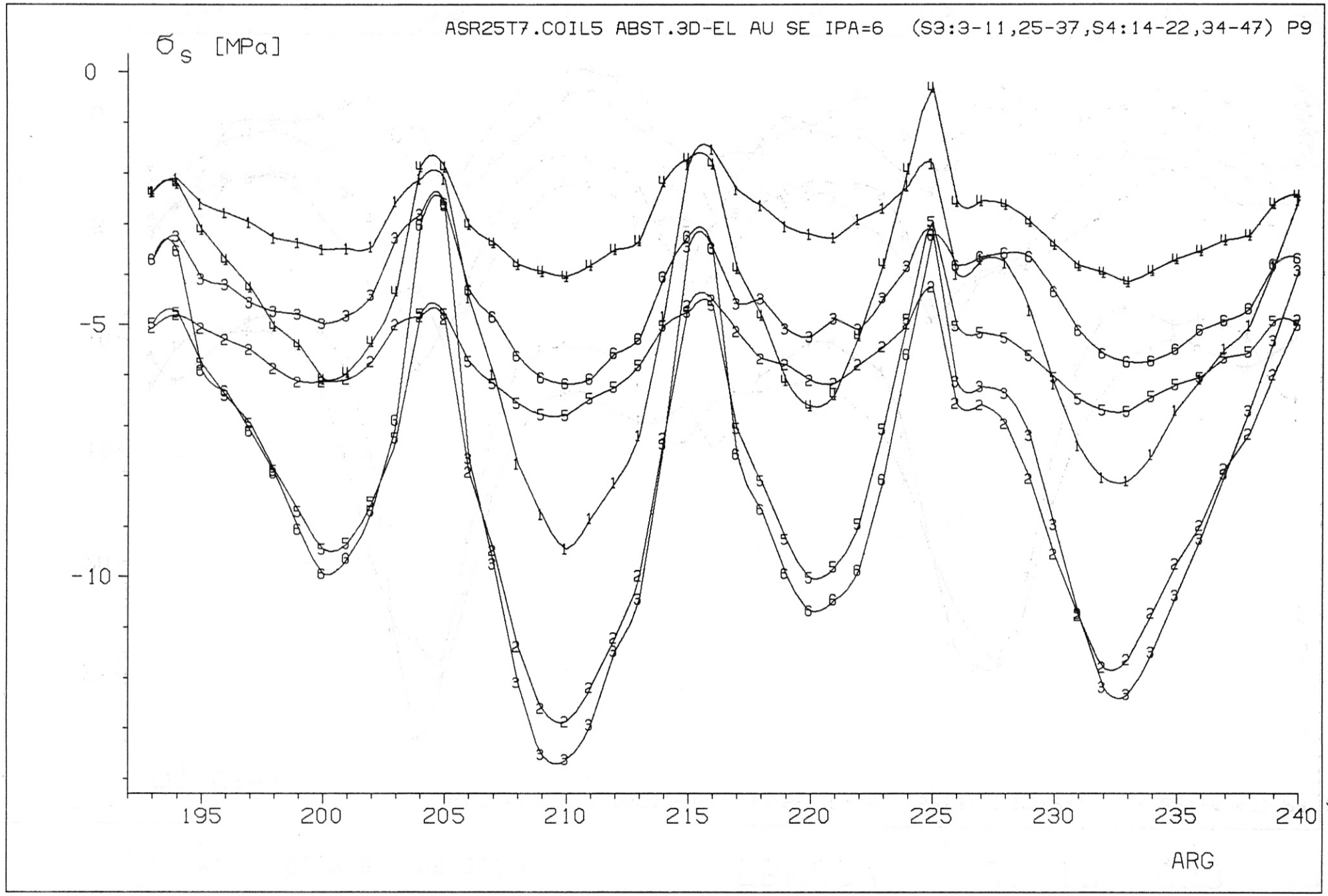

Fig. 51: Lateral stress coil 5

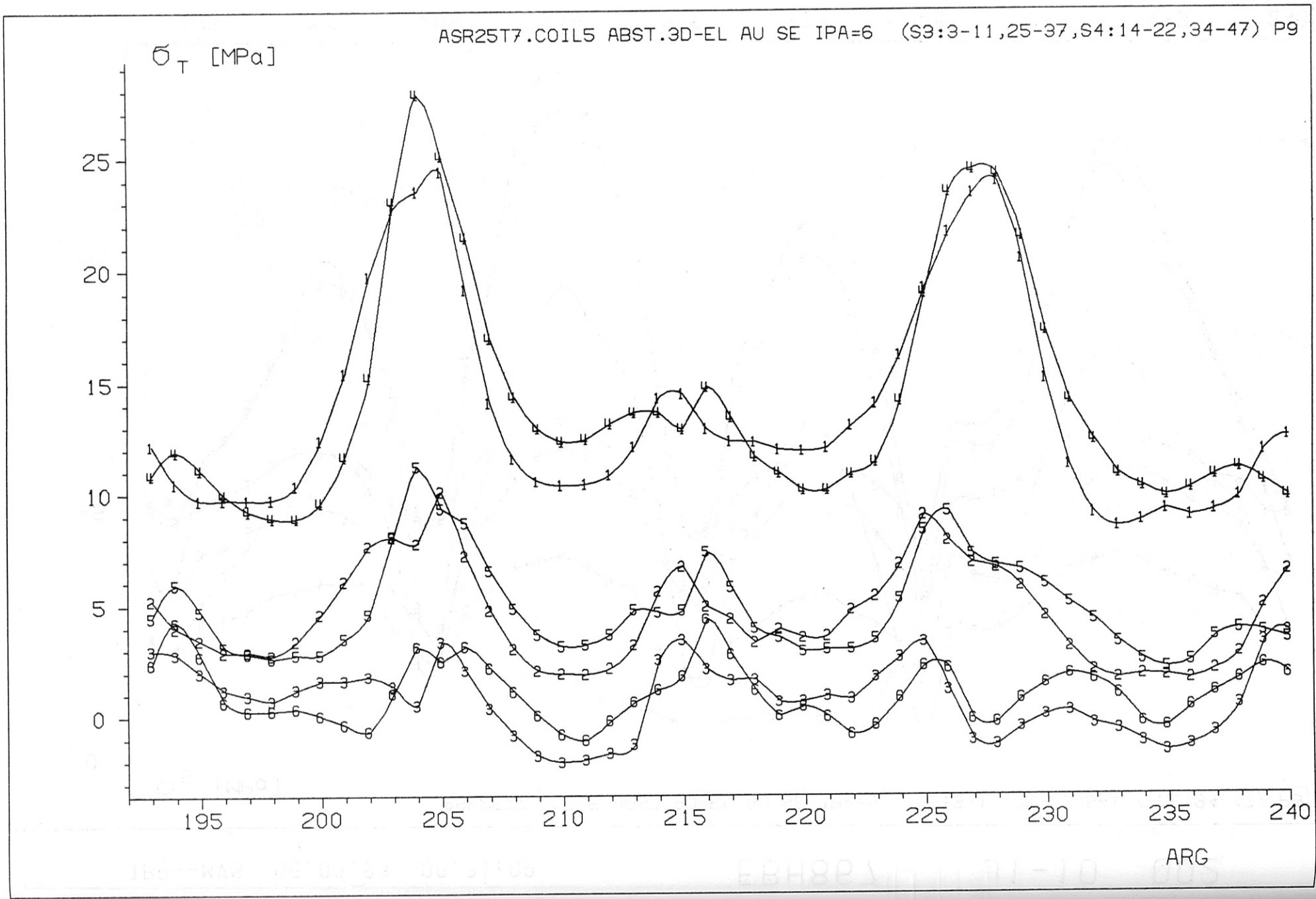

Fig. 52: Circumferential tensile stress coil 5

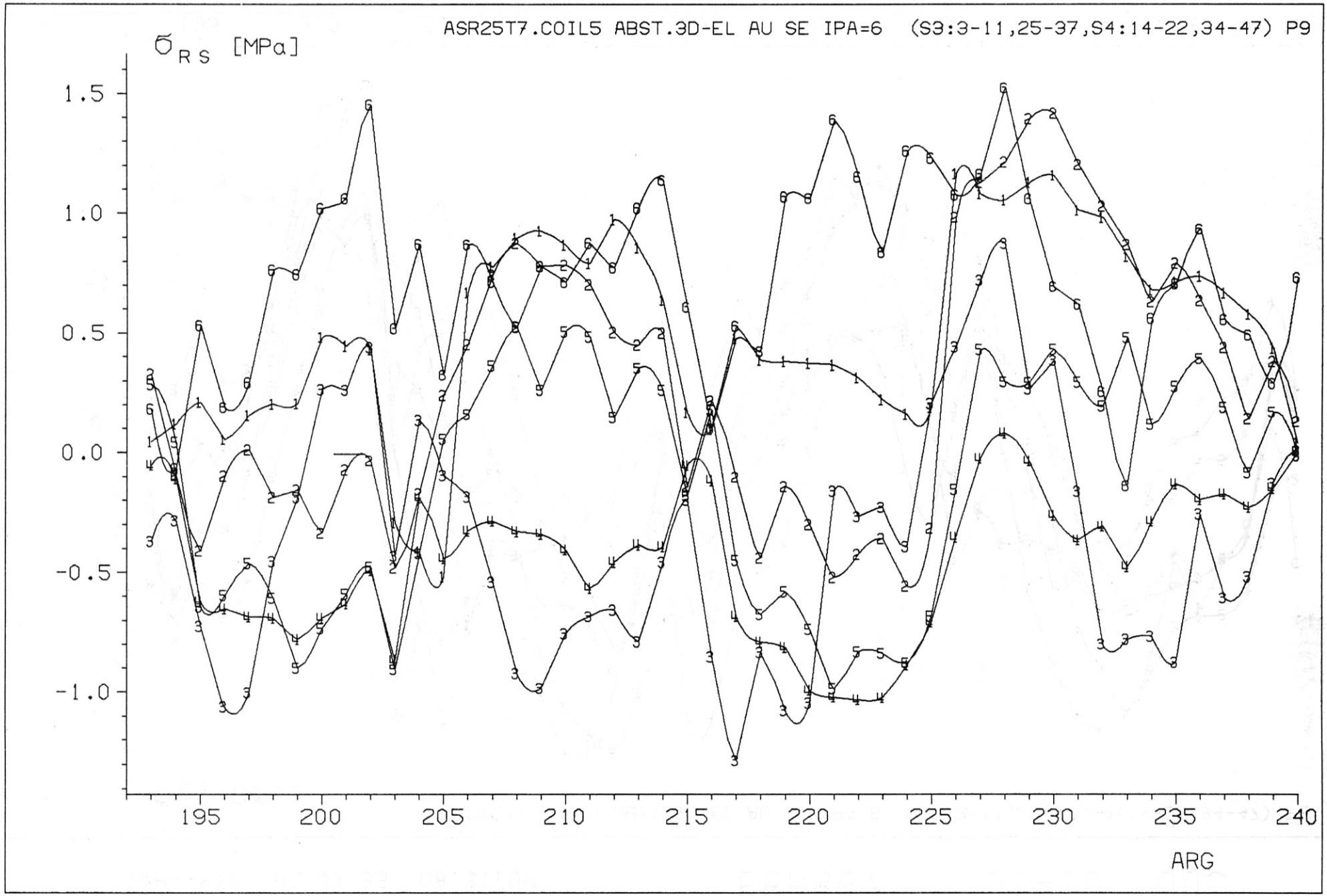

Fig. 53: Shear stress σ_{RS} coil 5

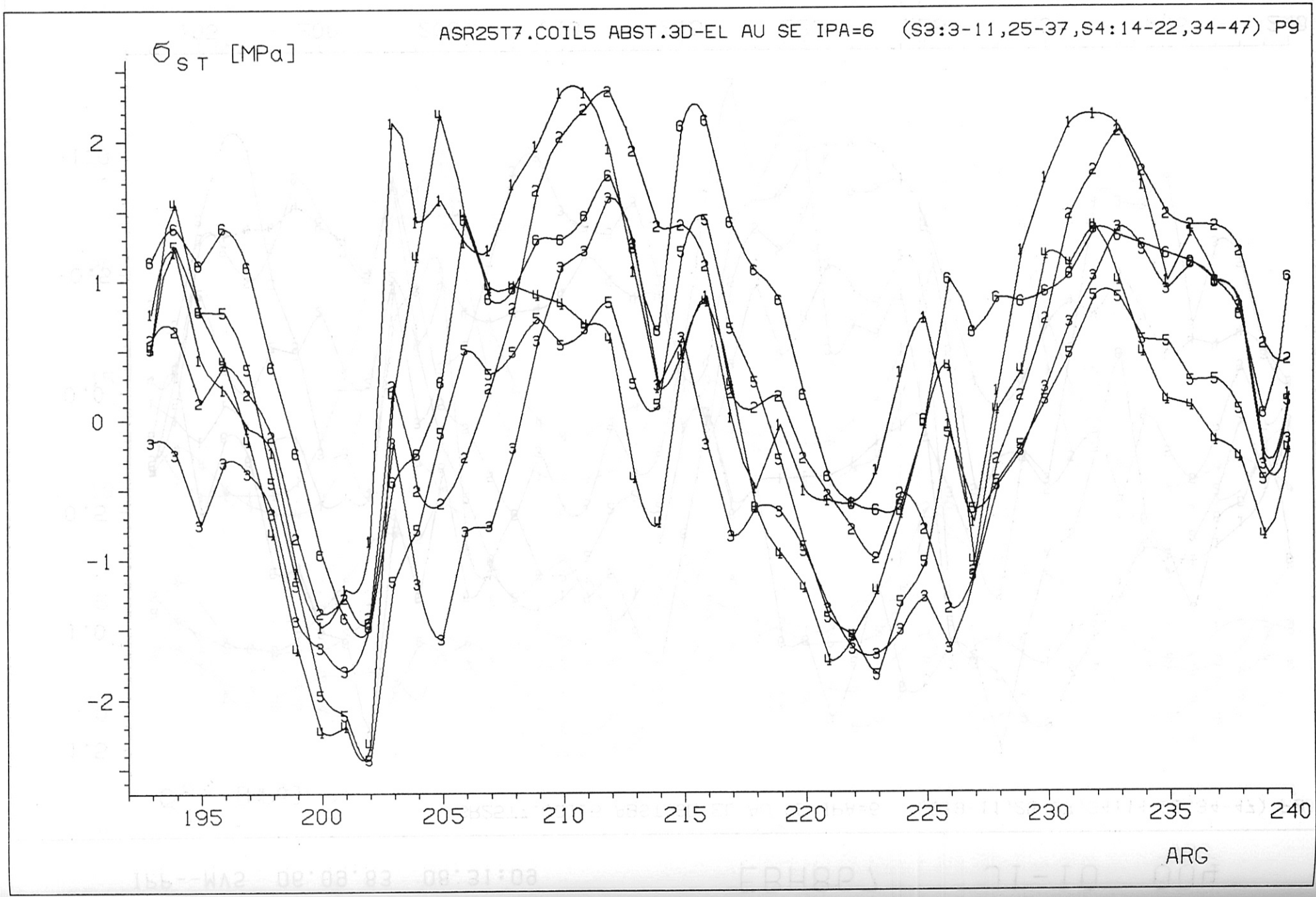

Fig. 54: Shear stress σ_{ST} coil 5

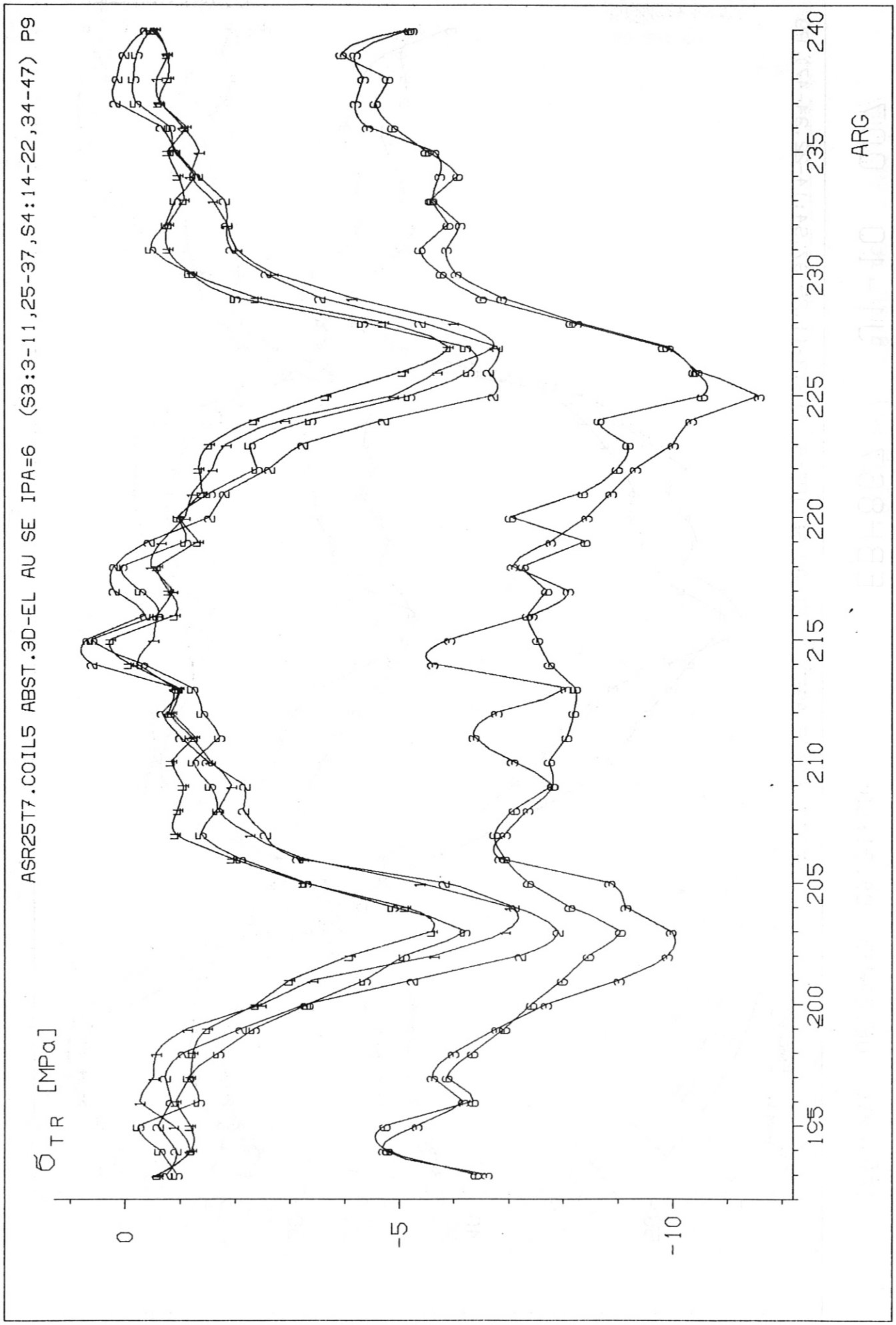

Fig. 55: Shear stress σ_{TR} coil 5

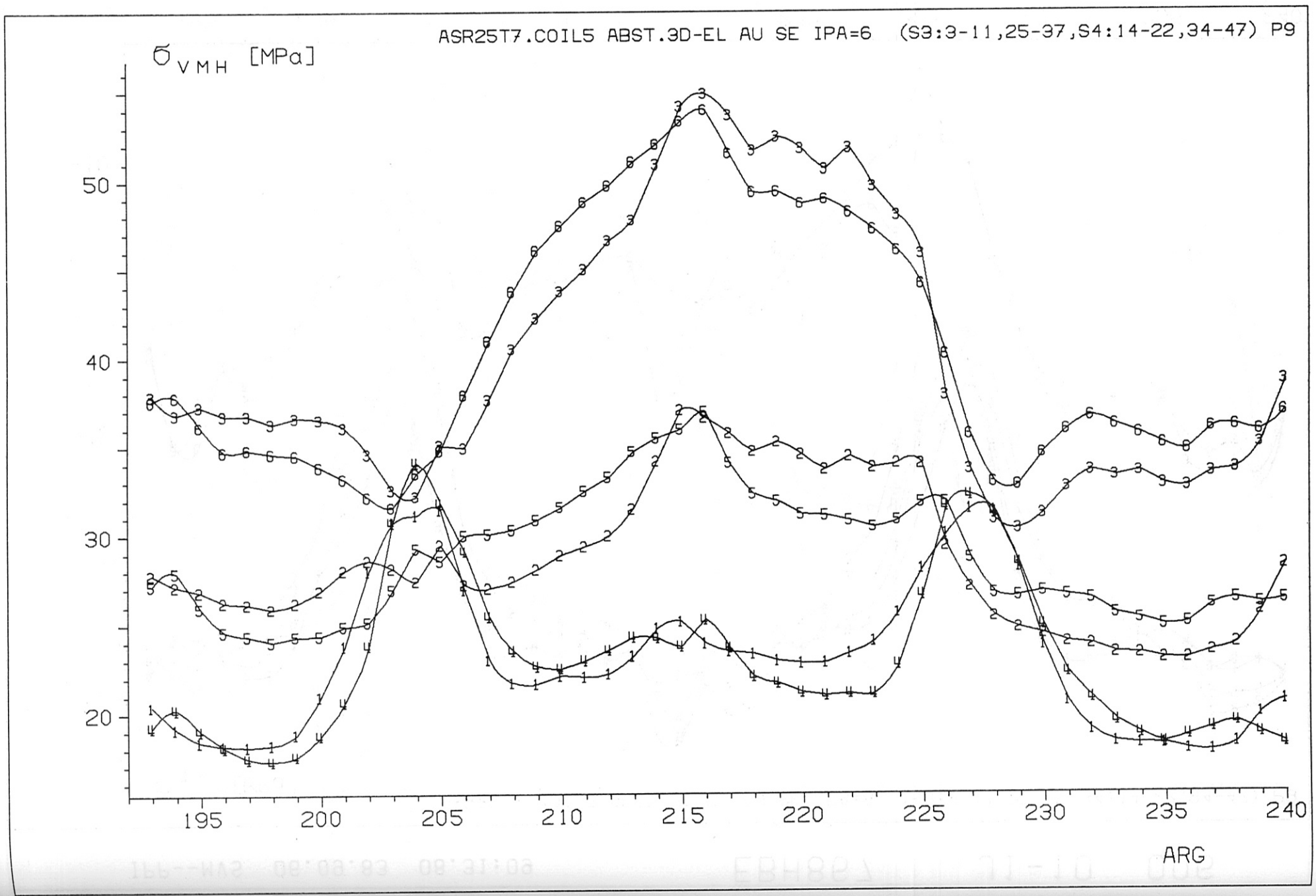

Fig. 56: Reference stress (von Mises stress) coil 5

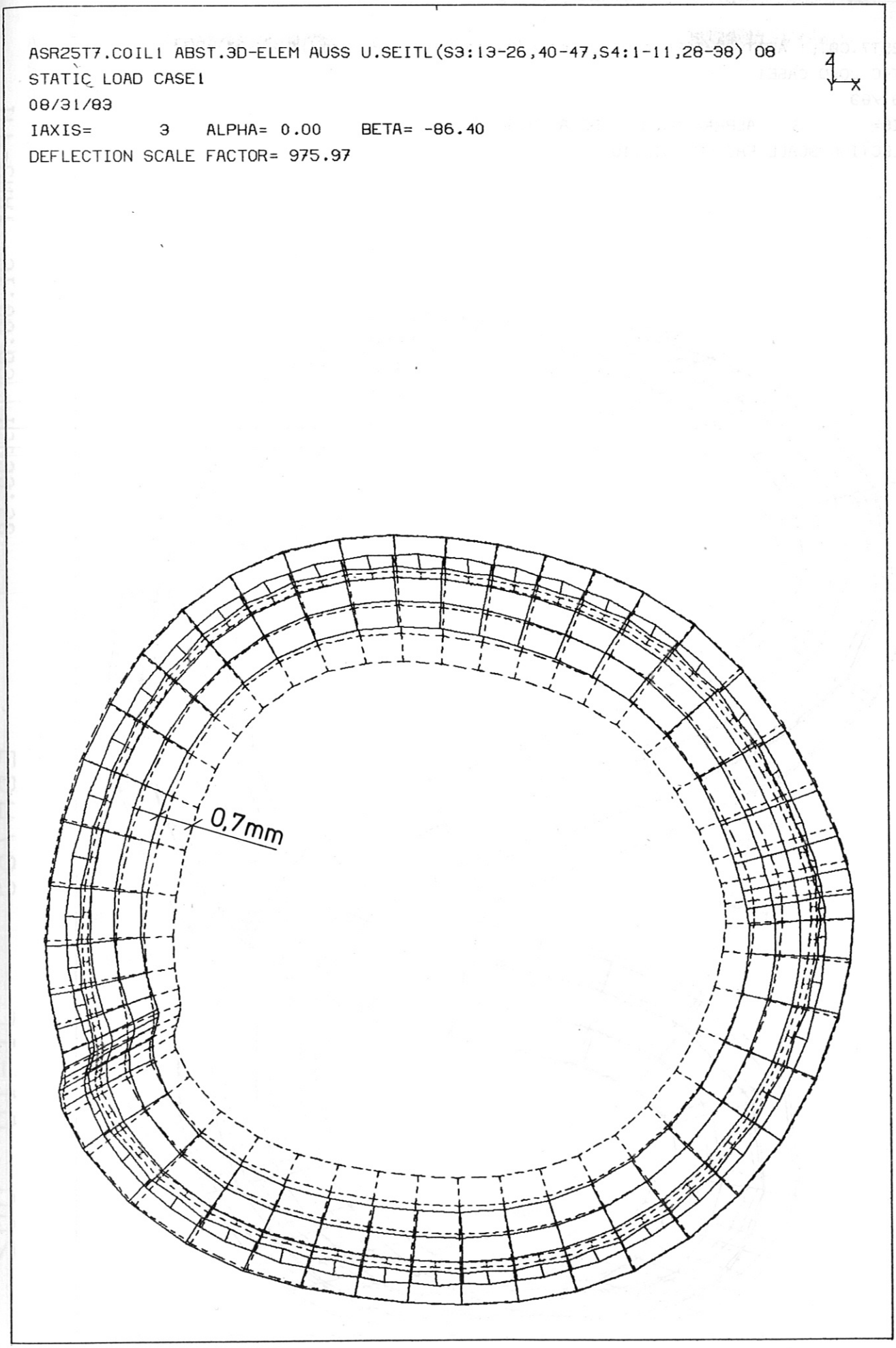

Fig. 57: Deflection coil 1 side view

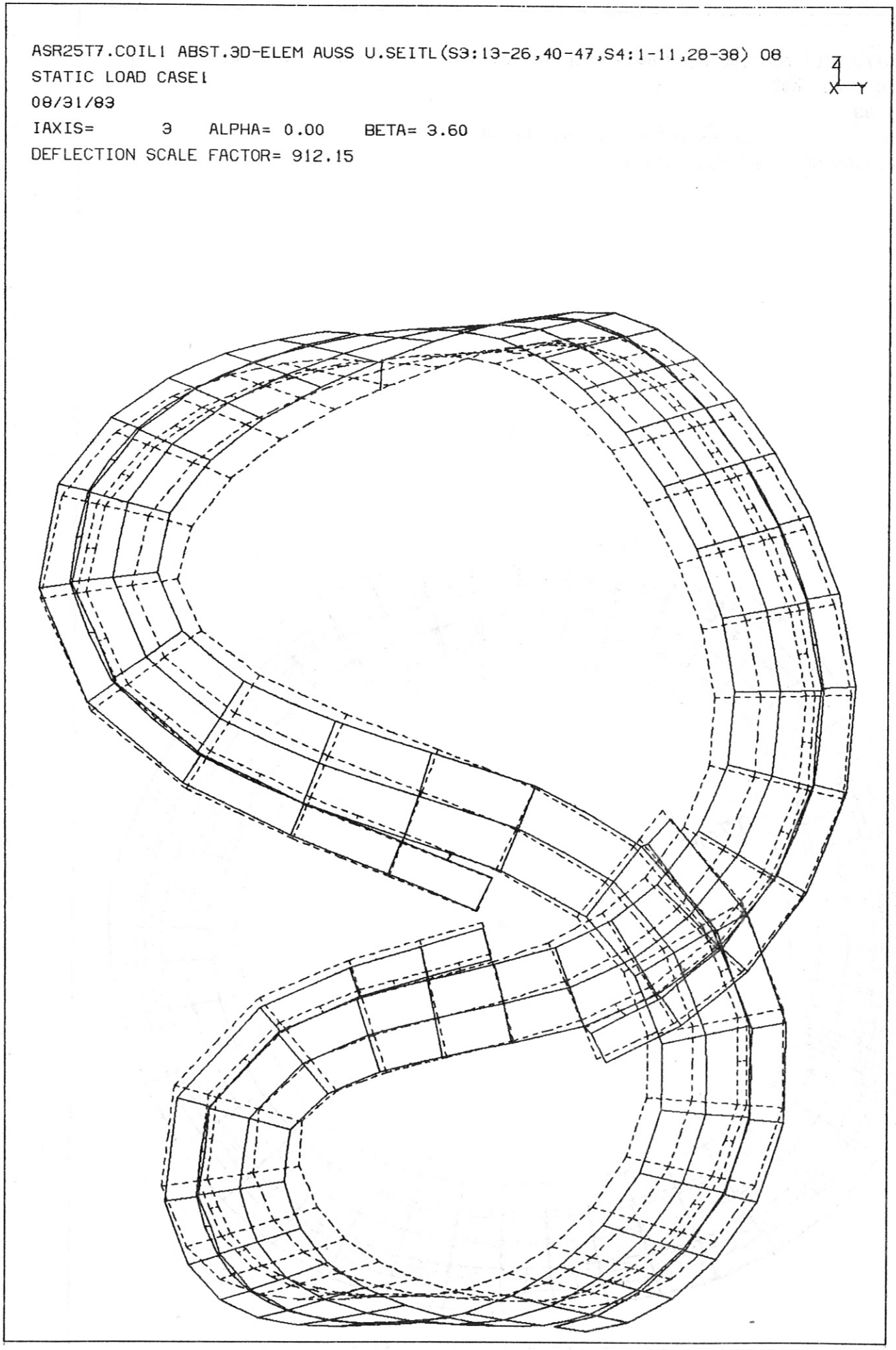

Fig. 58: Deflection coil 1 front view

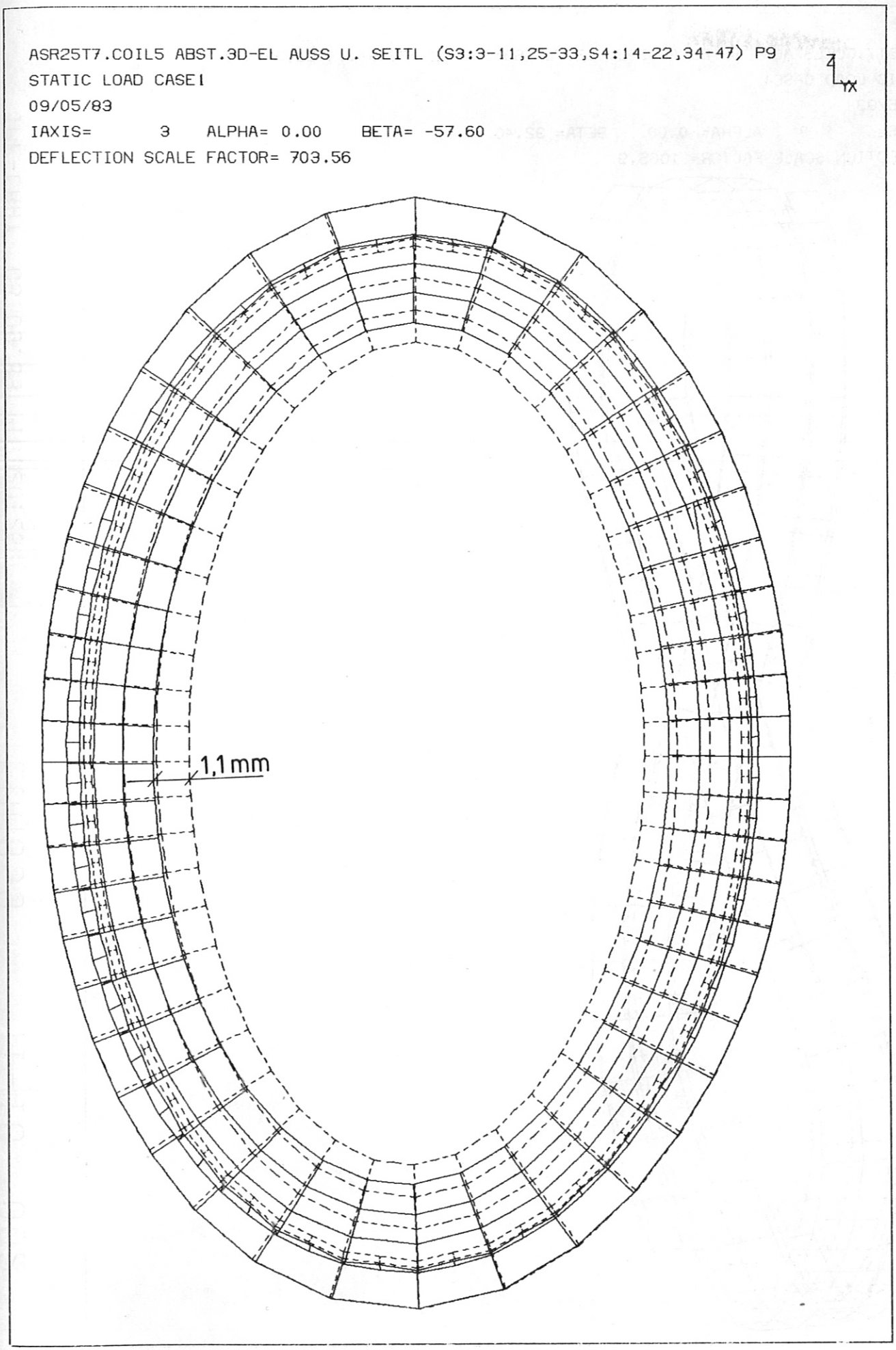

Fig. 59: Deflection coil 5 side view

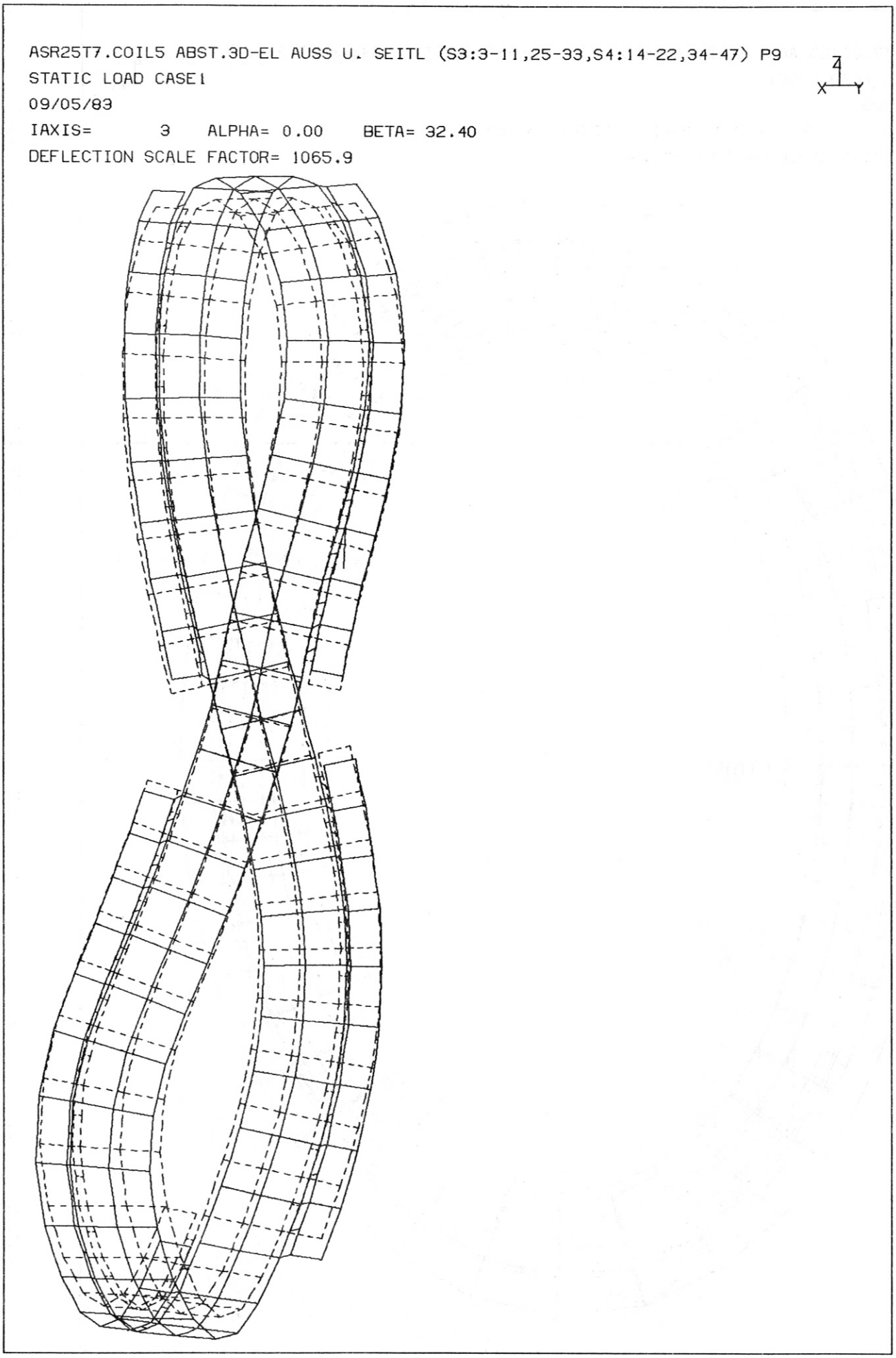

Fig. 60: Deflection coil 5 front view